Hydroacoustic and geochemical traces of marine gas seepage in the North Sea

Dissertation
zur Erlangung des Doktorgrades
der Mathematisch-Naturwissenschaftlichen Fakultät
der Christian-Albrechts-Universität
zu Kiel

vorgelegt von

Jens Schneider von Deimling

Kiel 2009

Referent .....Prof. Dr. Wolfgang Rabbel

Korreferent .....Prof. Dr. Gregor Rehder

Tag der mündlichen Prüfung 14.07.2009

Zum Druck genehmigt: Kiel, ...

Der Dekan

Hiermit erkläre ich, dass die vorliegende Doktorarbeit - abgesehen von der Beratung durch den Betreuer - nach Inhalt und Form die eigene Arbeit ist. Weder diese noch eine ähnliche Arbeit wurde an einer anderen Abteilung oder Hochschule im Rahmen eines Prüfungsverfahrens vorgelegt, veröffentlicht oder zur Veröffentlichung vorgelegt. Ferner versichere ich, dass die Arbeit unter Einhaltung der Regeln guter wissenschaftlicher Praxis der Deutschen Forschungsgemeinschaft entstanden ist.

Kiel, den

Jens Schneider von Deimling

Acknowledgement

First of all, I would like to thank Prof. Wolfgang Rabbel and Prof. Gregor Rehder for accepting me as a PhD student and for their great support. The following listings do not include all but the most important other contributors to this work.

The novel GasQuant device required a lot of technical understanding and adaption. Great support was offered by L3 Communications ELAC-Nautik and profound understanding about multibeam sonar was gained through intense discussions with Jörg Brockhoff and Boris Schulze, as well as through input from Wilhelm Weinrebe (IFM-GEOMAR). I also want to thank Peter Gimpel (ELAC) for his generous support as well as Sven Rohde and Frank Ritters for their programming and system adaptions.

During my PhD I participated in six research cruises with an overall of 6 months on various research vessels. During that time, I worked together with more than one hundred seamen and scientists who can not be listed individually. This intense time included endless nightshifts, great success immediately followed by severe failure enclosed in a fascinating and sometimes unreal environment and overall, it was great to share this experience in cooperation that sometimes turned into friendship.

Since I have learned about the challenging offshore work I have started to appreciate the experience of many seamen and scientists and especially benefitted of the wisdom about deep sea instrumentation by the great technicians Bernhard Bannert and Matthias Türk. In this context, I want to honor Peter Linke's work on the invention of Lander system. He was the head of the project COMET and supported me very much on different fields and enabled my two months stay at the University of Victoria. Also, I want to thank the head of the underwater acoustic group, Prof. Ross Chapman, who supervised me and from whom I gained a lot of knowledge for my work.

Further credit goes to Jens Greinert, Matthias Haeckel, Oliver Schmale, Nikolaus Bigalke, and Robin Keir for their scientific and technical support. I would have been lost without the help of the best office mate Christine Utecht; also I really appreciate the work of the technicians Karen Stange, Bettina Domeyer, Peggy Wevers and student help Nina Köplin. I enjoyed using the great IT structure at IFM-GEOMAR that facilitated my work a lot and I want to thank the two men behind these machines Rüdiger Kunze and Wilhelm Weinrebe.

Last but not least, special thanks go to my family for supporting me under any circumstances.

Preface

This PhD thesis consists of a general introduction Chapter I, followed by three stand-alone Chapters II-IV, a general conclusion Chapter V, and supplemental content in the Appendix.

Chapter II is the reprint of a published paper that outlines the feasibility of ship-born gas bubble detection with conventional multibeam mapping sonar and its advantages compared to single beam sounders. Chapter III consists of a submitted manuscript describing the use of a prototype in situ multibeam bubble monitoring system (GasQuant) and illustrates the device's potential to resolve tempo-spatial variation of gas seepage. Due to technical difficulties, the aspired calibration of GasQuant failed and a quantitative analysis of the echo signals could not be accomplished. Even though, gas bubble acoustic inversion theory and principle limitations are discussed in Appendix B. Furthermore we attach a registered patented generic algorithm in Appendix A to e.g. automatically detect rising gas bubbles in sonar data.

Chapter IV covers the seepage at a specific seep site in the North Sea combining acoustic and geochemical methods. Thus, the source strength of the respective seep field could be determined and the further fate of methane seepage in the North Sea is discussed. This Chapter is again in the form of a manuscript for a peer reviewed journal and will be submitted shortly. Two peer-reviewed Co-authorship publications abstracts related to this work can additionally be found in the Appendix C and Appendix D.

The titles, authors and the state of each paper and manuscript are briefly listed below

Chapter II

Flare imaging with multibeam systems: Data processing for bubble detection at seeps

Authors J. Schneider von Deimling, J. Brockhoff, J. Greinert

Status published in *G-cubed* (2007), doi:10.1029/2007GC001577

Chapter III

Acoustic imaging of natural gas seepage in the North Sea: Sensing bubbles under control of variable currents

Authors J. Schneider von Deimling, J. Greinert, N.R. Chapman, W. Rabbel, P. Linke

Status under review at *Limnology & Oceanography Methods*

Chapter IV

A multidisciplinary approach to quantify methane gas seepage at Tommeliten

Authors J. Schneider von Deimling, G. Rehder, D.F. McGinnis, J. Greinert, P. Linke

Status ready for submission to *Continental Shelf Research*

Appendix A*

Patentanmeldung 10 2009 033 724.5
Teilchendetektions- und Identifikationsverfahren in bekanntem Strömungsmilieu

Status submitted to *Deutsches Patent- und Markenamt*

Appendix B

Seep bubble acoustics – the inversion of bubble backscatter into gas flux and principle limitations

Status in preparation for future publication

Appendix C**

Shallow Microbial Recycling of Deep-Sourced Carbon in Gulf of Cadiz Mud Volcanoes

Authors M. Nuzzo, Edward R. C. Hornibrook, C. Hensen, R. Parkes, C. John, A. Barry, J. Rinna, J. Schneider von Deimling, S. Sommer, V. Magalhaes, A. Reitz, W. Brückmann

Status published in *Geomicrobiology Journal* (2008), doi: 10.1080/01490450802258196

Appendix D**

Sea be d me thane e mission from the Ca ptain Arutyunov mud volcano (Gul f of Cadiz) – a tubeworm dominated seep ecosystem

Authors S. Sommer, O. Pfannkuche, P. Linke, T. Schleicher, J. Schneider von Deimling, M. Haeckel, S. Flögel, A. Reitz, C. Hensen

Status published in *Marine Ecology Progress Series* (2009), doi: 10.3354/meps07956

*patent was submitted to “Deutsches Patentamt München” by the PVA Schleswig Holstein

**The contribution to the publications include high precision multibeam surveying, postprocessing and visualization of the soundings; CTD casting and water sampling, methane concentration measurements and interpretation of the data, and general review of the contents of the papers.

Zusammenfassung

Methan ist das zweitstärkste anthropogene Treibhausgas auf der Erde und trägt damit wesentlich zur globalen Strahlungsbilanz bei. Der letzte Sachstandsbericht des Weltklimarats (IPCC Report, 2007) ordnet geologischen Emissionen eine nicht zu vernachlässigende Quellstärke zu. Diese Arbeit konzentriert sich auf geologische Methanquellen am Meeresboden in der Nordsee.

Auf Grund der erschwerten Zugänglichkeit im Vergleich zu terrestrischen Quellen sind marine Methanquellen am Meeresboden schlecht untersucht und wurden bisher quantitativ kaum oder gar nicht erfasst. Des Weiteren werden die Prozesse, die den quantitativen Transport des Methans vom Meeresboden an die Grenzschicht Ozean/Atmosphäre steuern, nur unzureichend in die Betrachtungen mit einbezogen.

Zur Untersuchung von natürlichen Gasaustrittsgebieten (*Seepages*) haben sich Sonarsysteme bewährt, mit deren Hilfe methanhaltige Gasblasen selbst in Wassertiefen von über 2000 m nachgewiesen werden können. Die technische Entwicklung der letzten Jahre hat das Fernerkundungspotential sogenannter Fächerecholotsysteme in Hinblick auf Gasblasendetektion in der Wassersäule stark verbessert. Jedoch erfordern Daten aus der Wassersäule, die mit solchen Sonarsystemen aufgezeichnet werden, spezielle Methoden für deren wissenschaftliche Auswertung. Diese Arbeit zeigt exemplarisch einige Möglichkeiten auf, solche Systeme effizient zur Gasblasendetektion zu verwenden. Hierzu wurde eine anthropogene Gasaustrittsstelle in der Nordsee mittels eines solchen Fächerecholots akustisch untersucht. Der Vorteil der hierbei verwendeten Technologie besteht in der größeren räumlichen Überdeckung (im Vergleich zu Einstrahlsonaren), in der dreidimensionalen Kartierung der Gasaustritte sowie in der exakten Lokalisierung der Gasaustrittsstellen.

Ferner wird der Einsatz des „GasQuant“ Prototyps behandelt - eines Systems zur in situ Untersuchung von Gasaustritten auf Grundlage eines Fächerecholots. Dieses System wurde für mehrere Tage in dem Tommeliten-Gasfeld (zentrale Nordsee) mit aktiven Gasaustritten eingesetzt. Neben kleineren Systemanpassungen wurden zahlreiche Routinen zur Verbesserung der Datenqualität und deren Visualisierung entwickelt. Unter Berücksichtigung des tidalen Strömungsfeldes konnten spezielle Datenmuster herausgearbeitet werden, die eindeutig Gasaustritte in die Wassersäule belegen. So konnten 52 Gasaustrittsstellen lokalisiert und deren räumlich-zeitliche Aktivität bestimmt werden.

Erst seit Kurzem sind wassersäulenscannende Fächerecholotsysteme kommerziell erhältlich. Jedoch sind die gewonnenen Datenmengen so umfangreich, dass eine manuelle Auswertung kaum zu bewerkstelligen ist. In Appendix A wird daher ein automatisiertes

Verfahren vorgeschlagen, um aufsteigende Gasblasen in Fächerecholotsystemen algorithmisch aufzuspüren.

Unter Einbezug weiterer Teildisziplinen (Geochemie, Ozeanographie) konnte eine quantitative Methangas-Flussabschätzung eines Gasaustrittsgebietes in der Nordsee durchgeführt werden. Unter diesem Aspekt wurde das Tommeliten-Gasfeld untersucht. Eine akustische Vermessung und in situ Beprobung ergab eine Quellstärke von ~0.8-4.8*10^6 mol/Jahr - im Vergleich zu weit bekannteren Gasaustrittsstellen (Vodyanitskii Schlammvulkan, Schwarzes Meer: ~1*10^6 mol/Jahr; Nordteil Hydrate Ridge, offshore Oregon: 2.19*10^6 mol/Jahr) ist dies eine beträchtliche Größe. Des Weiteren belegen geochemische Daten und Modellrechnungen, dass sich der Großteil des durch Gasblasen induzierten Methans bereits in der Sommer-Tiefenwasserschicht löst. Das Tiefenwasser und damit der darin gelöste Methanpool ist durch die Thermokline vom Oberflächenwasser und somit auch vom Austausch mit der Atmosphäre entkoppelt. Bisherige Forschungsfahrten, die u. a. den durch Gasaustritte bedingten atmosphärischen Methaneintrag untersuchten, konzentrierten sich auf die windärmere Sommersaison. Vermutlich wurden beträchtliche Mengen Methan, die sich während der Sommermonate im Tiefenwasser akkumulieren, hierbei nicht erfasst. Es ist jedoch zu erwarten, dass in der Winterjahreszeit dieses Methan aus einigen Gebieten der Nordsee quantitativ in die Atmosphäre überführt wird. Diese saisonale Ungleichheit beschränkt sich jedoch nicht auf das Arbeitsgebiet, sondern gilt für die gesamte zentrale und nördliche Nordsee sowie für Gasaustritte in Flachmeeren gemäßigter Breiten mit temporärer Ausbildung stabil stratifizierter Verhältnisse.

Abstract

Methane is the second most important anthropogenic greenhouse gas on Earth and contributes considerably to global radiative forcing. The last IPCC assessment report 2007 assigns geological methane emissions as a significant source. This thesis therefore concentrates on the quantity and atmospheric implications of methane emissions from the seabed of the North Sea.

Sampling of marine seepage is challenging compared to readily accessible terrestrial sites; thus marine seepage sites have scarcely been observed or even yet discovered. Moreover, in terms of atmospheric contribution, the fate of methane after ebullition into the water column is usually not considered.

Hydroacoustic systems have proven to be very efficient remote sensing tools for gas seepage analysis even in water depth greater than 2000 m. Technical progress led to much higher remote sensing potential by means of modern multibeam applications for gas bubbles detection in the water column. However, to be effective, these novel multibeam systems require new methods for data analysis.

This thesis firstly demonstrates the application of multibeam systems as efficient gas bubble remote sensing tools. Therefore an anthropogenic blowout site was mapped using a multibeam sonar. The advantage of multibeam technology compared to singlebeam is increased efficiency due to larger coverage than singlebeam systems, three dimensional plume mapping, and exact localization of gas sources.

Moreover the deployment of the multibeam prototype *GasQuant* is examined, which is an adapted sounder specifically designed for in situ gas bubble detection. GasQuant was deployed for several days within a gas seep field in the Central North Sea (Tommeliten). Aside from minor system adaptations, major effort was spent to handle the non-standard large datasets by means of various data processing and visualization routines. Taking into account the surrounding tidal current flow field, unique data patterns were extracted to un-ambiguously detect gas bubbles in the water column. Thus, a total of 52 single seep holes were localized and characterized with respect to their tempo-spatial variability.

Recently, water column scanning multibeam mapping systems entered the market. Due to their huge amount of data output, manual processing is no longer feasible. Thus, a generic algorithm for the detection of rising gas bubbles in multibeam data was developed that accounts for the current tidal flow field for detection issues (Appendix A).

Incorporation of other disciplines such as geochemistry and oceanography allowed for a methane gas source strength estimate of the Tommeliten gas seepage field in the North Sea.

Combined acoustic mapping and in situ sampling revealed a source strength of ~0.8-4.8*10^6 mol/yr – a considerable quantity compared to prominent gas seep sites around the world (e.g. ~1*10^6 mol/yr at Vodyanitskii mud volcano, Black Sea; 2.19*10^6 mol/yr at North Hydrate Ridge offshore Oregon). Obviously previous studies have underestimated the area of active venting at Tommeliten. By modeling gas bubble dissolution and geochemical sampling it was found that the majority of bubble-mediated methane at Tommeliten already dissolves in the 'deep' water between the 70 m release depth and 40 m. Thus the methane is trapped below the upper-well mixed summer layer, from which it would readily be degassed by air-sea exchange processes. Given the heavy storm activity during winter, research cruises into the North Sea preferentially take place during the summer, where low atmospheric outgassing/emissions from seabed methane is expected due to stratification. However, considering the distinct hydrographic seasonal cycle of the North Sea, quantitative transport of seepage methane into the atmosphere seems likely during winter after fall mixing. This seasonal bias is not only constrained to the study site, but relevant for the entire Central and Northern North Sea as well as many mid-latitude shallow shelf sea waters showing temporal stratification.

TABLE OF CONTENTS

General Introduction

Methane in the Global Carbon Cycle

The greenhouse gas methane

Methane is the most abundant hydrocarbon in the atmosphere and has more than doubled since the pre-industrial era to a global mean average of 1.774 ppm in 2005 (IPCC, 2007). Although this concentration is much smaller than the currently observed 379 ppm global mean of CO_2, a 25-fold increased global warming potential of CH_4 (on a 100 yr timescale) on a mole-to-mol basis to CO_2 drives methane the second most important anthropogenic greenhouse gas on Earth with a 18 % contribution to the total radiative forcing of all long-lived greenhouse gases.

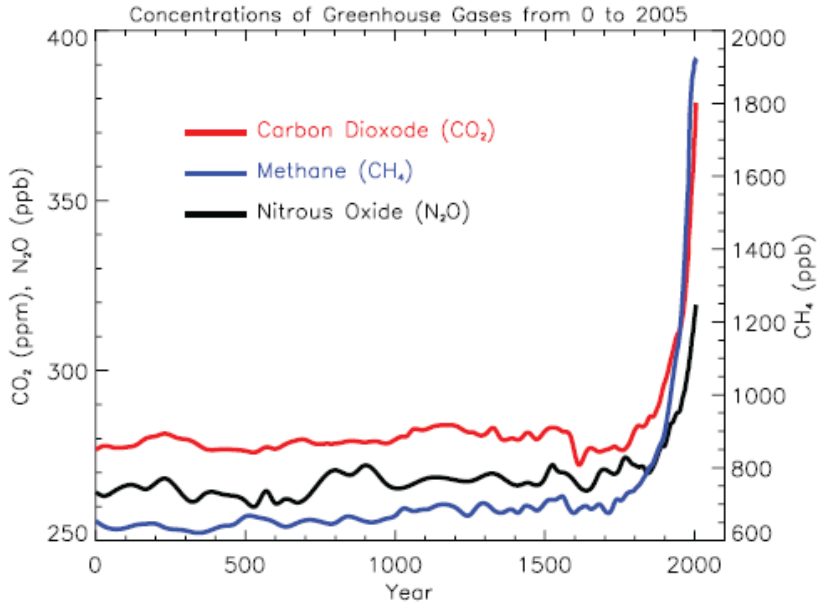

Figure 1: taken from (IPCC, 2007) showing a 2.5-fold methane concentration increase since the onset of industrialization.

The distinct post-industrial increase of atmospheric methane concentration has slowed from 1 % growth rate in the early 80'ies (BLAKE and ROWLAND, 1988) to close to zero towards the turn of the millennium, the reasons for this being under debate (Prather, 2001) but are clearly related to the imbalance between CH_4 sinks and sources. However, starting near the beginning of 2007 a renewed growth was recently reported by RIGBY et al. (2008).

The net atmospheric methane contribution is currently estimated 592 Tg(CH_4)/yr (IPCC, 2007) and predominantly caused from anthropogenic contributions (>60%, Figure 2). Major sinks for atmospheric CH_4 comprise reaction with the photochemically produced hydroxyl free radical (OH) and stratospheric removal followed by weaker sinks such as methane consumption in soils (BORN et al., 1988) and reaction with free chlorine (PLATT et al., 2004).

In terms of genesis and source, methane might be classified into three different types. Occasionally, methane is produced in magmatic systems on primarily mid-ocean ridges and terrestric volcanoes and named *abiotic* methane. So-called *thermogenic* methane may originate from larger depths associated with hydrocarbon reservoirs, where CH_4 was formed during maturation processes of higher hydrocarbons within geological time-scales. By far the strongest contribution derives from recent degradation of organic matter by microbial activity under anoxic environments on land, in the seabed, and even in the open ocean and is termed *biogenic*.

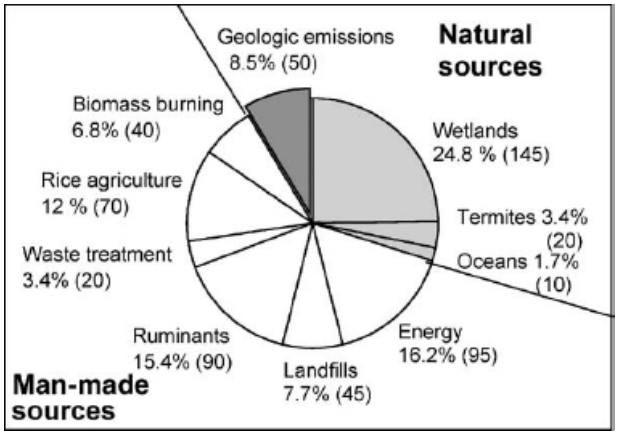

Figure 2: Taken from ETIOPE (2004) showing sources of atmospheric methane including geologic emissions (mean fluxes in Tg/yr in brackets). Non-geologic sources are taken from the Third Assessment Report of IPCC.

The main sources of CH_4 were assessed in the IPCC (2007) Tab. 7.6. Anthropogenic contribution of methane into the atmosphere primary derives from rice agriculture, livestock, landfills, waste treatment, biomass burning and fossil fuel combustion. Major natural sources include wetlands, oceans, fire, termites. Even though the overall CH_4 budget is relatively well known by the application of different budgeting methods (e.g. bottom-up, top-down analysis), the individual contributors are not. Just recently, KEPPLER et al. (2006) reported a so far unknown atmospheric methane source derived from tropical leafs as a potential extra major methane source by a hitherto unknown genesis. In the oceans a new process of methane formation in the upper water column was recently proposed by KARL et al. (2008).

Geologic emissions of methane through mud volcanoes, faults and seepage have been neglected in the previous IPCC reports and are not listed in IPCC (2007) Tab. 7.6, but are suggested as a potentially important source between 40-60 $Tg(CH_4)/yr$ (ETIOPE, 2004, KVENVOLDEN and ROGERS, 2005).

To clarify methane sources is a first step to better understand biogeochemical cycling and climate change and is thus a matter of global concern.

Marine methane seepage

One poorly understood source of geologic methane emissions derives from seabed seepages, where methane rich fluid and/or gas migrate from the depth towards the seafloor. This phenomenon has been observed world-wide, especially on continental margins (JUDD and HOVLAND, 2007) and was attributed an atmospheric source strength of 20 Tg/yr (JUDD, 2004). However, such an estimate is challenging, because submarine sources are difficult to find and the water column may potentially act as a natural filter that quantitatively suppresses methane emission from the seafloor into the atmosphere. Figure 3 illustrates the potential origin and migration pathway of methane gas seepage from the seafloor to the atmosphere. Methane migration from the depth originates from abiotic, thermogenic, or biogenic sources, where the latter two are often associated with and affected by the presence of gas hydrates, that currently hold substantial amounts of methane (BUFFETT and ARCHER, 2004). The upward migration of methane either takes place dissolved in interstitial pore water or in the form of gas bubbles creeping through the seabed sediments (SUESS et al., 1999; SUESS et al., 2001; BOUDREAU et al., 2005).

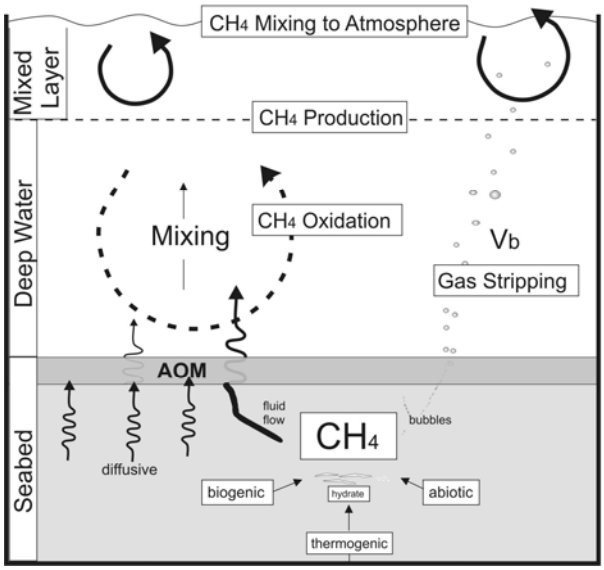

Figure 3: Schematic sketch illustrating the sources and further processes controlling the fate of methane derived from seepage during upward migration through the sediment, across the seafloor-seawater boundary, through the water column, and up towards the sea surface and atmosphere.

Only a fraction of dissolved methane transported by advective fluid flow reaches the water column, because anaerobic microbial oxidation (*AOM*) effectively converts approximately 80 % of dissolved methane to CO_2, representing the most effective sink for seepage methane (HINRICHS and BOETIUS, 2002). In contrast, rising methane bubbles by-pass this microbial filter and directly transport methane into the water column, where the gas bubbles

are prone to dissolution during their upward movement through the water column. Oxidation of the diluted methane is highly reduced compared to the AOM. Depending on the gas ebullition type and environmental settings (water depth, temperature, oxidation potential) the seepage gas may directly reach the sea surface or enter the upper well-mixed layer, where air-sea exchange finally transports sedimentary CH_4 to the atmosphere within a timescale shorter than the turnover time for oxidation.

In the future, several processes are expected to cause a significant increase of the marine methane flux, partly due to anthropogenic forcing. Enhanced eutrophication is expected to augment shallow gas production from fresh organic material (BEST et al., 2006). Also, enhanced methane fluxes from dissociating hydrates are expected as a response to seafloor warming (BUFFETT and ARCHER, 2004), in particular in polar regions, where in addition organic material formerly conserved in permafrost shelf areas is warmed and thus starts to be consumed by methanogens (SHAKHOVA et al., 2005).

Sonar and gas seepage detection

History and invention of sonar

Remote sensing of the Earth has become popular by the use of satellites especially using electromagnetics in order to obtain information about the atmosphere and the surface of the Earth and other planets. But remote sensing of the hydrosphere is critical due to the restricted penetration of the widely used electomagnetic methods. Thus hydroacoustics gained major importance in marine science because compressional waves are transmitted in water much farther than electromagnetic shear waves and - depending on frequency - even reach the deepest parts of the ocean. Large ranges can be achieved even in muddy water and allow enhanced target detection were optical systems fail. Therefore echosounders have established as standard tools in remote sensing of the ocean.

Although the modern age of underwater sound is often dated back just to the second World War, its straightforward application was stated already in1490 by Leonardo da Vinci: “if you cause your ship to stop, and place the head of a long tube in the water and place to outer extremity to your ear, you will hear ships of a great distance from you”. This is an example of a passive and non-electric acoustic method marking the begin of a long and successful development of sound navigation and ranging (sonar) in marine science.

Towards the nineteenth century, the invention of transduction of electricity into vibration/sound and vice-versa enabled the design of electronic sonar systems with the most famous device patented by Bells company in 1876 - the telephone (later the common unit deciBel was named there after).

Inspired by the sinking of the cruise ship ‘Titanic’, the German physicist Alexander Behm was looking for obstacle avoidance techniques and found a great method to measure the depth of the seafloor and invented ship-born echo sounding in the sea (Reichspatent Nr. 282009).

From single- to multibeam

So called ‘singlebeam’ echosounders were invented in the 1920s and initially used for ship-born seafloor depth determinations. They have turned out to be very effective tools in order to find, identify and quantify single fish, fish schools, zooplankton layers, ship’s wakes or seep bubbles. The rise of gas bubbles from the lake/seafloor have firstly been reported from sonar data by OHLE (1960) and MCCARTNEY and BARY (1965). Early technological restrictions only allowed for data storage on thermal paper in the form of grey-scaled coded records. The advent of mass storage around the early 80’ies enabled singlebeam sonar systems to produce digital echograms and storage. This opened enhanced access, postprocessing and analysis of sonar data to the scientific community and a couple of publications manifesting worldwide occurrences of seep bubbles to occur (MEREWETHER et al., 1985; JUDD et al., 1997; HORNAFIUS et al., 1999; ARTEMOV et al., 2007). Significant progress in digital signal processing brought about the design of so called multibeam systems (DE MOUSTIER, 1988), that entered the market in 1977 for coastal navigation assurance, bioacoustic investigations, and scientific seafloor mapping (SEABEAM on R/V Jean Charcot; RENARD and ALLENOU, 1979). By 2001 around 700 MB sounders had been put into service and today, multibeam sonar even gained importance through the request of the definition of continental shelve territory boundaries. Modern multibeam sounders cover an acoustic fan of up to 150° and make surveying much more efficient, and narrow beamforming even improves resolution for the cost of higher data volume to be stored. So called bottom detection algorithms were inevitably to distinguish valuable seafloor echoes from spurious water column reflections. Today, the number of beams of those modern multibeam systems exceeds 300. By the advent of high-level digital signal processing boards and mass storage, digital sampling of echo soundings from all depths and (beam) directions is technically feasible and give rise to water column imaging (*WCI*).

In this study we concentrate on the use of both conventional (Chapter II) and prototype WCI multibeam (Chapter III) for gas seepage research and stress the advance of the latter WCI

system. Novel methods are presented for dataprocessing, visualization and automated bubble detection (Appendix A), which will be valuable for future WCI systems. Moreover principle limitations in the inversion of sound into seep gas flux are outlined in Appendix B.

North Sea

Bathymetry and hydrography

The North Sea is a semi-enclosed, shallow sea located on the western European continental shelf with an average water depth of 74 m, deepening from south to north. The only exception is the Norwegian trench along the east coast of Norway, which represents the most striking bathymetric feature with a maximum water depth of 730 m. Elsewhere, the bathymetry is fairly flat, with a significant morphological high in the south (the morainic, shallow Dogger Bank, visible through the 30 m contour line, Figure 4) and several round-shaped small depressions in the north.

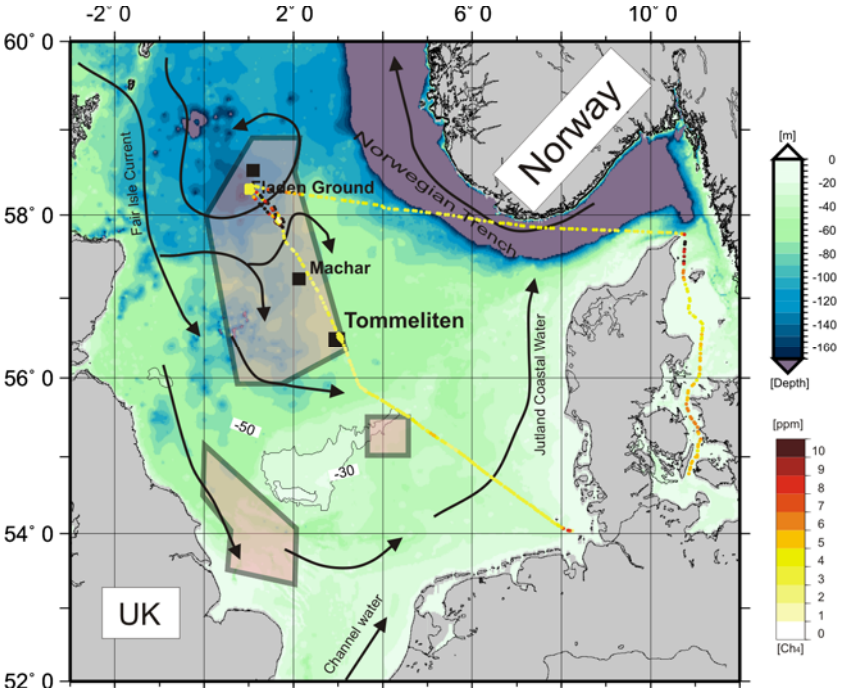

Figure 4: (a) North Sea bathymetry from GEBCO_08 30 arc seconds grid (http://www.gebco.net) with schematic hydrographic information of the main flow pattern adapted from TURRELL et al. (1992). Gas seepage areas (purple polygons) surrounding the study area Tommeliten were compiled from various sources (Norwegian EEZ: JUDD and HOVLAND (2007); English EEZ: JUDD et al. (1997), JUDD (2001); Dutch EEZ: SCHROOT et al., (2005). Color coded dots represent surficial methane concentration gathered during ALK 259.

The residual flow pattern within the semi-enclosed North Sea reveals anti-clockwise rotation with the main inflow of Atlantic water entering the Northern North Sea (*Fair-Isle-Current*, *Shetland Flow*) flowing along the Scottish/British East coast towards the south. A minor contribution of Atlantic water enters through the Strait of Dover. Aside freshwater admixture through various rivers along the Dutch and German coasts, considerable brackish water from the Baltic is mixed with North Sea water in the Skagerrak. Eventually, a newly formed water type leaves the North Sea as Norwegian coastal current. The turnover time for the North Sea as a whole is estimated about a year (OTTO et al., 1990). However, the anti-clockwise rotation and one-year overturn period are bulk patterns. The dispersion of a tracer such as methane may locally and temporarily considerably differ from this advection scheme due to the present flow controlling factors (tides, meteorological impacts, residual Atlantic advection, and density currents).

The North Sea is strongly affected by seasonal temperature change, which is the predominating periodic, long-term signal. This temperature oscillation seasonally warms and cools the upper layer leading to in- and decreasing stratification.

The extent of stratification is correlated to the ratio between water depth and cubed tidal velocity (SIMPSON and HUNTER, 1974). Thus, in a general view, the deeper and less tidally influenced offshore areas of the Northern and Central North Sea show pronounced summer stratification (DIETRICH, 1950) whereas coastal areas, the shallow Dogger Bank and the very southern part of the North Sea appear mixed throughout the year (Figure 5, dark areas).

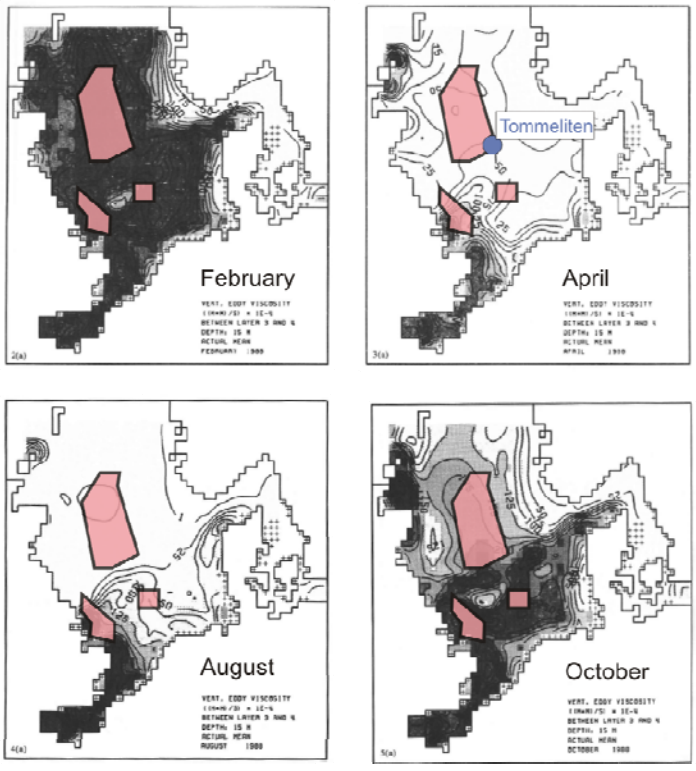

Figure 5: Demonstration of seasonal change of stratification expressed as monthly averaged vertical eddy viscosity A_v between 15 and 20 meters grid cell/water depth (POHLMANN, 1996); the darker the color-coding the larger is A_v and vertical mixing. Seepage areas are coded by purple polygons like in Figure 4.

Geological setting and methane sources

In terms of petroleum geology the North Sea is a complex buried graben structure holding Permian to Tertiary source rock from which oil, gas and fluids migrate from depth and potentially find storage in shallow hydrocarbon and methane-rich reservoirs. Further vertical migration of hydrocarbons up to the seafloor is often associated with salt doming (SCHUMACHER and ABRAMS, 1994). Other major sources of methane are supplied from biological production in the sediment. JUDD and HOVLAND (2007) compiled data of shallow gas and pockmark fields that are likely to release methane to the water column. Besides locations along the Norwegian trench in the East (e.g. Gullfaks), a large pockmark and seepage field spreads along the graben from the Fladen Ground area (58° 30'N, 1° E) to Machar (57° N, 2° E) and Tommeliten (56° 30'N, 3° E, Figure 4). Within the English EEZ frequent gas release was reported (JUDD et al., 1997) extending from the British Coast to approximately 1° E. Recently, SCHROOT et al. (2005) reported shallow gas findings and acoustic evidence for free gas in the water column next to the Dogger Bank.

Water column investigations in the North Sea were conducted by REHDER et al. (1998) showing two sections of continuous measurements of surface water and air CH_4 concentration during May 1994. The West-East transit extends from 58° N 1° W to 58° N 10° E and initially shows low background methane concentration of 2.5-3.5 nM, representing typical values of Atlantic inflow water. Methane concentrations repeatedly exceeded atmospheric equilibrium and the maximum was found in the vicinity of an abandoned borehole. Methane-enriched surface waters were also detected in the Skagerrak and in the surface water plume entering from the Baltic during the time of the measurement. A NW-SE section similar to the one in Figure 4 also starts from 58° N 1° W and shows methane concentration slightly above atmospheric equilibrium until the Dogger Bank is reached, where a 15 nM peak was detected. Finally, approaching the mouth of the river Elbe, methane concentrations increase steadily with decreasing salinity. A similar general trend was observed in the run-off areas of several Dutch rivers like the Scheldt and the Rhine (DE WILDE and DUYZER, 1995), though the Elbe shows the most conservative mixing behavior, as a result of the high water flow and a narrow estuary area. Results from Alkor cruise *ALK 259* in June 2005 basically redraw the findings presented in REHDER et al. (1998) except for reduced concentration in the northerly W-E transect.

Tommeliten

The major study site of this thesis is the Tommeliten gas seep field located in the Central North Sea (Norwegian Block 1/9, Figure 4) and was first discovered during one of the frequent seismic surveys along the North Sea graben in 1978. The seep field is underlain by a salt diapir that has most likely domed and pierced the upper sediments, giving pathway for fluid and gas migration along fractures from greater depth (HOVLAND and SOMMERVILLE, 1985; HOVLAND and JUDD, 1988). Shallow gas and persistent free gas ebullition was manifested in side-scan and pinger records (HOVLAND and SOMMERVILLE, 1985) and confirmed by early (HOVLAND and SOMMERVILLE, 1985) and recent (NIEMANN et al., 2005) video analysis using ROVs. A crude estimate about the gas seeping area was given and a total of 120 seep vents was estimated (HOVLAND and JUDD, 1988). A more comprehensive description of the state of the art knowledge about Tommeliten is given in Chapter III and IV.

References

Artemov, Y. G., Egorov, V. N., Polikarpov, G. G., and Gulin, S. B., 2007. Methane emission to the hydro- and atmosphere by gas bubble streams in the Dnieper paleo-delta, the Black Sea. *Reports of the Natl. Acad. of Sci. of Ukraine* 5, 110-116.

Best, A. I., Richardson, M. D., Boudreau, B. P., Judd, A., Leifer, I., Lyons, A. P., Martens, C. S., Orange, D. L., and Wheeler, S. J., 2006. Shallow Seabed Methane Gas Could Pose Coastal Hazard. *Eos* 87, 213-220.

Blake, D. and Rowland, F., 1988. Continuing worldwide increase in tropospheric methane, 1978 to 1987. *Science* 239, 1129–1131.

Born, M., Dörr, H., Levin, I., and Münnich, K. O., 1988. Methane concentration in aerated soils in West-Germany. *Chemical Geology* 70, 101-101.

Boudreau, B. P., Algar, C., Johnson, B. D., Croudace, I., Reed, A., Furukawa, Y., Dorgan, K. M., Jumars, P. A., Grader, A. S., and Gardiner, B. S., 2005. Bubble growth and rise in soft sediments. *Geology* 33, 517-520.

Buffett, B. and Archer, D., 2004. Global inventory of methane clathrate: sensitivity to changes in the deep ocean. *Earth and Planetary Science Letters* 227, 185-199.

De Moustier, C., 1988. State of the art swath bathymetry survey systems. *Int. Hydrogr. Rev* 65, 29-38.

de Wilde, H. P. J. and Duyzer, J., 1995. Methane emissions off the Dutch coast: Air-Sea concentration differences versus atmospheric gradients. In: Jähne, B. and Monahan, E. C. Eds., *Air-Water gas transfer*. AEON-Verlag, Hanau.

Dietrich, G., 1950. Die natürlichen Regionen der Nord- und Ostsee auf hydrographischer Grundlage. *Kieler Meeresforsch.* 7, 35-69.

Etiope, G., 2004. New Directions: GEM--Geologic Emissions of Methane, the missing source in the atmospheric methane budget. *Atmospheric Environment* 38, 3099-3100.

Hinrichs, K.-U. and Boetius, A., 2002. The anaerobic oxidation of methane: New insights in microbial ecology and biogeochemistry In: Wever, G., Billett, D., Hebbeln, D., Jørgensen, B. B., Schlüter, M., and van Weering, T. C. E. Eds., *Ocean Margin Systems*. Springer-Verlag, Heidelberg.

Hornafius, J. S., Derek, Q., and Luyendyk, B. P., 1999. The world´s most spectacular marine hydrocarbon seeps (Coal Oil Point, Santa Barbara Channel, California): Quantification of emissions. *Journal of Geophysical Research* 104, 20703-20712.

Hovland, M. and Judd, A. G., 1988. Seabed pockmarks and seepages. Graham and Trotman, London.

Hovland, M. and Sommerville, J. M., 1985. Characteristics of two natural gas seepages in the North Sea. *Marine and Petroleum Geology* 2, 319-326.

IPCC, 2007. Climate Change. Fourth Assessment Report of the IPCC. Cambridge University Press, Cambridge.

Judd, A., 2001. Pockmarks in the UK sector of the North Sea. *Technical Report TR_002*.

Judd, A., Davies, G., Wilson, J., Holmes, R., Baron, G., and Bryden, I., 1997. Contributions to atmospheric methane by natural seepages on the UK continental shelf. *Marine Geology* 137, 165-189.

Judd, A. G., 2004. Natural seabed gas seeps as sources of atmospheric methane. *Environmental Geology* 46, 988-996.

Judd, A. G. and Hovland, M., 2007. *Seabed Fluid Flow*. Cambridge University Press, New York.

Karl, D. M., Beversdorf, L., Bjorkman, K. M., Church, M. J., Martinez, A., and Delong, E. F., 2008. Aerobic production of methane in the sea. *Nature Geoscience* 1, 473-478.

Keppler, F., Hamilton, J. T. G., Bräß, M., and Röckmann, T., 2006. Methane emissions from terrestrial plants under aerobic conditions. *Nature* 439, 187-191.

Kvenvolden, K. A. and Rogers, B. W., 2005. Gaia's breath--global methane exhalations. *Marine and Petroleum Geology* 22, 579-590.

McCartney, B. S. and Bary, B. M., 1965. Echo-sounding on probable gas bubbles from the bottom of Saanich Inlet, British Columbia. *Deep Sea Res.* 12, 285-294.

Merewether, R., Olsson, M. S., and Lonsdale, P., 1985. Acoustically Detected Hydrocarbon Plumes Rising From 2-km Depths in Guaymas Basin, Gulf of California. *Journal of Geophysical Research* 90, 3.075-3.085.

Niemann, H., Elvert, M., Hovland, M., Orcutt, B., Judd, A., Suck, I., Gutt, J., Joye, S., Damm, E., Finster, K., and Boetius, A., 2005. Methane emission and consumption at a North Sea gas seep (Tommeliten area). *Biogeosciences* 2, 335-351.

Ohle, W., 1960. Fernsehen, Photographie und Schallortung der Sedimentoberfläche in Seen. *Arch. Hydrobiol.* 57, 135-160.

Otto, L., Zimmerman, J. T. F., Furnes, G. K., Mork, M., Saetre, R., and Becker, G., 1990. Review of the physical oceanography of the North Sea. *Netherlands Journal of Sea Research* 26, 161-238.

Platt, U., Allan, W., and Lowe, D., 2004. Hemispheric average Cl atom concentration from 13C/12C ratios in atmospheric methane. *Atmos. Chem. Phys.* 4, 2393-2399.

Pohlmann, T., 1996. Calculating the annual cycle of the vertical eddy viscosity in the North Sea with a three-dimensional baroclinic shelf sea circulation model. *Continental Shelf Research* 16, 147-161.

Prather, M. J., 2001. Atmospheric chemistry and greenhouse gases. In: Houghton, J. T., et al. (eds.), *Climate Change 2001: The Scientific Basis. Contribution of Working Group I to the Third Assessment Report of the Intergovernmental Panel on Climate Change,* Cambridge University

Rehder, G., Keir, R. S., Suess, E., and Pohlmann, T., 1998. The Multiple Sources and Patterns of Methane in North Sea Waters. *Aquatic Geochemistry* 4, 403-427.

Renard, V. and Allenou, J. P., 1979. Sea Beam multibeam echo sounding on Jean Charcot: Description, evaluation and first results. *Int. Hydr. Rev.* 56, 36-57.

Rigby, M., Prinn, R. G., Fraser, P. J., Simmonds, P. G., Langenfelds, R. L., Huang, J., Cunnold, D. M., Steele, L. P., Krummel, P. B., Weiss, R. F., O'Doherty, S., Salameh, P. K., Wang, H. J., Harth, C.M., Mähle, J., and Porter, L.W., 2008. Renewed growth of atmospheric methane. *Geophys. Res. Lett.* 35.

Schroot, B. M., Klaver, G. T., and Schüttenhelm, R. T. E., 2005. Surface and subsurface expressions of gas seepage to the seabed--examples from the Southern North Sea. *Marine and Petroleum Geology* 22, 499-515.

Schumacher, D. and Abrams, M. A., 1994. Hydrocarbon Migration and its Near-Surface Expression. In: Thrasher, J., Fleet, A. J., Hay, S. J., Hovland, M., and Düppenbecker, S. Eds. *Understanding Geology as the Key to Using Seepage in Exploration: The Spectrum of Seepage Styles*. The American Association of Petroleum Geologists, Oklahoma.

Shakhova, N., Semiletov, I., and Panteleev, G., 2005. The distribution of methane on the Siberian Arctic shelves: Implications for the marine methane cycle. *Geophys. Res. Lett.* 32.

Simpson, J. H. and Hunter, J. R., 1974. Fronts in the Irish Sea. *Nature* 250, 404-406.

Suess, E., Torres, M. E., Bohrmann, G., Collier, R. W., Greinert, J., Linke, P., Rehder, G., Trehu, A., Wallmann, K., Winckler, G., and Zuleger, E., 1999. Gas hydrate destabilization: Enhanced dewatering, benthic material turnover and large methane

plumes at the Cascadia convergent margin. *Earth and Planetary Science Letters* 170, 1-15.

Suess, E., Torres, M. E., Bohrmann, G., Collier, R. W., Richert, D., Goldfinger, C., Linke, P., Heuser, A., Sahling, H., Heeschen, K., Jung, C., Nakamura, K., Greinert, J., Pfannkuche, O., Trehu, A., Klinkhammer, G., Whiticar, M. J., Eisenhauer, A., Teichert, B., and Elvert, M., 2001. Sea floor methane hydrates at Hydrate Ridge, Oregon. In: Paull, C. K. and Dillon, W. P. Eds., *Natural Gas Hydrates: Occurrance, Distribution, and Detection*. American Geophysical Union, Washington, DC.

Turrell, W. R., Henderson, E. W., Slesser, G., Payne, R., and Adams, R. D., 1992. Seasonal changes in the circulation of the Northern North Sea. *Continental Shelf Research* 12, 257-286.

Flare imaging with multibeam systems: Data processing for bubble detection at seeps

Schneider von Deimling, J.[1, 4]; Brockhoff, J.[2]; Greinert, J.[3, 4, 5]

[1] Leibniz Institute for Baltic Sea Research Warnemünde (IOW), Seestrasse 15, 18119 Rostock, Germany

[2] L-3 Communications, ELAC Nautik GmbH, Neufeldtstrasse, D-24118 Kiel, Germany

[3] Renard Centre of Marine Geology at Ghent University, Krijgslaan 281, B-9000 Ghent, Belgium

[4] Leibniz Institute of Marine Sciences (IFM-GEOMAR), Wischhofstrasse. 1-3, 24148 Kiel, Germany

[5] now at Royal Netherlands Institute for Sea Research (NIOZ), P.O. Box 59, 1790 AB, Den Burg (Texel), Netherlands

published in *Geochem., Geophys., Geosyst.* (*G-cubed*), 2007, doi:10.1029/2007GC001577

Abstract

Multibeam sonar surveys have been conducted since their invention in the 70s, however mainly reflections from the seafloor were considered so far. More recently, water column imaging with multibeam is becoming of increasing interest for fisheries, buoy, mooring or gas detection in the water column. Using ELAC SEA BEAM 1000 data we propose a technique to detect gas bubbles (flares) although this system is originally not designed to record water column data. The described data processing represents a case study and can be easily adapted to other multibeam systems.

Multibeam data sets from the Black Sea and the North Sea show reflections of gas bubbles that form flares in the water column. At least for reasonably intense gas escape the detection of bubbles is feasible. The multibeam technique yields exact determination of the source position and information about the dimension of the gas cloud in the water. Compared to conventional flare imaging by single beam echo sounders the wide swath angle of multibeam systems allows the mapping of large areas in much shorter time.

Keywords: Multibeam; sonar; flare imaging; bubbles; acoustic data processing; methane seeps.

Index Terms: OCEANOGRAPHY: GENERAL: 4259 Ocean acoustics; MARINE GEOLOGY AND GEOPHYSICS: 3094 Instruments and techniques, 3004 Gas and hydrate systems, OCEANOGRAPHY: PHYSICAL: 4562 Topographic/bathymetric interactions

Introduction

Multibeam sonar technology was developed in the 1970s to map the seafloor more efficiently than with single beam surveys. Since its first deployment in 1977 (SEA BEAM, R/V Jean Charcot), systems have improved tremendously with regard to coverage and resolution resulting in a maximum of 150° opening angle and beam widths of less than 1°.

So far, multibeam applications have mainly been used to gather information about the seafloor; because of computer and data storage limitations water column information could not be recorded in the past.

Bottom detection algorithms (BDA) extract the 'valuable' data as water depth and amplitude/backscatter values of the seafloor but at the same time disregard almost any water column information irreversibly.

Meanwhile, today's computer technology allows recording and storing of huge amounts of data and water column imaging (WCI) swath sonars are feasible. The growing interest in WCI with multibeam sonar systems is shown in the increasing implementation of WCI in modern multibeam systems (e.g. ELAC swept beam 3012, Kongsberg Ex-Simrad raw data Logger, latest Atlas Hydrosweep DS). The field of applications is widespread and covers fisheries (MAYER et al., 2002), buoy, mooring and mine detection as well as the detection of natural bubble releasing seepage (SCHMALE et al., 2005; NAUDTS et al., 2006; GREINERT et al., 2006).

In the following, we will concentrate on the hydroacoustic detection of natural gas escape (flare imaging), a phenomenon that occurs globally in coastal deposition environments, major deltas, or hydrocarbon-bearing sedimentary basins on the continental shelves and slopes (HOVLAND and JUDD, 1988; JUDD and HOVLAND, 2007). Gas seepage is frequently linked to gas hydrate deposits (JUDD et al., 2002). We will present data from a seep area in the Black Sea and a gas well blow-out site in the North Sea. At both sites, gas bubbles of mm to cm size issue from the seafloor are released in 90 to 240 m water depth. We will show that information about the water column can even be obtained using multibeam systems without WCI support. The phenomenon of seafloor masking as well as special processing and 3D visualization techniques will be described below.

Background and methods

Interference of bubbles with hydroacoustic systems

The detrimental influence gas bubbles have on the quality of sonar surveys, e.g. as reverberation or damping, is well known. In many cases bubbles are carried into the surface water through breaking waves and the vessel movement itself. If a certain threshold of free gas is reached in the vicinity of the transducers, the transmission of acoustic energy is blocked, which results in a total failure of the sonar system. However, below 10 to 20 m water depth the effect of atmospheric air bubbles can be neglected (LURTON, 2002).

The situation is different when bubbles rise from the seafloor. In most cases, the bubbles will not reach the transducer and the transmission of energy into the water will not be disturbed. But since bubbles act as strong reflectors, they can be misinterpreted as bottom signals depending on environmental circumstances and the multibeam system used.

The strong impact of bubbles on acoustic wave propagation is based on the great impedance difference between water and free gas phase. If a bubble is big enough (radius must be considerably bigger than the wavelength), much of the wave energy is backscattered. This is especially true for an ideal sphere since any incident wave will hit the sphere perpendicular to its surface. Accordingly, bubbles can be detected in monostatic setups. Bigger bubbles (>1 mm) will not behave like ideal spheres, they are elliptically shaped and expose a larger area towards the incident wave from above (CLIFT et al., 1978). At a certain frequency f_{res}, bubbles become resonant depending on bubble size and pressure. In this case the bubble acts as a resonator with part of the energy being damped where the remaining part is transmitted as waves of f_{res} in any direction. The differential backscattering strength towards the transducer reaches a maximum.

For the given frequencies (50 and 180 kHz) and depths (90 to 250 m) of our field data, the critical radii for resonance are smaller than 0.3 mm. Direct bubble size distribution measurements at seeps (GREINERT and NÜTZEL, 2004; LEIFER and BOLES 2005) suggest hardly any bubbles < 0.5mm exist. Visual observations in the Black Sea by submersible (MICHAELIS et al., 2002; MCGINNIS et al., 2006) confirmed that bubbles are typically several mm in size. Nevertheless, as most rising bubbles from ‘normally’ active seeps will not reach the sea surface (MCGINNIS et al., 2006) because of dissolution, bubbles should become resonant at a certain depth. If many bubbles are close to each other (closer than the wavelength), multiple backscattering will occur (CLAY and MEDWIN, 1977) changing the received signal strength completely.

The detection of bubbles with conventional multibeam systems strongly depends on the implemented bottom detection algorithm (BDA), filter routines, data storage capacity apart from a sufficient amount of bubbles in the water. In conventional systems, bubbles appear as bottom signal spikes if the data are not filtered by the system at a very early stage. Particularly the BDA is critical for our purpose as discussed in the following.

Description of the system used

The multibeam used was a SEA BEAM 1000 (L3 ELAC-Nautik GMBH, 2003) with 126 beams, 3x1.5° beam angle mounted as 120° or 157° system in the moon pool. On R/V Poseidon the system was equipped with 50 kHz transducers (120° swath angle) and on R/V Alkor with 180 kHz transducers (157° swath angle). The system was motion compensated by an IXSEA 3000 unit fixed directly above the transducers in the moon pool. This unit also provided heading data. The sound velocity at the transducers was taken from a MiniSVP (Valeport). Positioning was supplied by the ship's GPS.

Data were recorded by the experimental “Water Column Imaging” version of Hydrostar-Online (HSO) by ELAC-Nautik. This version was adapted for IFM-GEOMAR by ELAC-Nautik in 2004 to record the entire signal trace of one of the 42 physically transmitted beams. Usually, the center beam was chosen for recording and for the online display of the water column signal (comparable to a normal single beam echo sounder). The most critically discriminating parameter between echoes from the seafloor and echoes reflected by bubbles was the quality factor, assigned by the SONAR processing. For a better understanding of this step we provide a more detailed explanation of the BDA below.

In general, the BDA of the SEA BEAM 1000 series is designed to retrieve echoes most likely returned from the seafloor and to reject any other echo. Once a sounding is accepted as a feasible seafloor signal, it is assigned a quality flag to provide information about the detection reliability for later data analysis. The signal output from the beam former is the input to the BDA. This amplitude time series contains signals from the seafloor echo as well as echoes from the water column like bubbles or fish (Figure 1).

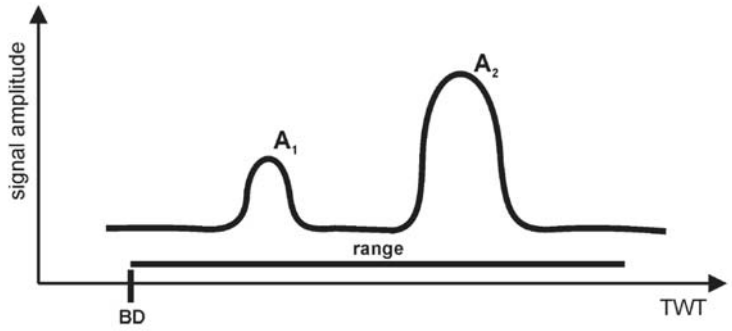

Figure 1: Schematic time series of the envelope of two echo signals, from a bubble cloud (A1) and the seafloor (A2). The block depth (BD) and the range determine the relevant time series (TWT is two-way- traveltime).

The BDA is implemented as a convolution of a customized response function with the beam formed amplitude time series.

The response function accounts for transmit pulse length and pulse widening with increasing grazing angle. The resulting time series is analyzed for maxima which determine the two-way travel time, signal amplitude and a quality factor for each beam. If more than one echo (maximum) is received, the BDA selects the most feasible one, which is normally the one with the highest amplitude. Quality factors of 1 to 4 are assigned to each selected signal using the ratio between the second and first strongest signal received in time (Table 1). Quality 4 describes data where this ratio is bigger than 1.

Table 1: Quality flags attached to the data by the SEA BEAM 1000 electronic (SEE) and HSO, respectively.

Quality flag	Pattern	Detection domain
0	Unrealistic Slope	Space
1-4	$A_2 > A_1$	Time/Amplitude
5	$A_1 = A_2$	Time/Amplitude
6,7	$A_2 < A_1$	Time/Amplitude
8, 9	No echo, internal error	

In case of two equally strong returns, the BDA selects the one that fits best to the previously measured beam and assigns a quality of 5. Sometimes the second strongest signal fits considerably better with the previously measured beam and thus is selected as more feasible despite its lower amplitude. The BDA algorithm incorporates a hysteresis to prevent oscillating between two feasible values, comparable to clutter filter often found in RADAR applications. The quality factors assigned in this case are 6 or 7 depending on the ratio between the finally selected and the strongest signal. Quality values of 8 and 9 indicate errors during the depth analysis or beams without feasible returns. Finally a quality factor of 0 is assigned if the BDA indicates a reliable seafloor signal but the slope to neighboring beams of the same swath is too steep.

Data processing

The data were processed applying correct sound velocity profiles and system corrections such as roll bias and exported to be visualized in *Fledermaus* in 3D. It is critical that all data are used, particularly those flagged with quality 0, 5, 6 and 7 by the system. Data points flagged with quality 0 (q0) are most likely to present bubbles. If there is a dense bubble cloud, the transmitted sound waves are strongly damped and bottom reflections become weak (q5, q6, q7).

Standard post processing techniques, e.g. median or mean filtering, standard grid interpolation or the novel CUBE (CALDER and MAYER, 2003) should be avoided. These post processing steps are well adapted for seafloor map generation but suppress water column data. Shallow-pass filter routines might be applied before 3D presentation.

Field data

Blow-out site, North Sea

During a cruise with R/V Alkor (Alk 259, June 2005) we investigated a leaking gas well in the North Sea at about 95 m water depth (Figure 2).

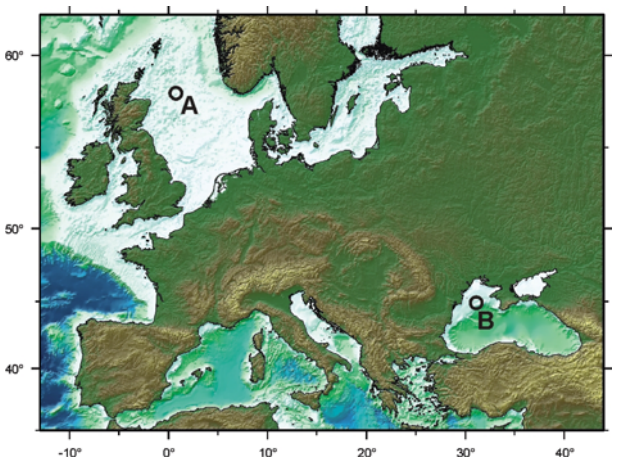

Figure 2: Locations of the working areas (A) in the North Sea (blow-out site) and the Dnepr shelf area in the Black Sea (B).

This site has been leaking since 1990 and was found to be still active in 1994 (REHDER et al., 1998) and during our studies in June 2005. Captured centimeter-sized gas bubbles at the sea surface showed a gas composition with more than 60 % methane. Up-welling process could be identified due to turbulent mixing patterns in temperature and density profiles, which were measured during CTD-casts in the vicinity of the blow-out. Because of this, the blow-out site must be regarded rather as a gas plume than a gas flare. At the sea surface it caused a bubble patch of 30 m in diameter well visible from a greater distance. In figures 3a and 3b, post processing (i.e. incorporation of bad-flagged data) for finding free gas was applied. Well visible are data that form an almost vertical column with the highest data points at 7 m water depth. Color coded for the beam number (Figure 3a), it becomes obvious that with increasing distance to the seafloor the beams sequentially belong to the outer parts of the swath. At the same time, the data quality changes from bad data (red) to unrealistic slope data (yellow) for the highest data points (Figure 3b). The position where bubbles have been observed at the sea surface fits precisely with the topmost data points. This alone may prove that these data points are caused by bubbles; however amplitude data show that these data points indeed have relatively high values, which can be expected from several millimeters to cm-sized bubbles. The bubble abundance is so high that they physically mask the seafloor to be reached by the transmitted pressure wave. The large number of data points with quality factor 0 (extreme slope) prove conventional and automatic data processing would have deleted most of the data indicative for bubbles.

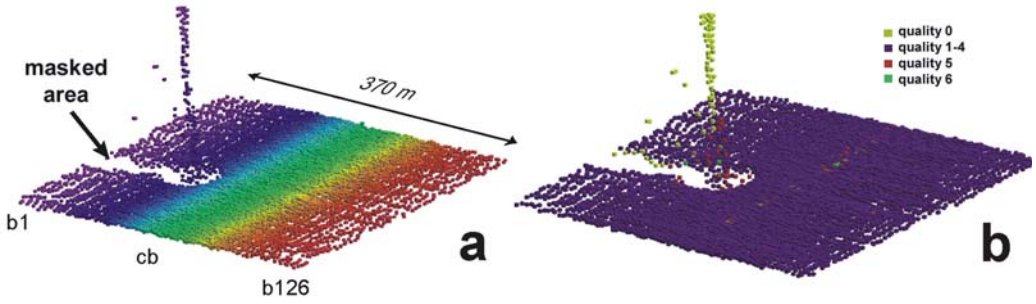

Figure 3: Multibeam data from the blow-out site of one single line (180 kHz, vertical exaggeration: 2.8). Image (a) shows data color coded by beam number ranging from beam 1 (b1, portside) to beam 126 (b126, starboard side); cb is the center beam. Image (b) shows the same data as (a) but is color coded by quality.

Knowing that the bad quality data high up in the water column are caused by reflections of bubbles in the bubble plume, it is possible to map the total dimension of the plume. This requires insonification of the area from many different directions and incident angles to account for the geometric masking effect. Figure 4 shows the compiled data set recorded from different incident angles of several survey lines. The grey colored seafloor was generated in a conventional way (excluding bad-flagged data and editing). The gridded data shows a circular depression, 50 m in diameter and 20 m around the actual drill hole. The depth-colored water column data are mainly caused by bad quality data similar to those shown in Figure 3b. It became clear that the gas release itself occurs in the morphologic depression. The dimension of the uppermost part of the acoustic plume correlates with visual observations of the 30 m-wide bubble patch at the sea surface (Figure 4).

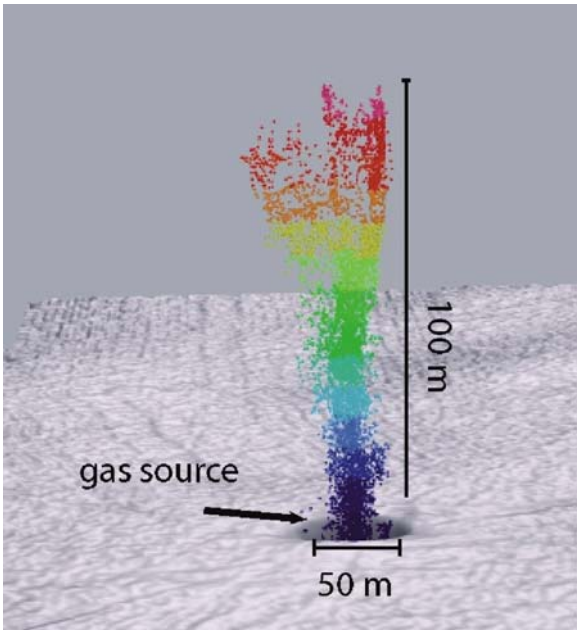

Figure 4: Data recorded during several survey lines covering the same location. The gray seafloor relief is generated in a conventional manner, whereas the depth colored soundings in the water column derive from 'bad' data. The plume forming bubbles could be detected by the multibeam system to rise up to 7 m below the sea surface. A 3D movie of this data set exists as supplemental material (2007gc001577-ms01.mpg).

Natural methane seepage, Black Sea

We applied the same method to process data from a less intense seep area in about 220 m water depth in the Black Sea (Figure 2). Seep sites in this area have been reported by several authors during the last 10 years (EGOROV et al., 1998; MICHAELIS et al., 2002; NAUDTS et al., 2006). The data presented were recovered on a research cruise with R/V Poseidon-317-3 in October 2004. One advantage of hydroacoustic studies in the Black Sea is that there are no 'disturbing' signals caused by fish below 100 m water depth as the Black Sea becomes anoxic at this depth.

A reduced data set is visualized in Figure 5 in a similar way to Figure 4. Four possible flare sites could be identified. Their positions coincide with seep locations detected during submersible dives and WCI studies carried out during multibeam mapping (yellow and purple circles, respectively in Figure 5). Again, mainly bad-flagged data contribute to the vertical excursions and might be interpreted simply as spikes of the bathymetric data.

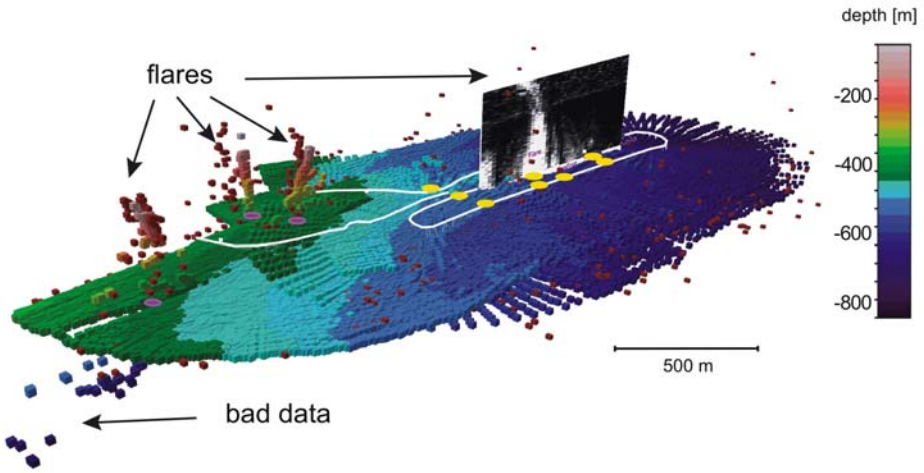

Figure 5: Multibeam depth data presentation of any quality from the Dnepr area in the Black Sea. Red dots are plotted with a small horizontal offset (for better visibility) presenting soundings flagged with quality 0. The ship track is plotted as white line. Each flare detected in the center beam is drawn as yellow circle (along-track), where the vertical image is a depicted echo time series from this center beam recorded as WCI. Flare positions detected by the submersible JAGO are shown as purple circles. A 3D movie of part of this data set exists as supplemental material (2007gc001577-ms02.mpg).

Although spikes are common in multibeam data, we are convinced that these bad-flagged data are reflections by bubbles for the following reasons: (A) Visual observation by submersible (Figure 5, purple circles) and WCI of the centre beam (Figure 5, yellow circles)

provided ground truthing for several flares along the ship's track. Additional flares off the ship's track but inside the multibeam swath coverage are likely to occur. (B) Applying the same postprocessing technique for data from areas where no active seepage was found by visual or WCI studies, we did not find bad-flagged data positioned high in the water column. (C) The bad-flagged data systematically plot exceptionally high above the seafloor and resemble the shape of a flare.

Comparing the WCI flare detection of the recorded centre beam (Figure 5, yellow ellipses) and the multibeam data, WCI provides proof of the occurrence of free gas. The great advantage of using multibeam data is the large coverage. The combination of both methods allows recognition and mapping of bubble release/flares of a large area parallel to normal multibeam mapping.

Summary and conclusion

We propose a processing procedure for finding gas flares in the water column with multibeam systems. This procedure makes use of the fact that the strong reflectivity of gas bubbles for acoustic waves leads to bubbles being misinterpreted as bottom reflections by the multibeam system. Depending on the system bottom detection algorithm, the strong reflections are recorded and might be flagged as bad or suspicious. During conventional multibeam postprocessing those data are typically not used for further processing. But visualizing such bad-flagged data in a raw data presentation is a very effective way for finding gas in the water column. Two data sets from sites where intense bubble release has been identified visually or by WCI show flare-shaped reflections caused by bubbles.

The steered narrow beam of multibeam systems allows the exact determination of the echo origin and therefore allows exact positioning of the gas source at the seafloor. Seafloor masking due to strong backscatterers above the seafloor can be used as additional indication for bubbles. However, for 3D mapping of bubble plumes the area has to be insonified from every direction. Doing this, a clear relation between the gas releasing spot and geological features such as pockmarks, ridges or (on a larger scale) mud volcanoes is possible. Huge amounts of multibeam data exist especially from the continental shelf and margin where gas escape is most likely to occur. Adapting the described processing and visualization procedure should be possible for e.g. older ATLAS Hydrosweep and RESON data as these systems also record(ed) several quality values in each beam. Simrad systems eliminate suspicious data (bubbles) in real time (person comm. Torgrim Eldevik, Kongsberg). Thus, former Simrad data sets are not very useful for gas detection in the water column. Reprocessing of data could be used for extensive flare imaging along continental margins for the detection of gas reservoirs deeper in the sediment supplying gas that migrates along

geological pathways towards the seabed surface. At the same time this method can be used to detect leaking gas pipelines monitored by multibeam carrying AUVs.

Acknowledgments

The authors would like to thank the German Government (BMBF) for supporting our research financially through a grant (COMET, 03G0600D) and the EU for supporting Jens Greinert with a Marie Curie Fellowship (MOIF-CT-2005-007436). Furthermore, we would like to thank Boris Schulze, Daniel Wendorff (L3 Communication ELAC-Nautik GmbH) and Wilhelm Weinrebe (IFM-GEOMAR) for their great help with software support/adaptations and scientific input. Finally, we would like to thank the crew and the scientists who helped during the cruises with R/V Poseidon and R/V Alkor. This is publication no. GEOTECH - 254 of the R&D-Programme GEOTECHNOLOGIEN.

References

Calder, B. R. and Mayer, L. A., 2003. Automatic processing of high-rate, high-density multibeam echosounder data. *Geochemistry Geophysics Geosystems* 4.

Clay, C. S. and Medwin, H., 1977. *Acoustical oceanography: Principles and Applications*. John Wiley & Sons, New York.

Clift, R., Grace, J. R., and Weber, M. E., 1978. *Bubbles, Drops, Particles*. Academic Press, New York.

Egorov, V., Luth, U., Luth, C., and Gulin, M. B., 1998. Gas seeps in the submarine Dnepr paleo-delta, Black Sea: acoustic video and trawl data. *Bericht aus den ZMK* Reihe E, 14, 11-22.

GmbH, L.-C. E. N., 2003. Shallow and Medium Water Multibeam SEA BEAM 1000, technical handbook, Kiel, Germany.

Greinert, J., Artemov, Y., Egorov, V., De Batist, M., and McGinnis, D., 2006. 1300-m-high rising bubbles from mud volcanoes at 2080m in the Black Sea: Hydroacoustic characteristics and temporal variability. *Earth and Planetary Science Letters* 244, 1-15.

Greinert, J. and Nützel, B., 2004. Hydroacoustic experiments to establish a method for the determination of methane bubble fluxes at cold seeps. *Geo.-Marine Letters* 24, 75-85.

Hovland, M. and Judd, A. G., 1988. Seabed pockmarks and seepages. Graham and Trotman, London.

Judd, A. G. and Hovland, M., 2007. *Seabed Fluid Flow*. Cambridge University Press, New York.

Judd, A. G., Hovland, M., Dimitrov, L. I., García Gil, S., and Jukes, V., 2002. The geological methane budget at Continental Margins and its influence on climate change. *Geofluids* 2, 109-126.

Leifer, I. and Boles, J., 2005. Measurement of marine hydrocarbon seep flow through fractured rock and unconsolidated sediment. *Marine and Petroleum Geology* 22, 551-568.

Lurton, X., 2002. *An Introduction to Underwater Acoustics - Principles and Application*. Springer.

Mayer, L., Li, Y., and Melvin, G. D., 2002. 3D visualization for pelagic fisheries research and assessment. *ICES Journal of Marine Science* 59, 216-225.

McGinnis, D. F., Greinert, J., Artemov, Y., Beaubien, E., and Wuest, A., 2006. Fate of rising methane bubbles in stratified waters: How much methane reaches the atmosphere? *JGR* 111, 1-15.

Michaelis, W., Seifert, R., Nauhaus, K., Treude, T., Thiel, V., Blumenberg, M., Knittel, K., Gieseke, A., Peterknecht, K., Pape, T., Boetius, A., Amann, R., Jorgensen, B. B., Widdel, F., Peckmann, J. R., Pimenov, N. V., and Gulin, M. B., 2002. Microbial reefs in the Black Sea fueled by anaerobic oxidation of methane. *Science* 297, 1013-1015.

Naudts, L., Greinert, J., Artemov, Y., Staelens, P., Poort, J., Van Rensbergen, P., and De Batist, M., 2006. Geological and morphological setting of 2778 methane seeps in the Dnepr paleo-delta, northwestern Black Sea. *Marine Geology* 227, 177-199.

Rehder, G., Keir, R. S., Suess, E., and Pohlmann, T., 1998. The Multiple Sources and Patterns of Methane in North Sea Waters. *Aquatic Geochemistry* 4, 403-427.

Schmale, O., Greinert, J., and Rehder, G., 2005. Methane emission from high-intensity marine gas seeps in the Black Sea into the atmosphere. *Geophys. Res. Lett.* 32, doi: 10.1029/2004GL021138.

Acoustic imaging of natural gas seepage in the North Sea: Sensing bubbles under control of variable currents

Schneider von Deimling, J.[1, 5]; Greinert, J.[2, 5, 6]; Chapman, N. R.[3]; Rabbel, W.[4]; Linke, P.[5]

[1] Leibniz Institute for Baltic Sea Research Warnemünde (IOW), Seestrasse 15, 18119 Rostock, Germany

[2] Renard Centre of Marine Geology at Ghent University, Krijgslaan 281, B-9000 Ghent, Belgium

[3] Univ. of Victoria, School of Earth and Ocean Sciences, P. O. Box 3055, Victoria, BC V8W 3P6, Canada

[4] University CAU Kiel, applied geophysics, Otto-Hahn-Platz 1, 24118 Kiel, Germany

[5] Leibniz Institute of Marine Sciences (IFM-GEOMAR), Wischhofstrasse 1-3, 24148 Kiel, Germany

[6] now at Royal Netherlands Institute for Sea Research (NIOZ), P.O. Box 59, 1790 AB, Den Burg (Texel), Netherlands

submitted May 2009 to *Limnology and Oceanography Methods*

Abstract

In 2001 a hydroacoustic device named GasQuant was developed to monitor the temporal variability of gas bubbles rising from the seafloor. This device is integrated in a lander system and uses a wide angle horizontal looking multibeam system (180 kHz) with a swath covering 2075 m². In 2005, GasQuant was deployed at the prominent gas seep field Tommeliten (North Sea) and 52 gas seeps have been detected in the swath area and monitored for 36 hours yielding a unique high resolution temporal and spatial dataset. In order to unambiguously detect gas bubbles, their characteristic rising path, which is affected by changing water currents, was considered and appropriate visualization techniques were applied to the data. Doing so, bubbles can undoubtedly be identified. Simple transient parameters like total time of activity of each seep can not only be measured, but additionally, specific release frequencies, response to tides and interaction between neighboring seeps can be studied. Finally, the hydroacoustic results are compared to single bubble flux estimates gathered during former ROV dives to compare the two methods, and to characterize the overall gas seepage behavior of the Tommeliten seep area.

Introduction

Marine methane gas seepage is a worldwide phenomenon especially on continental margins. In shallow waters such as the North Sea the released methane has the potential to enter the atmosphere, where it acts approximately 25-fold more effectively as the same amount of CO_2 in terms of its global warming potential. Today, atmospheric methane is estimated to contribute 18 % of the total atmospheric radiative forcing (IPCC, 2007).

High amounts of organic matter are buried especially on the continental margins where under anoxic conditions methane is formed mainly via microbially mediated CO_2 reduction (biogenic methane). Alternatively methane forms at greater sediment depth and higher temperature, where organic material is thermally cracked into methane and higher hydrocarbons (thermogenic methane). At porewater overpressure conditions, methane may migrate as dissolved and/or free gas phase through the sediment following geological and sedimentological pathways. If methane accumulates and its solubility in the porewater is exceeded, microbubbles may form and will further grow depending on the environmental settings, e.g. sediment characteristics, depth, methane and other gas supply from below, and biogeochemical processes.

Already in the 1960's OHLE (1960) and MCCARTNEY and BARY (1965) observed that rising bubbles can be detected with high frequency active sonar (>3 kHz). Since then, bubbles rising from the sea or lake floor have often been detected by various acoustic systems such as singlebeam (MEREWETHER et al., 1985; HORNAFIUS et al., 1999; ARTEMOV et al., 2007), multibeam (SCHNEIDER VON DEIMLING et al., 2007) and side scan sonar (KLAUCKE et al., 2005). Because of the shape in echograms, the hydroacoustic manifestation of bubbles in the water column has been termed 'flare'. The drawback by using ship-mounted singlebeam echosounders for high resolution spatial and temporal bubble release studies is the beam angle of several degrees that results in a large footprint and low ping rate increasing with depth. The resulting limited spatial resolution and the time needed for a detailed monitoring survey limits the use of such systems. Nevertheless, singlebeam echosounders have demonstrated to be the ideal tool for finding bubble releasing seep areas and estimating flux and bubble sizes at single seeps (ARTEMOV et al., 2007). Direct sampling and video observation of gas bubbles with submersibles, ROVs and scuba divers improved our knowledge about naturally occurring bubble size spectra (LEIFER and BOLES, 2005a; LEIFER and BOLES, 2006) and the relation between rising speed, bubble size, and bubble surface character (REHDER et al., 2002). Even though gas flux measurements could be conducted during several scientific missions (TRYON et al., 2002; SAUTER et al., 2006), long-term quantitative measurements (>1 day) disclosing temporal variations and the response to e.g. pressure changes are sparsely available. Most of the experiments were conducted in very

shallow environments (MARTENS and KLUMP, 1980; BOLES et al., 2001; LEIFER et al., 2004), whereas only very few deeper deployments exist such as performed with a bubbleometer from MACDONALD et al. (1994). A better knowledge about the transient behavior of the bubble release is crucial for flux estimates. If bubble seepage is active during limited time periods only, the estimated total flux is most likely overestimated. A reference volume that is released as a vigorous transient from the seafloor is more likely to enter the atmosphere than emitted by continuous release. The reason for this is the increased bubble rising speed due to upwelling effects, as well as slower loss by diffusion due to elevated methane concentrations in the aqueous-plume (LEIFER et al., 2004). Gas ebullition is also controlled by tides and other external pressure changes. Such controls can only be examined during long-term observations.

To mitigate the limitations of vessel-mounted sonar and direct observation and sampling (submersibles, ROV, scuba divers, video-sled systems) the hydroacoustic lander-based monitoring system GasQuant (180 kHz) was developed by IFM-GEOMAR and L3-Communications ELAC-Nautik in 2001. The system is able to detect gas bubbles remotely from a great distance and does not disturb the sensible fluid flow system of the actual gas releasing spot by its weight or the measurement itself. The 60 m range of the GasQuant exceeds visual observation range especially in muddy water and has a high resolution in space (9 cm along the beam) and time (4.4 s ping interval). GREINERT (2008) gives a detailed description of the system and processing steps and shows the temporal variability of bubble release from a shelf seep site in the Black Sea. Here we present extended processing techniques used to study strength and temporal variability of 52 individual seeps at the Tommeliten Gas Field in the central North Sea using data recorded during two RV ALKOR cruises in 2005 and 2006 (*ALK259*, *ALK290*). The resulting GasQuant data will additionally serve as a base for quantitative gas flux estimates in a subsequent publication.

Materials and procedures

Bubble acoustics

The physical background of the acoustic gas bubble detection is based on the large differences in density and seismic velocity between water and gas giving rise to significant contrast in acoustic impedance. Furthermore harmonic oscillator response of gas bubbles may additionally contribute to scattering. The latter occurs with a natural frequency due to large compressibility of the gas and almost incompressible water displacement interactions. As a consequence, gas bubbles in water act as strong reflectors/scatterers and even single gas bubbles or fish can be tracked by sonar.

The backscattering cross-section σ_{bs} of a single gas bubble is defined in the $ka \ll 1$ (k=frequency dependent wavenumber) regime

$$\sigma_{bs} = \frac{a^2}{((\frac{f_{res}}{f})^2 - 1)^2 + \delta^2} \quad (1)$$

where k is the *wavenumber,* a is the radius of the bubble and f_{res} its corresponding resonance frequency. f is the operating sonar frequency and δ the so called damping constant. After MINNAERT (1933) the resonance frequency of a clean gas bubble can be calculated by

$$f_{res} = \frac{1}{2\pi a}\sqrt{\frac{3\gamma P_w}{\rho_w}} \quad (2)$$

where γ is the ratio of the specific heats of bubble gas at constant pressure (c_p) over constant volume (c_v), P_w the ambient pressure, and ρ_w the water density. If the resonance frequency f_{res} of a bubble equals the transmit frequency f of the system, then the backscattering σ_{bs} peaks and the acoustic cross-section is much higher than compared to that of a rigid object of similar geometry (geometrical cross-section). Sufficiently large bubbles cause strong backscattering even if they are not in resonance ($f_{res} \neq f$: off-resonance contribution, COMMANDER and MORITZ, 1989). Furthermore, investigation of (1) clarifies that a large single non-resonant bubble can be easier detected than a smaller single

non-resonant bubble. If a non-resonating bubble is much smaller than the acoustic wavelength, the bubble behaves as a weak Rayleigh scatterer and – depending on the Signal to Noise ratio (*S/N*) of the system – can not be resolved.

Most of the hydroacoustic bubble research during the past decades was undertaken to study the acoustic response of micrometer bubbles entrained into the surface water by wind and ships. Here, resonance effects play a crucial role at the common operating frequencies and quantifications become feasible exclusively with multi-frequency approaches (MEDWIN, 1977; VAGLE and FARMER, 1992).

In contrast, the mono-frequent GasQuant system was designed to detect bubbles in the off-resonance domain, where a linear relationship between bubble density and echo integrated intensity is expected to occur (FOOTE, 1983). GREINERT and NÜTZEL (2004) and OSTROVSKY et al. (2008) have shown that the backscatter is linearly correlated to the gas flux for specific seep bubble spectra and sonar frequencies. These results served as a base for the GasQuant system design and data interpretation. However, resonant bubbles would disturb this linear correlation. But visual observations in the study area and at other micro-seepages around the world indicate that seep bubbles typically range from 1 to 15 mm in diameter (HORNAFIUS et al., 1999; REHDER et al., 2002; LEIFER and BOLES, 2005a). These sizes are well in the off-resonance domain when using the 180 kHz transducer of GasQuant in water depths down to 1000 m.

Acoustic Methods

In the beginning of cruise *ALK259* the main goal was to find an active gas seeping area for a later deployment of the GasQuant system. Ship-mounted sonar systems are very efficient tools for finding gas seepage due to their large coverage, the high survey speed and sensitivity for gas bubble echoes. Singlebeam sonar surveying was conducted to map the flare (= active seep) distribution. Simultaneous multibeam mapping should additionally reveal free gas indications and give further insight into morphological settings, which might unfold seep-related features.

Singlebeam

A vessel mounted Kongsberg-Simrad EK 60 singlebeam sonar equipped with a 38 kHz transducer (SIMRAD ES 38b) was used for water column and flare imaging. The pulse length was set to 1 ms and the given opening angle along and across track is 6.5° and transforms into a circular footprint of 7.9 m at 70 m water depth. This sensitive sonar is suitable for flare imaging although it is operating off-resonant at the given depth and expected seep bubble radii (1-15 mm bubbles have a corresponding f_{res} between 9.1 and 0.6 kHz at this depth,

equation 2). During surveys, the gain had to be adjusted to account for changing acoustic noise level so that the display is sensitive for weak echoes but not superimposed by too much noise. To reduce noise derived from the vessel, the survey speed was reduced to 3 knots. Operating with these settings resulted in the detection of many high backscatter 'clouds'. Only those patterns showing flare-like features as pointed out by JUDD et al. (1997) and a vertical extent of at least 20 meters have been counted valid and are plotted in Figure 1 as seep position. Localizing all recorded flares and determination of their height and intensity was completed through post processing work with MYRIAX ECHOVIEW.

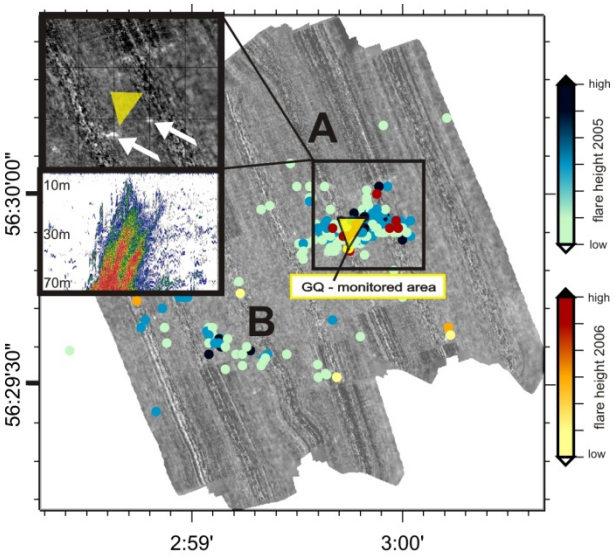

Figure 1: Each colored point represents a flare (subplot) detected in the EK 60 (38 kHz) singlebeam data of 2005 (bluish) and 2006 (reddish). The flares have been classified into low, medium and high depending on their rising height above the seafloor (~20 m absf: low; 21-40 m: medium; >40 m: high). The area monitored by GasQuant is indicated as a yellow triangle in the centre of the flare cluster A. The grayscale color coded backscatter data reveals a few patches of enhanced backscatter (white arrows, upper left subplot).

Multibeam mapping

Prior to the cruise we installed the shallow water swath multibeam system SEABEAM 1180 (L3-ELAC-NAUTIK GMBH, 2003) on RV ALKOR. This 180 kHz system covers a 153° swath angle subdivided into 3° by 3° beamformed receive angles. Consequently, the horizontal resolution at 70 m water depth is 3.66 m; the vertical resolution is estimated to be better than 0.45 m (0.5 % of the water depth). Motion compensation was achieved by using an IXSEA Octans 3000 motion reference unit. A sound velocity probe was mounted next to the transducers to guarantee correctness of sound velocity values for the beamforming. Sound velocity profiles were processed from CTD data for exact depth calculation. Within a fairly flat and featureless area the system was calibrated for roll offset.

During the postprocessing work we explicitly looked for possible seep-related features as: elevated backscatter values that might be caused by methane-derived authigenic carbonates or free gas in the seabed surface; morphological highs that might be formed from methane-derived carbonates (chemoherms) precipitated at the sediment-water interface; pockmarks; gas bubbles in the water column using the technique described by SCHNEIDER VON DEIMLING et al. (2007).

GasQuant

On the ALK259 cruise GasQuant was the most important acoustic device to monitor temporal and spatial variation of gas release. It is composed of an adapted ELAC SEABEAM 1000 multibeam electronic, a 180 kHz transducer and a data storage and system control PC. The device is mounted to a lander system (PFANNKUCHE and LINKE, 2003) and deployed video-guided with the transducer facing into the direction to seep area. The cardan-suspended transducer is placed about 3 m above the seafloor and produces a swath of 63° horizontally consisting of 21 beams with 3° by 3° beam angle each. The swath covers a range between 13 and 63 meters from the transducer resulting in a 2075 m^2 large area (Figure 2).

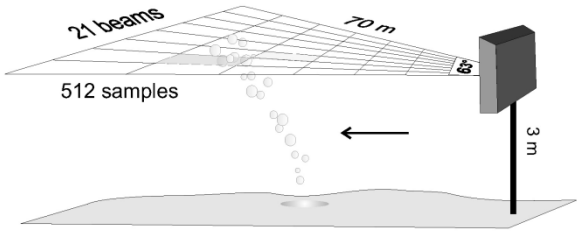

Figure 2: Schematic sketch of the deployed transducer insonifying a bubble chain. The swath covers a range of 60 m and echo time series is divided into 512 samples. Each beam is 3° wide and the overall swath width of all 21 beams is 63°. The bright and dark colored cells represent bubble activity at different times, respectively.

In operational mode, GasQuant transmits a 0.150 ms long acoustic pulse (corresponding to 0.25 m at 1500 m/s) and receives a time series of the echo-envelope for each of the 21 beams. If gas bubbles rise from the seafloor into the acoustic swath, then the respective echo intensity increases. A typical gas bubble of 10 mm diameter was reported for the working area by HOVLAND and JUDD (1988). Such a bubble rises with approximately 25 cm/s (CLIFT et al., 1978) and we can be sure that each bubble is at least insonified once in the 3° swath. Compared to a standard multibeam mapping system, which is optimized for bottom detection, the GasQuant electronic system was adapted in order to sequentially scan the water column. Each received beam is converted from analogue to digital every 128 µs resulting in 512 samples along the transducer's view (Figure 2). The system performs echo integration and stores the envelope data as 8-bit values ranging between 0 and 255. A complete scan of the swath needs 4.42 seconds which can be considered the sampling interval for each cell. The resulting data set consists of 512 x 21 time series of enveloped backscatter values. The system corrects this backscatter for geometrical spreading and absorption using a time-varying gain (TVG).

During an experimental setup (Figure 3), the system sensitivity was tested with respect to bubble size and flux rate in a similar way reported by GREINERT and NÜTZEL (2004). Even

low fluxes of only 0.2 l/minute and bubbles with a diameter of only 2 mm were clearly recognized as elevated backscatter values in GasQuant data. With increasing gas flux and number of insonified bubbles, the backscatter values increased. Relative changes in gas flux can thus be constrained at this stage of development.

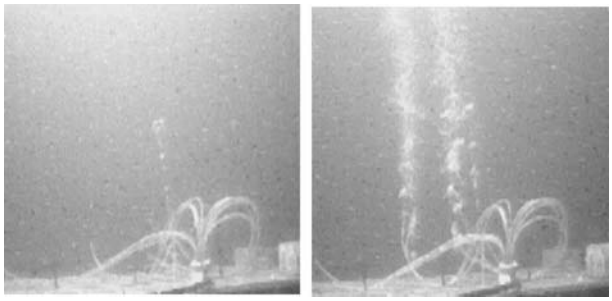

Figure 3: During a dock experiment, an artificial seep area was set up and low to medium gas flux rates of 0.2 l and 5 l per minute could be generated. Simultaneously, GasQuant insonified these bubbles and recorded backscatter data.

In addition to the GasQuant system, another lander equipped with an upward looking ADCP (2 MHz Nortek Aquadopp Profiler) was simultaneously deployed (DOS 1, 56° 30.00 N, 2° 59.62 E) in the nearby bubble free environment next to GasQuant to constrain the water velocity and backscatter target strength. Furthermore a CTD (SBE 25) was fixed to the GasQuant lander to monitor environmental changes and particularly link tidal pressure changes to the observed gas release patterns. All times are given in MESZ (= UTC +2).

Data processing of GasQuant recordings including ADCP

The GasQuant data volume, that is stored during a deployment for several days, grows large and various sources of noise close to the 180 kHz band (system self-noise, engine/hydrolic pumps, thermal noise, biologic scatter) perturbs the data. This requires postprocessing to improve the signal to noise ratio, for removal of spikes, and for easier data handling and visualization. A key feature during postprocessing was to consider current velocity (*ADCP*) effects on the data. The drift of rising bubbles is dominated by the sum of their vertical buoyancy velocity and environmental water current. If bubbles are emanating from the seafloor they become laterally shifted and if currents change direction and or speed, successive bubbles rather pass the swath at adjacent cells. As a result, bubbles from one seep are recognized in several cells of one beam and might even move between beams. During the GasQuant experiment, simultaneous ADCP measurements reveal a strong tidal impact on the current (Figure 4). Consequently, a displacement of bubbles is expected to occur. The magnitude of this shift can be estimated, e.g. a bubble of 10 mm diameter has a terminal rising velocity v_z of approximately 20 cm/s (CLIFT et al., 1978) and needs t_{up}=15

seconds to reach the acoustic main lobe at *d* (3 m) above the seafloor. Using the horizontal velocity components (v_h) from ADCP measurements the expected horizontal bubble drift can easily be calculated to be v_h x t_{up}.

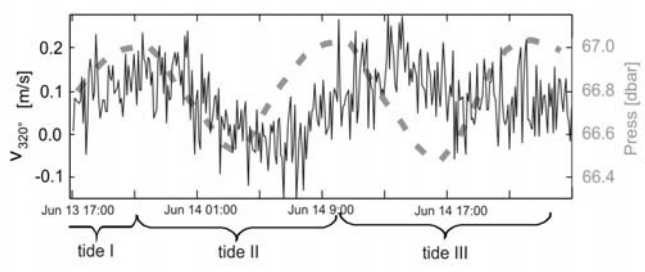

Figure 4: Combined plot showing ADCP velocity component alongtrack of the transducer's view direction towards NNW (N positive, S negative) together with CTD pressure data (dashed line) gathered during the GasQuant deployment. The entire deployment time is separated into three sections termed tide I, tide II and tide III with respect to the differing tidal cycles.

The displacement effect can be visualized in *traceplots*. Such an illustration comprises sixty backscatter amplitude time-series (traces) of adjacent cells being drawn underneath each other (Figure 5). It incorporates both the predicted bubble displacement (solid sinusoidal line) and real displacement showing up as tidally dominated sinusoidal pattern. As long as the sinusoidal curves are clearly separated from each other, each of these curves is considered to be caused by one individual seep releasing bubbles over time. This is even valid for non-continuous bubble release as long as its repetition rate is high enough to trace the sinusoidal line. The predicted and measured displacement curves agree particularly well and this similarity can be considered as an unambiguous pattern for rising gas bubbles in swath plots.

Figure 5: GasQuant dataset showing 60 trace time series (TTS) of beam number 1 corresponding to the very outer left beam (Figure 2). The respective TTS originate from adjacent samples labeled on the y-axis by sample number and distance to transducer (meter). Color-coded values correspond to GasQuant backscatter units (color bar). The entire time series comprises 36 h. Vertical green and red lines indicate moments of minimum and maximum water-level, respectively. The thin black sinusoidal re-traces #52 and the thick sinusoidal line represents the predicted bubble displacement derived from ADCP data. A zoomed subplot presentation in the lower left corner stresses underlying higher gas release frequencies, that vanish in the bulk presentation due to print/pixel resolution.

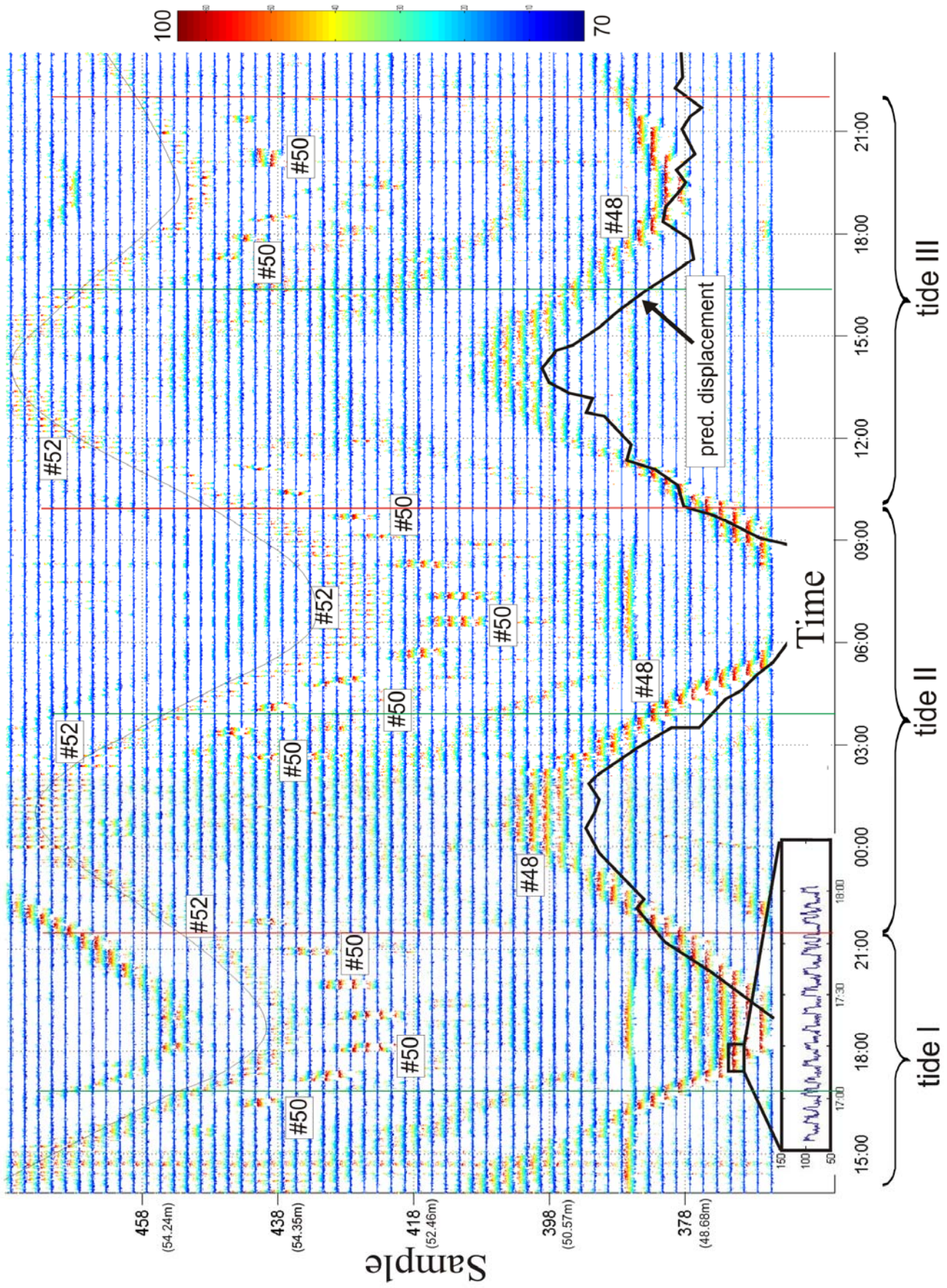
100
70
#52
#50
#48
pred. displacement
Time
tide I
tide II
tide III
15:00
18:00
21:00
00:00
03:00
06:00
09:00
12:00
15:00
18:00
21:00
Sample
458 (54.24m)
438 (54.35m)
418 (52.46m)
398 (50.57m)
378 (48.68m)

This bubble detection method works if current variations exist and are strong enough to move bubbles and cause a wavy data pattern. Tidal effects occur in all marine environments and at least small current shifts are likely. Considering the high resolution and long-term monitoring of the GasQuant system, only slight current changes are required to cause detectable shifts from one cell to another (wavy data pattern) and thus recognition of bubbles.

Automatic event detection algorithms such as correlation processing (DWORSKI and JACKSON, 1994) or 'short/long term averaging' (STA/LTA) known from seismic processing have been considered and rejected, because the visual bubble pattern recognition works quickly and reliably against erroneous interpretation.

Nomenclature

To facilitate data description several data types and descriptors have to be introduced. We define a 3D matrix composed of *GQTS* (GasQuant Target Strength) backscatter values. Its first spatial dimension is along the transducers view (along the 'samples' of the given beam, Figure 2) and addressed by sample-index *s* [1..512], the across-track beam direction by beam-index *b* [1..21], and time is the third dimension abbreviated by index *t* [1..29000]. Holding arbitrary *s* and *b* values fixed equals choosing one cell and its corresponding Trace Time Series ($TTS_{s,b,1\text{-}29000}$). A subset of this time series, e.g. $TTS_{s,b,t1\text{-}t200}$ is termed a '*sniplet*'. To analyze the activity of one seep rather than the activity of a GasQuant cell, a so called Individual Seep Time Series (*ISTS*) is introduced and explained later in the text. It represents compiled backscatter time series of adjacent cells unfolding gas releasing activity of one single seep. To decide whether an elevated backscatter signal is regarded to be caused by free gas or noise, a Detection Threshold (*DT*) has to be set. Values above *DT* are considered as *active* and the corresponding time values are summed to give the Time of Activity (*TA)* of the respective gas releasing event, whereas values below are termed *background/silent*. If *TA* steadily exceeds *DT* for 2 minutes then we define this a '*bubble burst'* of length *TA.* The signal is usually characterized by sharp edges separating the *burst* from the background. The *total TA* ($\sum TA$) includes all *active* periods of one seep during the observation time. Integration of *GQTS* values over *TA* yields the intensity of the respective bubble burst *TI* and the overall intensity $\sum TI$ of one seep spot. To better constrain the relation between *active* and *background* periods the Release Cycle Ratio *RCR* is introduced, where the numerator corresponds to the *silent* period within an *ISTS*, and the denominator to the *active* time (e.g.

a *RCR* value of 10/20 means gas release occurs every 30 time units lasting for 20 time units with 10 time units between the bursts).

Compiled presentation of many TTS is preferred for simultaneous visualization of large datasets and bubble detection as shown in Figure 5, whereas inspection of *ISTS* helps for later data analysis, e.g. measuring the seep activity ($\sum TA$), determination of its intensity ($\sum TI$) or finding the seepage response to environmental changes such as tidal pressure variation.

Filtering

To increase the *S/N* of the GasQuant data and to delete system related spikes, low pass filtering was applied. Physical parameters such as the range-dependent vertical swath width $s_v(d)$ and the bubble rising speed v_{up} were considered to design an effective filter.

With increasing distance d of a bubble to the transducer (due to the beam opening angle of 3°) the crossing of the swath takes increasingly more time and consequently one rising bubble is insonified more than once during its ascent. For instance, in 50 meters distance from the transducer the vertical swath is 2.6 m. A typical bubble with 20 cm/s ascent rate (~10 mm diameter) needs 13 s to cross the swath. The expected acoustic bubble backscattering strength should first steadily increase while entering the acoustic lobe, then peak within the main lobe and eventually decrease with its further ascent. Significant backscatter undulation within this ascent period can be considered as noise and was suppressed by a 20^{th}-order low-pass Butterworth filter designed and adapted for the changing swath geometry with $[s_v(d)/v_{up}]^{-1}$ being a cut-off frequency criterion.

Unfortunately, the raw data additionally contain spikes which result in a very broad spectrum making the low-pass filter ineffective. Thus, before applying the filter, a lower and upper intensity threshold was assigned to clip the spikes by logical treatment. The clipped values were replaced by the mode value within a 20 samples wide window around the values that had to be replaced.

Seep detection and analysis

With regard to trace plots, it was shown that bubbles may be recognized in the form of sinusoidal patterns. Doing so the observer discriminates signals from noise by utilizing elevated trace amplitudes and colors as an indicator. This visual pattern recognition technique is very quick and reliable in terms of finding constant bubble release in the large amount of GasQuant data. But for computational data analysis, e.g. the determination of TA and TI values, a numerical threshold value DT is necessary to separate silent periods and areas from active ones. To face temporal variations of the noise and changes with swath-cell position, DT was set dynamically at given times and locations. This was feasible, because in traceplots seepage appears in the form of sniplets spread over adjacent cells. These sniplets

are short compared to the total length of the entire trace (Figure 5, 6). The calculation of the local mode value of a single trace gives the local background value. DT was set by adding twice the standard deviation to the local background level. This computed DT value matches the visual decision, where the transitional color-coded value between the wavy pattern and background is chosen to be the threshold. E.g. in Figure 6a the bubble pattern plots with yellowish/reddish points ranging between 73 and 90 *GQTS*.

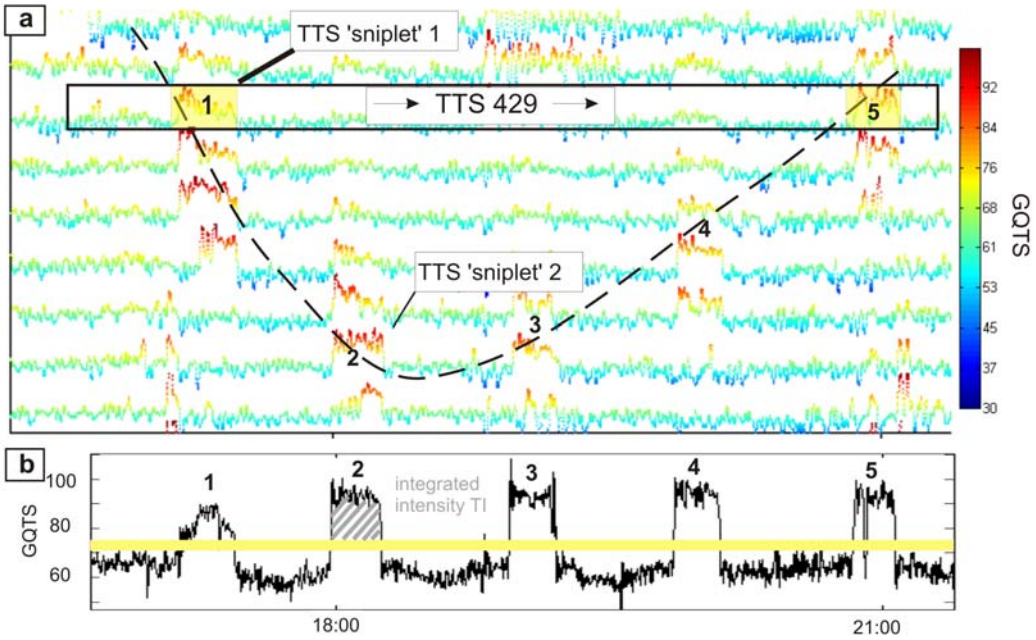

*Figure 6: (**a**) trace sub-plot from Figure 5 (tide I) showing five successive bubble bursts of seep #50 (labeled incrementally 1-5). The yellow rectangles within TTS 429 highlight relative short active periods of the single TTS 429. Enhanced signal strength can be tracked by following the wavy pattern (dashed line). Yellowish and reddish points in the vicinity of the black line are considered a signal, whereas bluish and greenish dots are considered background/noise. (**b**) ISTS representation of picked samples and times from (a). The yellow line represents the given color-coded threshold (compare color bar in (a)). TI of one bubble burst plots as a grey-shaded area at burst number 2 (1800 MESZ).*

Consequently, *DT* was set to 73 and values below are considered as noise. We only found minor differences between statistical and visual threshold setting, nevertheless the impact of small deviation of *DT* must be acknowledged. Therefore, *TA* and *TI* values were computed using min, max, and medium *DT's* (adding and subtracting 10% of *DT*). In most of the cases such threshold modifications show hardly any effect on the calculated *TA* (e.g. Figure 6a). Only in a few very noisy *ISTS* a variation of maximum of 12 % of *TA* was found. However, de- or increasing the threshold has an immediate impact on the integrated *TI* value, and, for later presentations the medium threshold was selected.

Stacking of Individual Seep Time Series (ISTS)

To obtain a complete time series that represents the bubble release activity of one seep (*ISTS*), time series values from different cells have to be merged (stacked). This is to include all those cells which are influenced by bubbles from one seep hole, but also excluding

signals of those cells which are affected by other seeps close by at different times. Thus, the sinusoidal curves consisting of raised backscatter values were manually digitized (Figure 6a). Subsequent spline interpolation between digitized points gave a continuous time series containing the picked shift magnitude of bubbles/elevated backscatter values. Eventually, the *ISTS* (Figure 6b) is computed by merging of time series values along this spline.

If elevated backscatter occurs, at least three adjacent samples are affected (Figure 6a). This is given due to the slight over-sampling effect of the transmitted 0.150 ms long pulse with regard to the sample rate (0.128 ms). In addition, the spatial dispersion of bubbles some meters above the seafloor may cause neighboring samples to inherit similar backscatter patterns. To account for matching signals in upper and lower neighbors around the spline three samples were 'stacked' and averaged ($TTS' = (TTS_{n-1} + TTS_n + TTS_{n+1})/3, n \in [2, 511]$).

This processing was accomplished with a self written MATLAB GUI capable to digitize the sinusoidal curve (Figure 6a, black spline) and to extract the requested data (Figure 6b). Compared to previously suggested processing by GREINERT (2008), the small distance between single seep holes at Tommeliten and the considerable current variations require digitization to avoid merging backscatter values originating from neighboring seeps into one *ISTS*. Moreover, the selection of active areas improves the *S/N* of the resulting *ISTS* because only those values have been stacked which include a bubble signal.

Spectral analysis

To better identify and quantify periodicities in the data, the stacked time series were transformed into the frequency domain. This was accomplished with a Fast Fourier Transform (*FFT*) algorithm run in MATLAB. This algorithm uses zero-padding and to further face potential leakage effects, some time series were cut down in length to exponential to the base 2. The *FFT* was run using Hamming windows to avoid spectral leakage caused by edges of the time series. Disturbing long term trends in the data were removed using the MATLAB built in function 'detrend'. Finally the frequency content was displayed as a powerspectrum.

Study area

The study area 'Tommeliten' is located in the 'Greater Ekofisk' area (Central North Sea, Norwegian Block 1/9) over three buried salt diapir structures, that are covered by Mesozoic and Quaternary sandy and clay-rich sediments (HOVLAND and JUDD, 1988). A seismic section reveals a gas chimney (D'HEUR, 1984) rising along a fault providing a pathway for gas migration into the surficial clay-rich layers and locally into the water column (HOVLAND and JUDD, 1988). The topmost sediment layers have been investigated by vibro-coring (NIEMANN et al., 2005). They contain four different horizons of sediments where the lowest (350–240 cm b.s.f) consists of stiff marl followed by a gassy layer of clay-silt with supersaturated CH_4 concentration (240–175 cm b.s.f) and two topmost sandy layers - depending on locality - with and without carbonate. More general information about regional geology can be found in D'HEUR (1984).

During a routine seismic survey in 1978 higher frequency acoustic data (3.5 kHz pinger) revealed both, flare-like features in the water column and acoustic turbidity indicating gas in the water and in the sediments (JUDD and HOVLAND, 2007). Early ROV expeditions in 1983 revealed seeps on a plain, sandy seabed with only occasional signs of biological activity (HOVLAND and SOMMERVILLE, 1985; HOVLAND and JUDD, 1988). Those include reef-like structures locally arising in the form of small-sized bioherms extending a few meters in diameter. Most of those gas vents have been found to be surrounded with 20 cm funnel-shaped depressions in the sandy environment.

The area of gas-charged sediments was estimated to be 120.000 m² (HOVLAND et al., 1993). Analysis of the gas composition and its methane stable carbon isotopic signature undertaken by HOVLAND and SOMMERVILLE (1985) indicate a thermogenic origin of the gas that enters the water column.

HOVLAND and SOMMERVILLE (1985), describe a total of 120 bubble seeps in the area. The seeps typically release bubbles from a circular 10 mm diameter hole in sandy sediments. The release of the approximately 10 mm diameter bubbles was estimated to be more or less constant with an average production rate of one bubble every 6 seconds. Noteworthy is an experiment documented in HOVLAND and SOMMERVILLE (1985) where one gas releasing hole was filled up with sand. After about 1.5 minutes, the bubble stream was re-established from this hole. The same area was re-surveyed 15 years later and HOVLAND (2002) reports (a) new incipient seep, (b) bacterial mats (probably Beggiatoa sp.), and (c) authigenic carbonate cemented bioherm structures.

In addition to acoustic and visual evidence of seepage, several CTD casts were conducted during *ALK259* and *ALK290* and indicate methane seepage. From water samples taken

around the GasQuant deployment site high methane concentration of up to 180 nM was measured. Isotopic signatures ($\delta^{13}C\text{-}CH_4$) from samples taken near the bottom gave -45 ‰ VPDB and support previous isotope studies.

Recent ROV (NIEMANN et al., 2005), submersible and video-sled observations (*ALK259*) have demonstrated that gas venting is still active and that the flux is strong and persistent enough to supply seep-related fauna to live and methane-derived carbonates to form.

Assessment

Flare distribution and bathymetry

Most of the time during *ALK259* the water column was monitored by the EK60 singlebeam echosounder. Online observation and post-processing of the data clearly revealed a high number of flares. They concentrate in two areas (Figure 1, blue dots). To a certain extent, the clustering derives from a sampling artefact caused by the fact that the ship spent more time at areas that have been found the most active during the cruise. To eliminate this artefact, only those flares recorded during the combined multibeam/singlebeam survey gathered during *ALK 290* (survey was performed with uniformly distributed coverage time) are plotted as well and give a similar result (Figure 1, reddish dots). Therefore, clusters *A* and *B* are considered the most intense gas emanating areas. These findings confirm the gas seepage occurrences presented by HOVLAND and SOMMERVILLE (1985) and NIEMANN et al. (2005), but additionally stress their clustered nature.

The bathymetry of the working area is flat and featureless (70 m) and slightly deepening towards the south. Small depressions were reported from video observation (HOVLAND and JUDD, 1988; NIEMANN et al., 2005) but they could not be resolved by the multibeam system. Backscatter data from *ALK290* with reduced ship speed and calm weather conditions reveal some small patches of higher backscatter (Figure 1). This might be caused by increased sediment cementation by methane-derived carbonates.

GasQuant measurements

GasQuant was deployed looking northwards within the center of the most intense gas seepage area for a total of 36 hours (Figure 1: 56° 29.89'N, 2° 59.80'E). After recovery, the GasQuant dataset was processed and visualized in large paper printouts. Supported by the respective current velocity data (ADCP) and predicted bubble paths, a total of 52 gas seeping point sources were located in *TTS* plots (Figure 5). A CTD cast within the working

area revealed an in situ temperature of 6.5°C and salinity of 33 psu at depth. Thus, a sound velocity of 1475 m was calculated for 80 dbar after FOFONOFF and MILLARD (1983) to provide precise distance of samples to the transducer (Figure 5, y-axis).

The transience of the seep activity could be further constrained by scrutinizing the corresponding *ISTS* data (Tab. 1).

In the following the acoustic imaging is illustrated and the signature of individual seeps is studied. We demonstrate GasQuant's potential to not only detect single seeps, but also to reveal their small scale temporal and spatial variability. Because of the great amount of seeps detected, we only show some of them in detail. Finally, the bulk behavior of the entire seep area is described based on the GasQuant data.

Table 1: Seep classification into continuous (by definition continuous means, that seepage activity is longer than 70 % of observation time) and non-continuous gas release types.

Release type	Continuous	Non-continuous			
		Transient			purely tidal (on/off)
		∑TA <31%	∑TA 31-50%	∑TA 50-70%	
Number (% perc.)	41 (67%)	7 (11%)	2 (4%)	1 (5%)	1(~1 %)

Individual gas escape behavior

In Figure 5 and 6 GasQuant data are visualized as *trace* plots and various release characteristics can be studied. To stress the relation to pressure changes, the in situ minimum and maximum CTD pressure data is shown as well in Figure 4 and Figure 5 (vertical lines). Seep #48 draws a continuous sinusoidal line without any interruption and can be visually interpreted as a continuous gas release from a single seep spot. A replicate but much weaker representation of this line plots 9 samples later. This is considered a 'ghost' signal caused from either multipath effects, where #48 bubble echoes travel not directly back to the sonar, but first hit the sandy seafloor to later achieve the transducer, or by the complicated forward scattering of gas bubbles (FEUILLADE and CLAY, 1999), especially if they are arrange in an equidistant manner (array effect). Zooming into the time axis of seep #48 reveals that this seep is not constantly active but characterized by short inactive periods of 3 to 5 minutes (Figure 5, subplot). Seep #50 and #52 exhibit a more pulsing and less constant gas release still having the same current-driven displacement as seep #48. During the first tidal cycle (*tide I*) #52 releases gas bubbles approximately every 3 to 5 minutes until the beginning of *tide II* (23:30), where the gas release abruptly slows down to occur every 12 minutes.

Seep #50 exhibits much longer gas escape periods with systematic linkage to the tides. Around low tide minimum (*tide I*, green line) gas release begins to produce a 15 minutes long burst, followed by several bursts of the same length and silent periods of 60 minutes (60/15 *RCR)*. At 2130 MESZ (*tide I*) this seep turns completely silent until begin of the next low tide phase (*tide II,* 0345 MESZ). Afterwards, this scheme repeats almost identically, whereas at *tide III* an exceptional long silent period of 90 minutes starts around 1900 MESZ interrupting the previous scheme; it is followed by a longer bubble escape lasting 30 minutes. The *RCR* of 90/30 is still of the same magnitude as the consistent previous 60/15 ratio. Although #50 and #52 are only 1.9 m apart, their transient release is not correlated to each other.

Figure 7 shows compiled escape patterns. E.g. seep #25 releases bubbles every 5-6 minutes which last for 3 to 4 minutes. These events show the typical bubble burst shape with distinct on and offset edges. This escape pattern remains active over the entire deployment time. During low tide (*tide II)*, seep #3 reveals a constant release between 0400-0600 MESZ but turns periodic at 0800 MESZ towards high tide. Burst length range from 1 and 5 minutes each burst followed by 2 minutes of no release. With the successive tidal cycles this sequence recurs (not shown). Such a transitional gas release pattern was also found at seep #38 where the gas release turns from constant to irregular with increasing tidal pressure (0730 MESZ). The *TA* values range between 5 and 35 minutes separated by silent intervals of 2 and 15 minutes. Such an unsteady and pulsing gas escape pattern was additionally observed at #43 and #56.

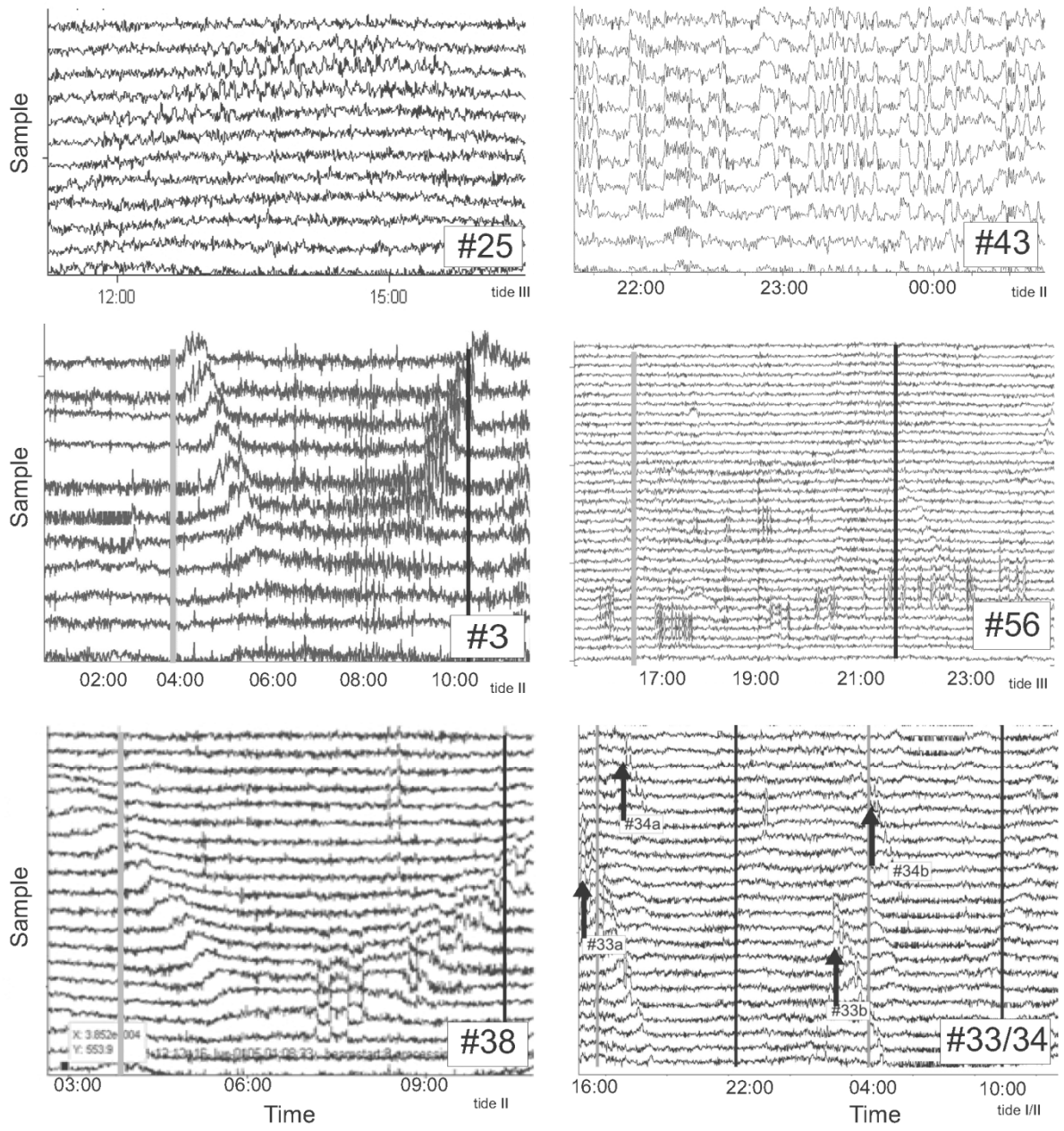

Figure 7: Compilation of various gas escape patterns. Note the differing time-scales and tidal phase in each subplot. Vertical black and gray lines indicate maximum and minimum water level, respectively. Additionally, tidal control of gas seepages is indicated by arrows.

The most prominent tidal control appears at seep #33, where gas is exclusively released during low tide (Figure 7,Figure 8). The gas release starts before low tide by initial, long bursts (Figure 8a, b). Subsequently, the backscatter intensity (Figure 8a) and the length of bubble release periods (Figure 8b) decline and the gas release totally vanishes around high tide. At the following tidal cycles this release pattern can be seen again. The neighboring seep #34 (Figure 8c, d) is tidally triggered as well, but exhibits a solitary gas release event

during water level high stands. Overall, it was found that only 1% of all discovered seeps exhibit an on-off tidal control (i.e. gas is released exclusively during low tide).

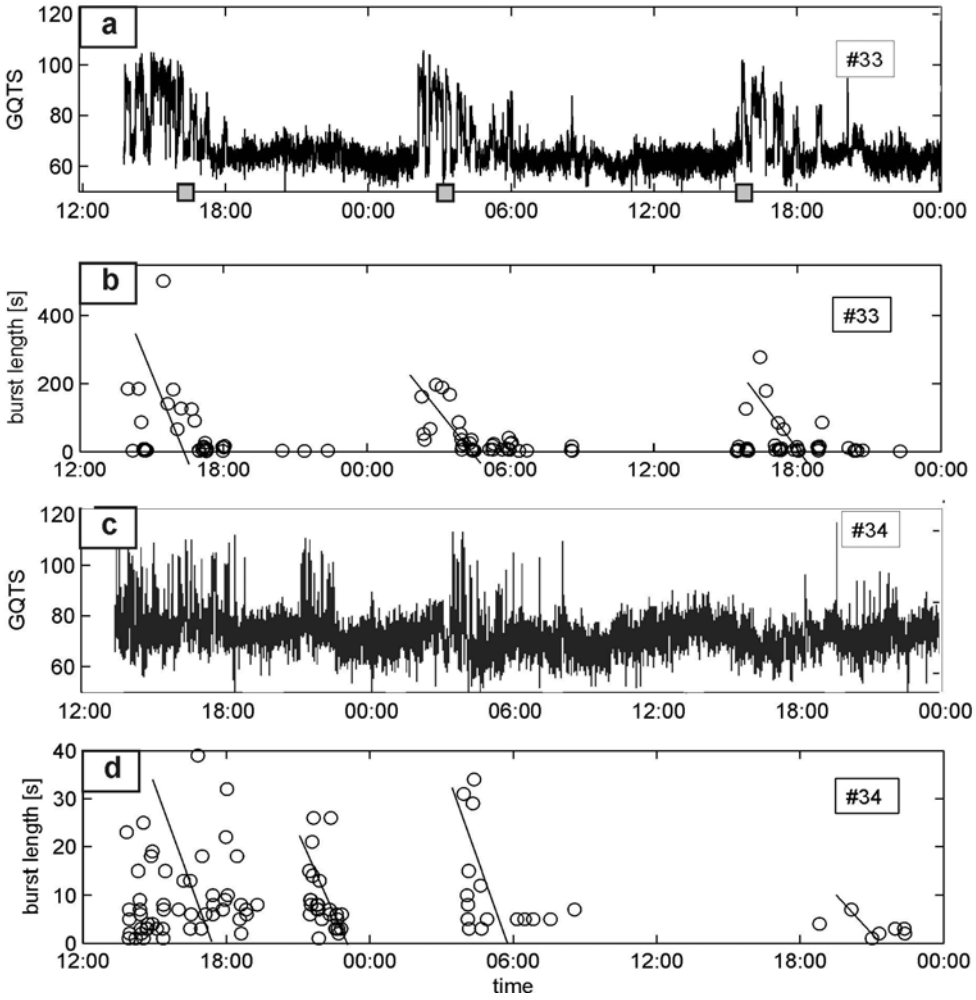

Figure 8: (a) ISTS plot of #33 (compare Figure 7) showing distinct increase of GQTS attributed to enhanced gas release occurring around minimum pressure (grey square on time axis). (b) length (seconds) of individual bubble bursts plotted versus time. Longest bursts occur at the beginning of active periods and gradually decrease towards the silent periods. (c) and (d) are similar to (a) and (b), but at 2200 MESZ a bubble burst emanates at high tide around 2200 MESZ.

Spectral analysis

To quantify the bubble release periodicities and also to overcome the high data density (t_1-t_{29000}) and limited *trace plot* resolution, FFT analyses were performed in order to resolve the periodicities, which can not be quantified visually. Combined plots (Figure 9) including time series and spectral presentation of seep #25, #50, and #52 reveal minimum (a) maximum (b) and intermediate (c) gas release periodicities.

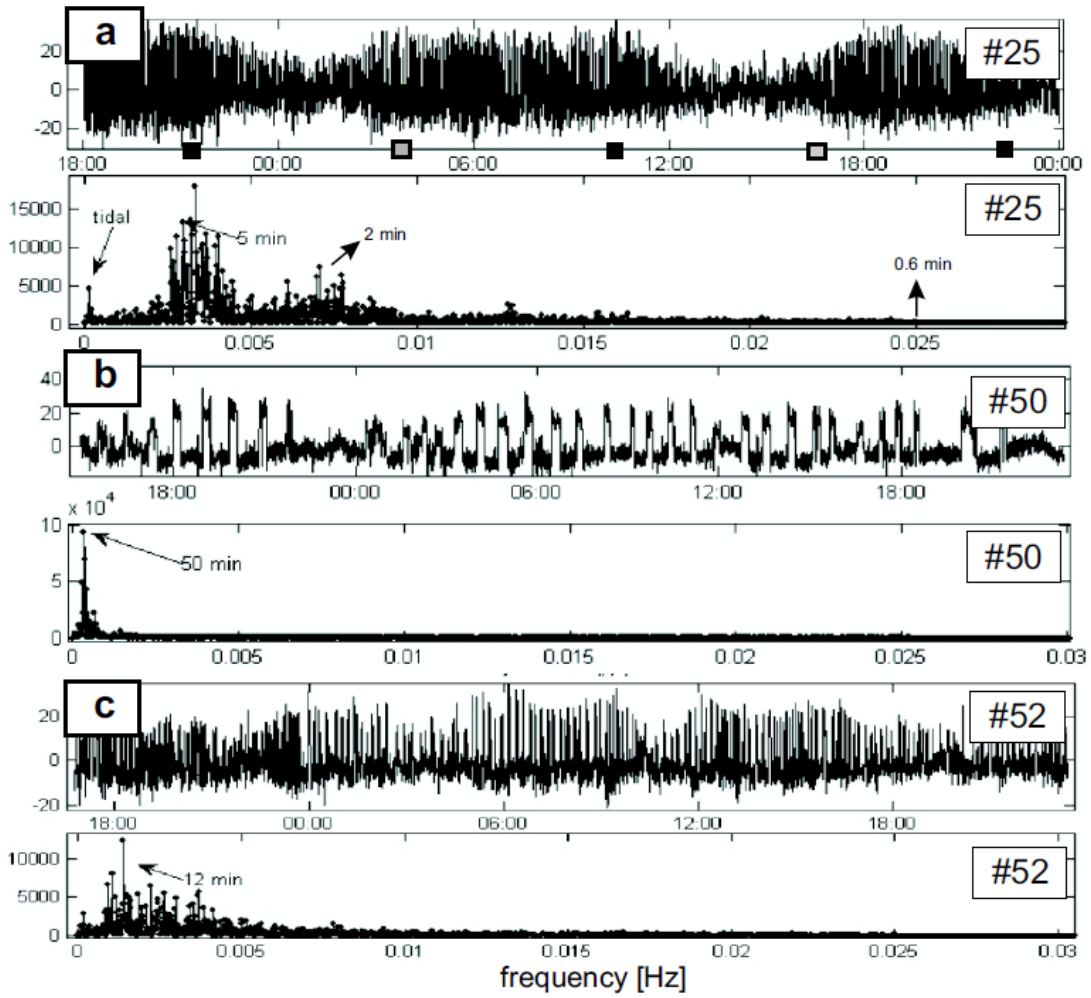

Figure 9: ISTS presentation and the corresponding powerspectrum of seep #25 (a), #50 (b), and #52 (c). The cut-off at 0.025 Hz in the frequency domain is caused by previous low-pass filtering.

Long, tide controlled fluctuations can be observed in Figure 9a. Here, the backscatter amplitude gradually increases after passing the low water level. This higher values are considered to be caused from enhanced bubble release and the high values persist until reaching water level maximum and subsequently drop down to background values. This cycle repeats during all tidal periods. This obviously tide-controlled oscillation shows up as a minor peak in the frequency domain (Figure 9a). A secondary pronounced peak at 5 minutes additionally occurs in this spectrum. When zooming into time-series very persistent bubble bursts of 5 minutes duration become visible (similar to Figure 5, subplot of seep #48).

Fifty-minute period of seep #50 can be detected in both, its time and spectral domain (Figure 9b) and confirm previous visual impressions of long bubble bursts drawn from

. A solitary peak in the frequency spectrum indicates that concurrent frequencies besides the 50 minutes peak do not exist at seep #50.

The entire GasQuant dataset was examined for preferential release frequencies by FFT analysis, and 18% of all seeps exhibit profound release frequencies in the range between 5 and 50 minutes. In addition, potential dependency of gas release frequency on tidal pressure phase was tested by computing several spectrograms. However, systematic frequency shifts over time have not been found.

Bulk gas escape behavior

GasQuant allows to exactly localize each seep hole relative to the GasQuant lander (Figure 10). The spatial distribution of the gas sources appears homogeneously distributed. Enhanced along- compared with across-beam resolution causes local seep clusters to appear aligned into the direction of the beam, even if the true seep cluster extent is not aligned.

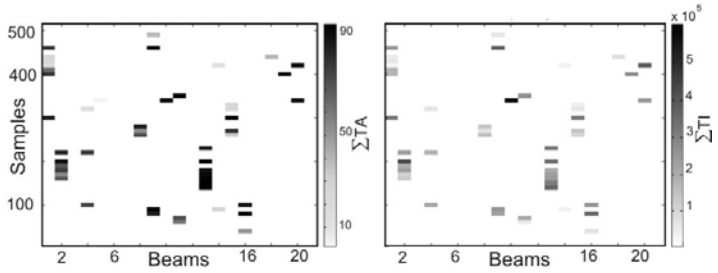

*Figure 10: Distorted topview on swath data: (**a**) distribution of total seep activities (∑TA) in percentage of observation time and (**b**) distribution of total seep intensities (∑TI) in absolute values.*

A histogram of ∑*TA* (Figure 11a) including all seeps demonstrates that the major number of seeps emanate gas continuously (see definition in Tab. 1), whereas transient seepage only marginally contributes to the ∑*TA* (Figure 11a). In terms of gas seepage intensity (∑TI), low gas seepages clearly dominate a few rare stronger gas events (Figure 11b). Such skewed distributions are fitted best by a lognormal distribution. This type of distribution often emerges in (geological) exploration and has already been mentioned in the context of seepage (WILSON et al., 1974; LUYENDYK et al., 2003; ARTEMOV et al., 2007).

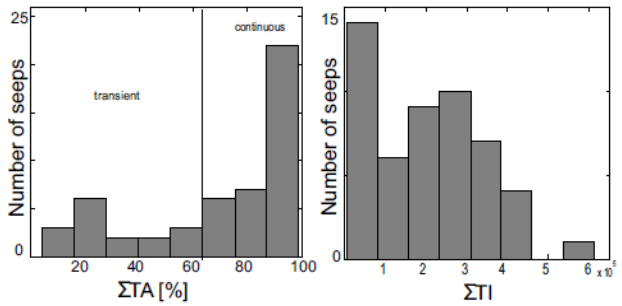

*Figure 11: (**a**) Eight bin histogram incorporating ∑TA of all seeps. By definition seeps ≥70% activity are considered continuous (**b**) eight bin histogram incorporating ∑TI of all seeps.*

Considering both, the histograms of ∑*TA* and ∑*TI* the question arises if transient seeps might emanate as much gas as continuous seepage. In terms of bulk gas escape a transient bubble burst might compensate for its reduced *TA* by more vigorous escape *TI*. To better constrain this *TI* was normalized by *TA*. The normalized *TI* only slightly increases with *TA* (Figure 12), and the obviously reduced activity of transient seepage is not compensated by major intensity.

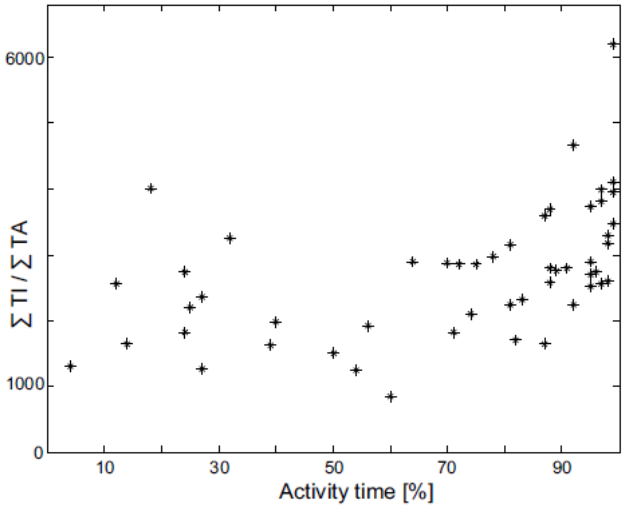

Figure 12: The ∑TI of each seep has been normalized by its ∑TA value and plotted versus percentage time of activity. No explicit trend can be discerned.

To study the transience of the bulk gas release, all *ISTS* were summed together (*GQTS'*, Figure 13a). To see potential interrelations with the ADCP backscatter or tidal pressure, those variables are additionally plotted in Figure 13 (b, c). The maximum tidal range between low and high tide was 0.7 m during the study period. A high correlation between the pressure and summed *GQTS'* exists, where GQTS' lags π/2 behind the pressure, i.e. the bulk seepage values *GQTS'* start to increase at the maximum pressure inflection point (Figure 13a) and peak, when dp/dt drops fastest (Figure 13b, arrows). The *GQTS'* value backs down to normal exactly at the pressure minimum. Around 0500 MESZ the per se silent period is interrupted by a slight excursion. At the next maximum pressure inflection point this cycle repeats except for the 0500 MESZ anomaly. The ADCP TS variable appears to be counter correlated to the ISTS and will be discussed later, whereas the absolute ADCP velocity shows no clear correlation to the GQTS'.

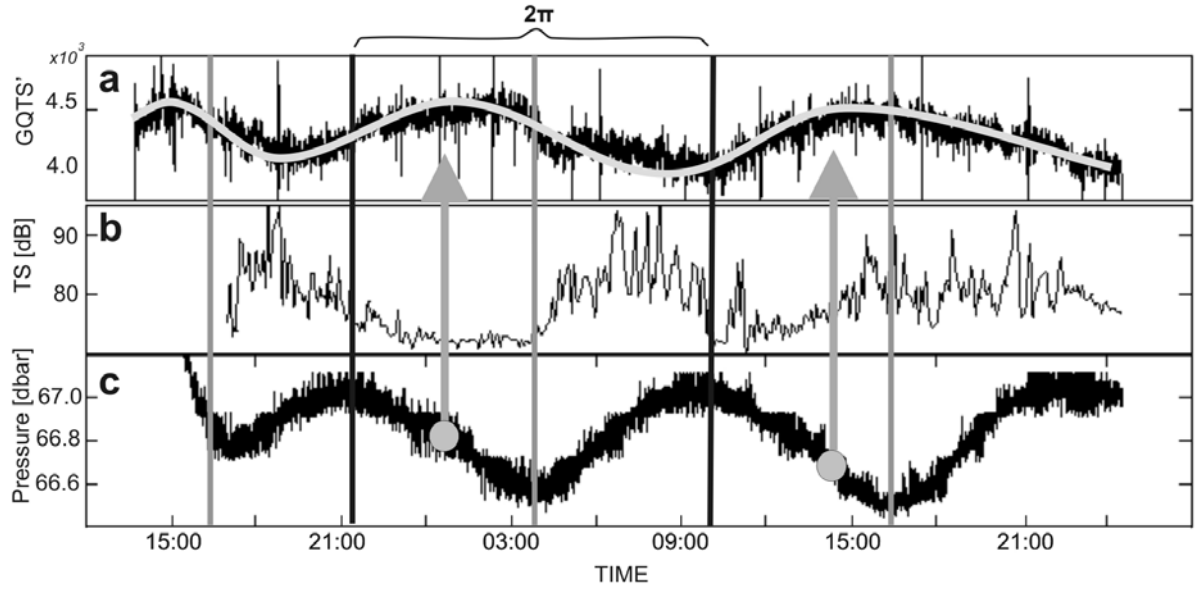

Figure 13: (a) Time series of summed backscatter values of all seeps (GQTS'), (b) target strength of the ADCP and (c) the CTD in situ pressure. Varying length of datasets is due to different initialization times of the sensors. Black vertical line indicate high water levels (2π period) separated by low water levels (grey lines). Grey arrows symbolize increased gas flux occurring at the inflection point of pressure decrease.

Discussion

Acoustic background level

In Figure 13a the bulk backscatter values are presented and temporal variations are attributed to the changing amount of free gas in the water. This is only true if other transient acoustic sources can be excluded. Due to changing currents the loads of suspended matter in the water may vary and significantly affect high frequency data by scattering. Thus, we used the backscatter data from the ADCP that was simultaneously deployed in the bubble-free environment in the vicinity of GasQuant. Due to the higher frequency of this acoustic device (1200 kHz), this system is expected to be even more sensitive to suspended particles than GasQuant. But *GQTS'* in Figure 13a was found to be counter-correlated to the ADCP target strength (TS). Therefore, the analyzed maximum intensities in the summed *ISTS* are not caused by suspended matter.

Microbubbles

Insonification of resonant microbubbles would rule out the assumed linear increase between TS and gas flux. For the given physical settings, i.e. 180 kHz transmit frequency and 70 m water depth, a resonance radius of 0.05 mm was calculated from equation 2. For such small bubbles the respective rising rate can be calculated with *Stokes law* to be 4 µm/s. For

several reasons the existence of such small microbubbles can be excluded: (1) the sinusoidal displacement pattern would evolve with much stronger amplitude; (2) very slowly rising bubbles would enter the beam gradually reaching the main lobe. This would result in gently increasing backscatter values. However, all *bubble burst*s are characterized by box-shapes with steep edges (sudden increase of *GQTS'*); (3) microbubbles around 500 micrometers radius are too small to rise through consolidated sediment or even to detach from the seafloor because their buoyancy is too small to overcome the resistance of the sediment grains.

Dynamic behavior of gas ebullition

At Tommeliten, deep seismic profiles indicate the migration of free thermogenic methane gas from the top of a salt diapir (1 km depth) towards the seafloor (HOVLAND and JUDD, 1988). Hydroacoustic investigations and coring of the upper sediment revealed both free gas bubble escape from the seafloor and methane accumulation within a clay-rich horizon (~2 mbsf) in the sediment exceeding saturation concentration (NIEMANN et al., 2005).

In this study we investigate the tempo-spatial character of gas ebullition into the water. In this respect, hitherto only a little number of shallow water gas seep investigations have been carried out and exposed a wide range of time scales to occur. Long-term variation on a day and month scale are thought to be triggered by tectonic stress, haline or thermal convection, biological pumping (TRYON et al., 1999), or seasonal temperature fluctuations of the upper seafloor (WEVER et al., 2006). In contrast the observed short term variations within minutes to hours are mainly attributed to tidal- (MARTENS and KLUMP, 1980; JACKSON et al., 1998; BOLES et al., 2001), atmospheric- (MATTSON and LIKENS, 1990), swell-induced (LEIFER and BOLES, 2005b) pressure changes, to a complicated interplay between varying fluid compositions (oil, tar and gas: LEIFER and BOLES, 2005a), or to morphological trapping of gas in pockets acting as a capacitor.

Pressure variations crucially affect both the solubility concentration of methane in seawater and the free gas volume. A pressure drop causes more dissolved CH_4 molecules to be transferred to its gaseous phase forcing bubble growth (LEIFER and BOLES, 2005b: *gas charging*). This process is strongest as the pressure drops fastest (dp/dt=min). Furthermore, at the sediment water interface (vent throat) a growing bubble must overcome the overlying hydrostatic pressure. Considering this *throat activation* model (BOLES et al., 2001), a pressure change has immediate impact on the bubble production rate. The lower the hydrostatic pressure, the easier a gas bubble will form and vice versa. In the latter case, pressure and bubble growth rate are expected to be counter-correlated. Regarding bubble

growth and release at the sediment-water interface, currents have been reported to have a significant influence, giving rise to enhanced bubble flux with rising current velocity.

Subsurface bubble growth behavior inside uncemented, soft sediment is governed by two environmental material properties. Bubble growth in (1) elastic mud is controlled by fracturing/reopening pre-existing fractures, whereas (2) sand acts fluidly or plastically in response to growth stresses (BOUDREAU et al., 2005).

Tidal

The majority of the observed seep spots emit gas almost continuously (Figure 11). We conclude that the methane supply from depth must be relatively constant during the deployment time. But the overall backscatter (*GQTS'*, Figure 13) is clearly modulated by a 12 hour tidal periodicity. *GQTS'* values increase as soon as the maximum pressure inflection point is exceeded and peak, where the pressure drop is fastest (Figure 13). The observed π/2 phase lag between maximum pressure and *GQTS'* indicates *gas charging* to be responsible for the tidal modulation by pumping dissolved methane out of the supersaturated, clay-rich horizon into the gaseous phase. Similar findings, i.e. enhanced gas ebullition triggered at decreasing pressure and peaking at dp/dt=min have previously been reported by MARTENS and KLUMP (1980) and JACKSON et al. (1998). Moreover, tidal effects dominate the water current velocity in the North Sea. High water velocity may cause smaller bubbles and higher suspended load both affecting the acoustic properties. If the gas flux from below remains constant, a shift of the bubble spectrum towards smaller radii would increase the amount of bubbles causing larger backscatter over time. But no in-phase correlation was seen and enhanced detaching caused from higher current velocities is not expected to play an important role here.

Generally, care must be taken in linking tides and gas flux. Depending on the free gas distribution within the sediment and permeability of the overlying sediment layers, the tidal load and unload on the seafloor may be propagating with a phase lag growing with depth (WANG et al., 1998; LABONTE et al., 2007). Because of high permeability and low methane concentrations of the topmost sandy layer, we do not expect such a phase delay to occur in the surficial clay layer. Though, deeper layers may be affected by tidal phase delays.

Many seeps show pulsing and periodic gas release patterns rather than continuous seepage. Release periods were found to range between 2 and 50 minutes. For short term fluctuations on a second scale swell could be responsible as noted by LEIFER et al. (2004). But the state of the sea was very moderate during the GasQuant deployment. Though, given the Nyquist

criterion, swell-induced changes could not be resolved with the used system sample frequency of 4 seconds.

Sharp peaks in spectral analysis of the seep time series (Figure 9) indicate consistency in recurring gas ebullitions. This implies that the underlying physical processes dominating the gas bubble flux remain constant. We hypothesize a more or less steady methane supply from depth and the temporal variation of gas release to be controlled by the pathway through the clay layer (Figure 14).

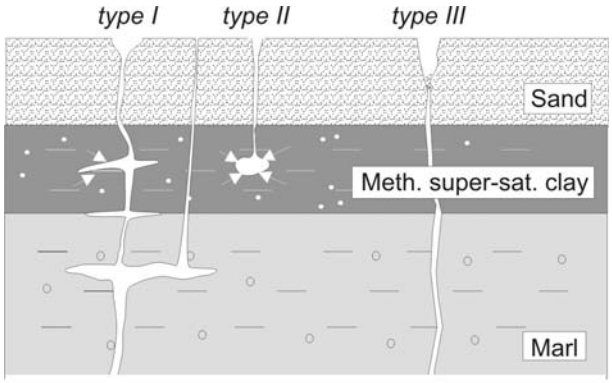

Figure 14: Schematic sketch of three different gas ebullition types at Tommeliten. Type I is fed from depth showing inter-storage in form of shallow gas pockets, type II is charged in situ from supersaturation of a methane rich layer, and type III proposes direct gas transport in a pipe without local storage and related pocket effects.

Underneath or within this layer methane may accumulate in reservoirs of different size and depth until fracture failure occurs opening pathway for bubbles to rise into the water column. The fracture remains open until equilibrium of pressure in the throat and hydrostatic pressure is restored. This fracture-dominated process and the resulting on-off character of the vent throat might be compared to single bubble growth processes causing 'linear elastic fracture mechanics' (LEFM) described by BOUDREAU et al. (2005). In contrast, a sandy reservoir responds more plastically to bubble growth giving rise to gently de- and increasing bubble growth and fluxes.

The spectral consistency again suggests constant gas supply from either below or in situ pumping within the saturated clay horizon capable of constantly refilling a reservoir. The gas seeping intensity does not change with activity time of the seep (Figure 13) and this indicates that the seeps exhibit on/off characteristics instead of a range of venting intensity. This supports the opening of fractures in an elastic/muddy environment instead of widening plastically/sandy throats changing the flux. Short periodic events could also be caused by 'sand blockage' (Figure 14, type *III*) as was experimentally verified by HOVLAND and SOMMERVILLE (1985) producing 1.5 minute periods. We recognized a 2 minutes cyclicity in the GasQuant data. We propose, that the seep surrounding funnel-shaped conduit - as described from ROV surveys - collapses in distinct intervals of a few minutes (maybe due to steepening of the walls) yielding high frequency gas escape patterns.

Spectral consistency

The length of bubble release periods is controlled by the amount of gas in a reservoir given by its size and/or internal pressure. Figure 15 shows that the longer a silent period, the longer the following bubble burst or vice versa. Moreover, the ratio between active and passive periods of the seeps is constant. This supports the idea that the size of re-opening fractures, which has an immediate impact on bubble size and gas flux, respectively, is consistent. Figure 15 depicts a linear relationship between burst length and silent periods covering a wide time range. This constant ratio between *active* and *passive* periods might be a characteristic feature of the Tommeliten seep field and the dominating media (mud/sand), but needs further data for verification.

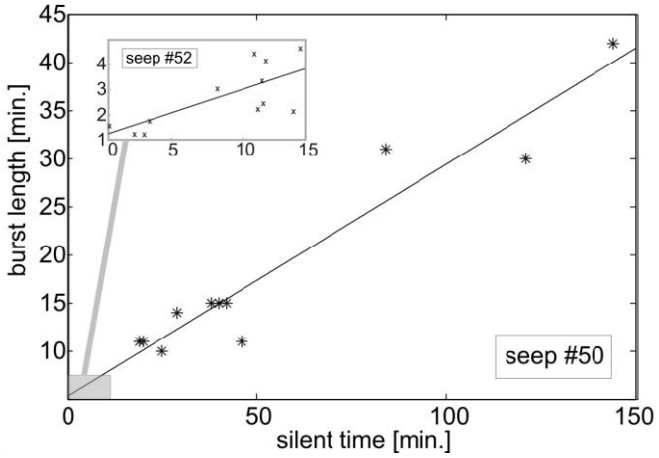

*Figure 15: The length of long-termed (#50) and short-termed (#52) bubble bursts (TA) is compared to subsequent silent intervals. Linear regression yields in both case similar slope (seep 52: y = **0.23***x + 0.82; seep 50: y= **0.24***x +5.3).*

Blowouts

No evidence for strong and continuous gas ebullition (*blowout*) was found in the data. All seep patterns clearly indicate strong horizontal bubble displacement similar to the one shown in Figure 5 and no elevated upward velocity component was found in the ADCP data. In case of a blowout event strongly enhanced bubble rise rates (up to 2 m/s: LEIFER et al., 2006) would not allow for significant horizontal shift of the bubbles before passing the swath plain. The absence of pronounced depressions (pockmarks) in bathymetry data further suggest that no vigorous blowouts have recently occurred. This is in good agreement with methane concentration and water density profiles gathered during the cruises. Even though significant bottom water methane concentrations of up to 400 nM were found in the Tommeliten area, only slightly elevated methane concentrations occur above the thermocline. In case of gentle seepage, stripping processes during the bubble rise (LEIFER and PATRO, 2002; MCGINNIS et al., 2006) lead to quick dissolution of methane in the water. Consequently, the concentrations steadily decrease towards the surface to almost background concentration of 3-4 nM as

measured by REHDER et al. (1998). The local contribution of bubble-mediated methane transport to the atmosphere is thus considered small during the well-stratified water column summer season.

Summary and Outlook

Natural methane venting in the Tommeliten area (North Sea, 56° 30' N, 3° E) was investigated with various hydroacoustic tools. Combined multi- and singlebeam surveys revealed a flat and featureless bathymetry and many gas flares clustered in two main areas showing bubble rise from the seafloor and partially reaching the sea surface (transducer depth). Within a dense seep cluster the lander-based echosounder GasQuant was deployed for 36 hours to monitor the gas release in-situ. The system covers a 2075 m² area and - compared to conventional, shipborn flare imaging techniques - yields a high tempo-spatial resolution dataset revealing individual gas seep holes and their respective transient gas escape behavior. 52 homogeneously distributed gas emanating point sources could be identified, localized and studied concerning their transient behavior. Detailed time series analysis revealed a wide-span of gas escape patterns ranging from very short termed, periodic events lasting only two minutes to longer periodic gas ebullitions up to 50 minutes. Most seepage sites in the observation area are active for more than 70 % of observation time. The individual seepage intensity shows a lognormal distribution, i.e. the weakest gas ebullitions are the most abundant ones and vice versa. The seepage clearly exhibits tidal control, showing a peak in the second quarter of the tidal pressure cycle, where pressure drops fastest. This suggests *gas charging* out of the supersaturated sediments to be the driving force with respect to the tidal modulations.

Violent seepage (blowout) did not occur during the monitoring and most likely not in the recent past, because no bathymetric depression was found in the working area. Compared to previously conducted ROV surveys, the number of seeps per m² determined by GasQuant appears 1.5-fold increased. This difference is most likely due to a sampling artefact of time-limited ROV surveys, where unsteady seepage might simply be missed. Correcting this, the visually and acoustically determined number of seeps is consistent. Thus, with respect to methane gas escape, we ascertain the Tommeliten gas seepage area to be as active as reported two decades ago by HOVLAND and JUDD (1988).

A new approach for identification and visualization of rising bubbles in the sea was established. Water current velocity data (e.g. ADCP) are used to predict the path of a rising bubble. Bubble paths may be defined and help to improve the *S/N* in the noisy acoustic data and assist to discriminate bubble from fish echoes.

GasQuant has proven to reliably detect micro-seepage gas ebullitions and offers a much larger coverage then currently available optical systems. The Lander can be deployed down to 1000 m depth and the acoustic sensing even allows for detection of hydrate coated gas bubbles that used to cause disturbing blockage in previously deployed mechanical gas bubble fluxmeter systems.

In the future, the system range and coverage will be increased significantly. Bubble detection algorithms are in preparation to analyze huge amounts of data. This will drive the device towards an online monitoring/gas bubble detection system, which could be used for monitoring of potential gas leakage in various environments.

Acknowledgements

The authors would like to thank our project partner L3-Communications ELAC Nautik for technical soft- and hardware support, system adaption and extensive and fruitful discussion with the head of the multibeam department, Peter Gimpel, and co-workers Jörg Brockhoff, Boris Schulze, and Sven Rohde. We greatly appreciate technical work and system maintenance performed by Bernhard Bannert and Matthias Türk. Data processing was additionally supported by GIS related work of assistant student Nina Köplin. Finally, we would like to thank the crew and the colleagues of RV Alkor for their assistance during both cruises. This is publication Geotech-862. The Alkor cruises were part of the COMET project in the framework of the R&D program GEOTECHNOLOGIEN, funded by the German Ministry of Education and Research (Grant No: 03G0600D).

References

Artemov, Y. G., Egorov, V. N., Polikarpov, G. G., and Gulin, S. B., 2007. Methane emission to the hydro- and atmosphere by gas bubble streams in the Dnieper paleo-delta, the Black Sea. *Reports of the Natl. Acad. of Sci. of Ukraine* 5, 110-116.

Boles, J. R., Clark, J. F., Leifer, I., and Washburn, L., 2001. Temporal variation in natural methane seep rate due to tides, Coal Oil Point area, California. *Journal of Geophysical Research* 106, 77-86.

Boudreau, B. P., Algar, C., Johnson, B. D., Croudace, I., Reed, A., Furukawa, Y., Dorgan, K. M., Jumars, P. A., Grader, A. S., and Gardiner, B. S., 2005. Bubble growth and rise in soft sediments. *Geology* 33, 517-520.

Clift, R., Grace, J. R., and Weber, M. E., 1978. *Bubbles, Drops, Particles*. Academic Press, New York.

Commander, K. W. and Moritz, E., 1989. Off-resonance contributions to acoustical bubble spectra. *J. Acoust. Soc. Am.* 85, 2665-2669.

D'Heur, M., 1984. Porosity and hydrocarbon distribution in the North Sea Chalk Reservoirs. *Marine Pet. Geol.* 1, 211-238.

Dworski, J. G. and Jackson, D. R., 1994. Spatial and temporal variation of acoustic backscatter in the STRESS experiment. *Continental Shelf Research* 14, 382-390.

Feuillade, C. and Clay, C. S., 1999. Anderson (1950) revisited. *J. Acoust. Soc. Am.* 106, 553-564.

Fofonoff, N. P. and Millard, R. C., 1983. Algorithms for computation of fundamental properties of seawater. *UNESCO Technical Papers in Marine Science* 44.

Foote, K. G., 1983. Linearity of fisheries acoustics with addition theorems. *J. Acoust. Soc. Am.* 73, 1932-1940.

Greinert, J., 2008. Monitoring temporal variability of bubble release at seeps: The hydroacoustic swath system GasQuant. *Journal of Geophysical Research* 113.

Greinert, J. and Nützel, B., 2004. Hydroacoustic experiments to establish a method for the determination of methane bubble fluxes at cold seeps. *Geo.-Marine Letters* 24, 75-85.

Hornafius, J. S., Derek, Q., and Luyendyk, B. P., 1999. The world´s most spectacular marine hydrocarbon seeps (Coal Oil Point, Santa Barbara Channel, California): Quantification of emissions. *Journal of Geophysical Research* 104, 20703-20712.

Hovland, M., 2002. On the self-sealing nature of marine seeps. *Continental Shelf Research* 22, 2387-2394.

Hovland, M., Judd, A., and Burke Jr, R. A., 1993. The Global Flux Of Methane From Shallow Submarine Sediments. *Chemosphere* 26, 559-578.

Hovland, M. and Judd, A. G., 1988. Seabed pockmarks and seepages. Graham and Trotman, London.

Hovland, M. and Sommerville, J. M., 1985. Characteristics of two natural gas seepages in the North Sea. *Marine and Petroleum Geology* 2, 319-326.

IPCC, 2007. Climate Change. Fourth Assessment Report of the IPCC. Cambridge University Press, Cambridge.

Jackson, D. R., Williams, K. L., Wever, T. F., Friedrichs, C. T., and Wright, L. D., 1998. Sonar evidence for methane ebullition in Eckernförde Bay. *Continental Shelf Research* 18, 1893-1915.

Judd, A., Davies, G., Wilson, J., Holmes, R., Baron, G., and Bryden, I., 1997. Contributions to atmospheric methane by natural seepages on the UK continental shelf. *Marine Geology* 137, 165-189.

Judd, A. G. and Hovland, M., 2007. *Seabed Fluid Flow*. Cambridge University Press, New York.

Klaucke, I., Sahling, H., Bürk, D., Weinrebe, W., and Bohrmann, G., 2005. Mapping Deep-Water Gas Emissions With Sidescan Sonar. *EOS* 86, 341-352.

L3-Communications-ELAC-Nautik-GmbH, 2003. Shallow and Medium Water Multibeam SEA BEAM 1000, technical handbook, Kiel, Germany.

LaBonte, A. L., Brown, K. M., and Tryon, M. D., 2007. Monitoring periodic and episodic flow events at Monterey Bay seeps using a new optical flow meter. *JGR* 112.

Leifer, I. and Boles, J., 2005a. Measurement of marine hydrocarbon seep flow through fractured rock and unconsolidated sediment. *Marine and Petroleum Geology* 22, 551-568.

Leifer, I. and Boles, J., 2005b. Turbine tent measurements of marine hydrocarbon seeps on subhourly timescales. *Journal of Geophysical Research* 109, 1-12.

Leifer, I. and Boles, J., 2006. Corrigendum to: Measurement of marine hydrocarbon seep flow through fractured rock and unconsolidated sediment [Marine and Petroleum Geology 22 (2005), 551–558]

Leifer, I., Boles, J. R., Luyendyk, B. P., and Clark, J. F., 2004. Transient discharges from marine hydrocarbon seeps: spatial and temporal variability. *Environmental Geology* 46, 1038-1052.

Leifer, I., Luyendyk, B. P., Boles, J., and Clark, J. F., 2006. Natural marine seepage blowout: Contribution to atmospheric methane. *Global Biogeochemical Cycles* 20, 1-9.

Leifer, I. and Patro, R. K., 2002. The bubble mechanism for methane transport from the shallow sea bed to the surface: A review and sensitivity study. *Continental Shelf Research* 22, 2409-2428.

Luyendyk, B. P., Washburn, L., Banerjee, S., Clark, J. F., and Quigley, D. C., 2003. A Methodology for Investigation of Natural Hydrocarbon Gas Seepage in the Northern Santa Barbara Channel. *OCS Study MMS 2003-054*, 1-66.

MacDonald, I. R., Guinasso jr., N. L., Sassen, R., Brooks, J. M., Lee, L., and Scott, K. T., 1994. Gas hydrate that breaches the sea floor on the continental slope of the Gulf of Mexico. *Geology* 22, 699-702.

Martens, C. S. and Klump, J. V., 1980. Biogeochemical cycling in an organic-rich coastal marine basin - I. Methane sediment-water exchange processes. *Geochim. Cosmochim. Acta* 44, 471-490.

Mattson, M. D. and Likens, G. E., 1990. Air pressure and methane fluxes. *Nature*.

McCartney, B. S. and Bary, B. M., 1965. Echo-sounding on probable gas bubbles from the bottom of Saanich Inlet, British Columbia. *Deep Sea Res.* 12, 285-294.

McGinnis, D. F., Greinert, J., Artemov, Y., Beaubien, E., and Wuest, A., 2006. Fate of rising methane bubbles in stratified waters: How much methane reaches the atmosphere? *JGR* 111, 1-15.

Medwin, H., 1977. Acoustical determinations of bubble-size spectra. *Journal of the Acoustical Society of America* 62, 1041-1044.

Merewether, R., Olsson, M. S., and Lonsdale, P., 1985. Acoustically Detected Hydrocarbon Plumes Rising From 2-km Depths in Guaymas Basin, Gulf of California. *Journal of Geophysical Research* 90, 3.075-3.085.

Minnaert, M., 1933. On musical air bubbles and the sounds of running water. *Philos. Mag.* 10, 235-248.

Niemann, H., Elvert, M., Hovland, M., Orcutt, B., Judd, A., Suck, I., Gutt, J., Joye, S., Damm, E., Finster, K., and Boetius, A., 2005. Methane emission and consumption at a North Sea gas seep (Tommeliten area). *Biogeosciences* 2, 335-351.

Ohle, W., 1960. Fernsehen, Photographie und Schallortung der Sedimentoberfläche in Seen. *Arch. Hydrobiol.* 57, 135-160.

Ostrovsky, I., McGinnis, D., Lapidus, L., and Eckert, W., 2008. Quantifying gas ebullition with echosounder: the role of methane transport by bubbles in a medium-sized lake. *Limnol. Oceanogr.: Methods* 6, 105–118.

Pfannkuche, O. and Linke, P., 2003. GEOMAR Landers as Long-Term Deep-Sea Observatories. *Sea Technology* 44, 50-55.

Rehder, G., Brewer, P. W., Peltzer, E. T., and Friederich, G., 2002. Enhanced lifetime of methane bubble streams within the deep ocean. *Geophysical Research Letters* 29, 10.1029/2001GL013966.

Rehder, G., Keir, R. S., Suess, E., and Pohlmann, T., 1998. The Multiple Sources and Patterns of Methane in North Sea Waters. *Aquatic Geochemistry* 4, 403-427.

Sauter, E. J., Muyakshin, S. I., Charlou, J.-L., Schlüter, M., Boetius, A., Jerosch, K., Damm, E., Foucher, J.-P., and Klages, M., 2006. Methane discharge from a deep-sea submarine mud volcano into the upper water column by gas hydrate-coated methane bubbles. *Earth and Planetary Science Letters* 243, 354-365.

Schneider von Deimling, J., Brockhoff, J., and Greinert, J., 2007. Flare imaging with multibeam sonar systems: Data processing for seep bubble detection. *doi:10.1029/2007GC001577 Geochem., Geophys., Geosyst. (G3, g-cubed.org)* 8, 1-7.

Tryon, M. D., Brown, K. M., and Torres, M. E., 2002. Fluid and chemical flux in and out of sediments hosting methane hydrate deposits on Hydrate Ridge, OR, II: Hydrological processes. *Earth and Planetary Science Letters* 201, 541-557.

Tryon, M. D., Brown, K. M., Torres, M. E., Tréhu, A. M., McManus, J., and Collier, R. W., 1999. Measurements of transience and downward fluid flow near episodic methane gas vents, Hydrate Ridge, Cascadia. *Geology* 27, 1.075-1.078.

Vagle, S. and Farmer, D. M., 1992. The Measurement of Bubble-Size Distributions by Acoustical Backscatter. *Journal of Atmospheric and Oceanic Technology* 9, 630-644.

Wang, K., Davis, E. E., and van der Kamp, G., 1998. Theory for the effect of free gas in subsea formations on tidal pore pressure variations and seafloor displacements. *Journal of Geophysical Research* 103, 339-353.

Wever, T. F., Lühder, R., Voß, H., and Knispel, U., 2006. Potential environmental control of free shallow gas in the seafloor of Eckernförde Bay, Germany. *Marine Geology* 225, 1-4.

Wilson, R. D., Monaghan, P. H., Osanik, A., Price, L. C., and Rogers, M. A., 1974. Natural marine oil seepage. *Science* 184, 857-865.

A multidisciplinary approach to quantify methane gas seepage at Tommeliten (North Sea)

Schneider von Deimling, J.[1]; Rehder, G.[1]; McGinnnis, D.F.[3]; Greinert, J.[2]; Linke, P.[3]

[1] Leibniz Institute for Baltic Sea Research Warnemünde (IOW), Seestrasse 15, 18119 Rostock, Germany

[2] Royal Netherlands Institute for Sea Research (NIOZ), 1790 AB, Den Burg (Texel), Netherlands

[3] Leibniz Institute of Marine Sciences (IFM-GEOMAR), Wischhofstrasse. 1-3, 24148 Kiel, Germany

Abstract

Tommeliten is a prominent methane gas releasing seep area in the Central North Sea discovered in 1978. Subsequent acoustic and ROV surveys revealed shallow gas-bearing sediments and gas bubble ebullition into the water column. The number of gas releasing single holes was roughly estimated from visual inspections in the late 80s and the respective flux extrapolated for the entire seep field (HOVLAND and JUDD, 1988). In this study, the methane gas flux of Tommeliten to the hydrosphere is re-assessed and - under consideration of the hydrographic setting - the potential methane transport to the atmosphere is discussed. We compiled earlier and new data including video observations, various acoustic evidences of gas bubbles, and their geochemical trace in the water column. Parametric subbottom sonar data reveal the three-dimensional distribution of shallow gas-bearing sediments and morphologic features relevant for gas migration. Five methane gas ebullition areas with an overall area 20 times larger than estimated in previous studies were identified. Submersible and ROV campaigns revealed an average gas bubble flux of around 12 ml/min per seep hole. By the use of an extensive dataset comprising video, flare imaging and hydroacoustic data a total gas bubble-mediated methane flux of ~0.8- ~4.8*10^6 moles per year was constrained.

Several CTD casts in the vicinity of the gas seeps were conducted to trace the methane footprint from rising gas bubbles, showing dissolved methane concentrations up to 268nM close to the seafloor. A negative carbon-isotopic shift suggests an additional methane source within the thermocline of unknown strength. To test how much of the bubble-mediated methane enters the upper mixed layer and potentially is transferred to the atmosphere through sea-air fluxes, a numerical bubble dissolution model is employed. Interpretation of the methane distribution in the water column and model results indicate that less than ~4 % of the gas initially released at the seafloor will be transported via bubbles into the mixed layer and ultimately to the atmosphere. However, in consideration of the seasonal hydrographic changes in the North Sea, even quantitative evasion of seepage methane into the atmosphere is expected, dominantly in fall/winter.

Introduction

Methane is the most abundant hydrocarbon in the atmosphere and has increased by ~30 % during the past 25 years to a global mean average of 1.774 ppm in 2005. The 25fold larger global warming potential (on a 100 yr. timescale) compared to CO_2 makes methane the second most important greenhouse gas and recent studies have estimated a 18 % contribution of methane to the total anthropogenic radiative forcing (IPCC, 2007). The atmospheric methane growth rate per year has decreased from 1 % in the early 80s (BLAKE and ROWLAND, 1988) to close to zero towards the turn of the millennium, the reasons for this being under debate (Prather, 2001). Following this period of little change in global atmospheric methane mole fraction, RIGBY et al. (2008) present measurements that show renewed growth starting near the beginning of 2007.

The marine methane contribution from the seafloor to the global annual source strength to the atmosphere of 540 Tg yr^{-1} is currently estimated to 20 Tg yr^{-1} (KVENVOLDEN et al., 2002) and arises primarily from seeps occurring world-wide on the continental shelves, in estuaries and river deltas. The main sources of the seepage are either thermogenic methane from deeper strata, or surficially generated biogenic methane, which migrates dissolved (fluid flow) and/or in the form of rising gas bubbles through the sediment towards the seafloor/water interface. In anoxic environments, that often prevail a few centimeters below the sediment the dissolved methane is oxidized by consortia of sulfate reducing bacteria and methane oxidizing archae (BOETIUS et al., 2000). This microbial filter effectively converts approximately 80 % of the dissolved methane to CO_2 representing the most effective sink for seepage methane (HINRICHS and BOETIUS, 2002). In contrast, methane gas bubbles migrating through the sediments bypass such a microbial filter. Once the gas has reached the sediment-water interface, gas bubbles detach from the sediment, rise through the water column and will partially dissolve. By this vertical transport mechanism a fraction might enter the upper mixed layer and is eventually transferred to the atmosphere by air-sea exchange (SCHMALE, 2006; REHDER and SUESS, 2001).

Although gas seepage is a widespread phenomenon, only a few gas venting sites with diverse environmental settings have been intensively studied so far. E.g. TORRES et al. (2002) and HEESCHEN et al. (2005) studied gas ventings associated with massive methane hydrate deposits at Cascadia Margin; MACDONALD et al. (1989) found salt tectonically driven oily gas seepages in the Gulf of Mexico and JUDD and HOVLAND (2007) give a compilation about several study sites including shallow seepages in the North Sea, that often appear together with pockmark structures. Even in water depths beyond 1000 m gas bubble ebullition has been observed, e.g. from mud volcanoes in the Black Sea (SAHLING et al., in

press; Vodyanitskii, 2070 m), in the Guayama Basin (MEREWETHER et al., 1985), or in the Norwegian Sea (SAUTER et al., 2006; Hakon Mosby 1250 m).

Only four quantitative gas seep flux measurements were published so far, revealing minor (8.5 ml/min: LEIFER and MACDONALD, 2003; 12.5 ml/min: this study; 32-120 ml/min: SAHLING et al., in press), intermediate (1.6 l/min: SAUTER et al., 2006; 5 l/min: TORRES et al., 2002) and major (420-900 l/min: LEIFER and BOLES, 2005b) gas ebullition rates.

Most of these sites were detected during hydroacoustic surveys, which showed evidence of gas bubble occurrence and allowed an estimate of their rising heights in the water column (MEREWETHER et al., 1985; HORNAFIUS et al., 1999).

So far scientific work either concentrated on such acoustic detections or on geochemical and/or optical approaches for seep characterization and corresponding methane flux estimates. In this study acoustic evidence and geochemical tracing of rising gas bubbles in the water column are considered as well as the oceanographic control on the methane distribution. Based on new data sets and techniques, we reassess the gas flux from the Tommeliten field and reconsider the fate of the gas in the water column, the latter with implication for all seafloor methane sources in the central North Sea.

Methodology

Within the framework of the GEOTECHNOLOGIEN project COMET data was acquired during two cruises with *R/V Alkor* to the North Sea in June 2005 and October 2006. The first expedition (*ALK 259*) allowed detailed hydroacoustic surveying and geochemical sampling of the water column. The succeeding cruise *ALK 290* was abandoned due to a forthcoming storm limiting our station work to a two hours submersible dive (*JAGO*) at Tommeliten with short gas seep inspection and flux analysis. To mitigate this limitation, further ROV (*Cherokee*) observations and subbottom data gathered during cruise of *R/V Heincke 180* and *Alk 267* are included in this study by courtesy of Antje Boetius (chief scientist, MPI, Bremen).

Integrated scientific approach

One major task in this study is to re-assess the total gas ebullition of Tommeliten. In contrast to more localized seep sites, where a single gas bubble flux measurement virtually presents the source strength of the seep site, Tommeliten requires field mapping to account for the widespread occurrence of a large number of seep holes, that all contribute to the total

methane flux. To obtain maximum tempo-spatial coverage of seep areas and abundance of gas vents, hydroacoustic water column data (flare imaging) from three cruises were compiled.

However, water column reflections present time-limited acoustic snapshots and transient ventings might be missed during surveying. In contrast, shallow gas stored in the sediment displays a less time-variant inventory. Therefore subbottom data were included to identify shallow gas-bearing sediments as potential seepage areas.

To give a good estimate for both, in situ gas ebullition and respective atmospheric input, the respective gas vents had to be characterized with respect to their flux, bubble sizes and respective rising heights and temporal activity. Video analysis, gas sampling, gas bubble modeling and hydroacoustic in situ monitoring data are used to constrain a comprehensive view of the ebullition character. The pathways of bubble-mediated methane in the water column are then pursued by vertical geochemical and physical CTD water sampling. Taking into account the distinct seasonal change of oceanographic settings throughout the year finally permits an overall perspective about the fate of seepage-derived methane in the North Sea.

Flare Imaging

The term ‘Flare’ is used in the scientific community to describe the echogram expressions of rising gas bubbles in water, that were repeatedly found on analogue and digital echoprints since 1960 (OHLE, 1960). Prominent acoustic scattering of gas bubbles in water emerges if the resonance frequency of gas bubbles is stimulated by the used sonar frequency (MEDWIN, 1977). Moreover, bubbles with similar or larger size than the acoustic wavelength show significant backscattering in the off-resonance *geometric* domain (Appendix B, COMMANDER and MORITZ, 1989) mainly due to the huge difference in impedance between gas and water. Several studies have attributed modern sonar a high sensitivity for the detection of seep bubbles released from various depths (Merewether et al., 1985: 2000 m; HORNAFIUS et al., 1999: 100 m; GREINERT et al., 2006: 2000 m; ARTEMOV et al., 2007: 100-2000m). Even for the minor gas seepages of Tommeliten flares were repeatedly reported (NIEMANN et al., 2005; WEGENER, 2008; SCHNEIDER VON DEIMLING et al., submitted).

However, the inversion of flare echoes into gas bubble flux is a difficult field and was thoroughly studied in ARTEMOV et al. (2007) for bubble plumes, and examined for single rising bubbles in a Lake by OSTROVSKY (2003). Even though our used split-beam sounder was suitable for such a quantitative approach, the seepage character of Tommeliten prohibits acoustic gas volume measurements by means of ship-born single beam. The reason for this

is the high seep density and shallow depth causing several single bubbles to be insonified at once within a single beam pulse shell. This obfuscates unique phase separation of the received echoes and prohibits angular deflection/target-strength-correction. Further consequences are uncontrolled loss of any sonar target, which implies that bubble dissolution and migration out of the acoustic beam cannot be differentiated. Under these circumstances our interpretation of flares concentrates on detection, abundance mapping (similar like in JUDD et al., 1997) and relative changes of backscattering volume within a given grid cell.

It is generally accepted that there is a certain dependency between the echo-signal strength of a flare and underlying gas flux, especially if the bubble size population do not change with flux variations and if resonance effects occur (Appendix B). At least close to the seafloor the expected seep bubble size exceeds 2 mm size (shown later) and is thus far out of the resonance domain with regard to the used sonar frequency (38 kHz) and water depth (72 m). Consequently, relative changes in echo intensity can be used to localize maximum seepage within a seep field.

A major difficulty in flare imaging is the potential confusion between rising methane seep bubbles with fish due to the acoustic similarity between swim bladders and gas bubbles. An additional aggravating factor derives from the observed attraction of fish to seep sites (unpublished observations gathered during several cruises and seep sites surveys) for hitherto unknown reason. If fish concentrate into schools then their acoustic signature resembles that of a bubble plume. However, fish schools rather extend horizontally (JUDD et al., 1997) with irregular intensity distribution, whereas bubble plumes spread vertically with maximum intensity in the middle of the flare or show bubble rising patterns as presented later.

Other prominent scatterers caused from horizontal plankton or density layering can clearly be distinguished from flares by their lateral wide spread and stationary appearance.

A strong protocol to distinguish gas bubbles from unwanted echoes is given later to unambiguously identify the spatial extent of gas escape at Tommeliten.

Subbottom profiling

Subbottom profiling is a very effective method to map free gas occurrences below the sea floor. Trapped gas bubbles changes the bulk acoustic properties of sediments dramatically, because of their low density and high compressibility in comparison to the pore fluid properties. The acoustic behavior of gas charged sediments is very complicated and still

under debate. A basic theory to model the acoustic properties like sound velocity and attenuation was developed by ANDERSON and HAMPTON (1980a, 1980b). A model to predict the acoustic scattering response of gas charged mud sediments was published by LYONS et al. (1996).

The acoustic images of gassy deposits are different depending on the geological settings and the frequency range of the acoustic waves. A high reflectivity of the surface layer and an abrupt blanking of the subbottom layers is observed in soft basin sediments. This phenomenon was already discovered by HINZ et al. (1971) in the western Baltic and named as "Beckeneffekt". The indications of free gas in sandy deposits are not that obvious. The penetration of the acoustic signals in sand is much less then in mud or clay deposits.

At Tommeliten HOVLAND and SOMMERVILLE (1985) presented an up-dipping reflector in shallow pinger data and maximum seepage at its crest; NIEMANN et al. (2005) concluded a dome structure to cause preferential gas pathway and seepage here. In this study additional survey lines were consulted for mapping of this 3D feature and to reveal other potential shallow gas occurrences and migration pathways.

Gas chemistry and bubble modeling

If a methane gas bubble leaves the seafloor it comes into contacts with seawater of low (relative) CH_4 concentration. The large methane concentration gradient between the bubble's interior (partial pressure * solubility coefficient) and the undersaturated seawater is the driving force for bubble dissolution yielding bubble → seawater methane flux. As long as the gradient persists during its ascent, methane is continuously dissolved into seawater. On the contrary dissolved gases such as oxygen, nitrogen, and argon are stripped, and enter the rising bubble driven by the reversed process (seawater → bubble flux). The expected geochemical trace remaining in the surrounding water of the rising gas bubbles is monitored by discrete methane water sampling through vertical CTD/rosette casts.

The composition of a rising gas bubble, its size, rise velocity and methane input into the surrounding water is very dynamic with depth and highly dependent on parameters such as initial bubble size, bubble gas composition, and environmental parameters such as temperature, salinity, and gas concentration of the surrounding water. To better interpret the measured methane profiles of water samples in terms of bubble-mediated transport, a bubble dissolution model is consulted (MCGINNIS et al., 2006). The amount of methane loss at respective depth and total rising heights for bubbles released with various sizes can then be numerically modeled.

The further fate of a dissolved methane plume requires knowledge of the oceanographic setting. CTD casts revealed salinity and temperature records to define the depth of a pycnocline separating the upper well-mixed layer from deeper water masses. The depth and intensity of the pycnocline is a controlling parameter for mixing and the potential evasion of seepage methane to the atmosphere.

The $\delta^{13}C\text{-}CH_4$ isotope ratio of extracted gas from several water samples was determined mainly to distinguish different methane sources and sinks in the water column, as well as to distinguish between consumption and mixing (i.e. dilution processes). In situ biogenic methane production usually produces isotopically light methane, while oxidation preferentially uses $^{12}CH_4$, leaving the remaining methane pool isotopically enriched in ^{13}C (WHITECAR, 1999). Mixing, at the other hand, naturally does not change the total isotopic composition of the methane inventory.

Methods

Sonar

Flare Imaging

Simrad EK60 (38 kHz, split beam) data were recorded in 2005 and 2006 on R/V Alkor. Briefly, the sonar transmitted a 1.024 ms CW-pulse (2kW) at survey speeds between 3-8 knots and ping rate less than 0.5 seconds. Based on the beam angle α=6.5° and the additional angular tilt caused by uncompensated ship motion, the positioning accuracy of the data at the given depth is not better than ±70 m into any direction depending on the state of the sea. Anyhow, given a ping rate higher than the roll motion period of the vessel leads to extra sonar coverage and thus, superior probability of target detection in the water column. Further system settings can be found in SCHNEIDER VON DEIMLING et al. (submitted)

The sonar data was later analyzed with postprocessing software MYRIAX ECHOVIEW. After adjusting the gain appropriately, flares could be visualized in echograms to determine maximum detection height, abundance per area and volume scattering strength, where for the latter only selected survey lines were used to exclude data showing significant acoustic interference with an unknown source. The volume scattering strength *Sv,* was determined using a horizontal integration window of 50 m across the main seeping field and only 15 meters vertically, beginning 3 m above the seafloor. This approach prohibits the integration of echoes from bubbles, that have significantly suffered volume loss during their rise and thus mitigates potential resonator effects. Furthermore the closeness of the integration area

to the sea floor and bubble sources guarantees not to include bubbles displaced through currents from adjacent seep sites.

A quantitative mapping of gas venting areas requires a strong protocol for unambiguous gas bubble recognition. This was assured by the application of the following: (1) the vertical/horizontal dimension ratio of echo pattern must be larger than 2 to account for preferential horizontal dispersion of fish schools, (2) flare must show contact with the seafloor, that is always considered the origin of gas ebullitions, (3) target strength variation within the plume, that is most likely the case due to natural dispersion of rising gas bubbles, (4) detection of rising reflectors with indicative bubble ascent velocities between 15-30 cm/s have additionally been counted valid, even if they do not comply with the listed requirements 1 and 3, (5) isolated flare findings (outside of flare cluster) are only accepted in case of replicate detection at least twice (fish is unlikely to rest at the same location over time).

Subbottom profiling

The echosounder prototype *SES-2000* manufactured by Rostock University/*INNOMAR* was intensely used during *HEI 180* mainly for subbottom profiling. This type of echo sounder uses the parametric effect. Two similar so called primary frequencies f1 and f2 are simultaneously transmitted to generate an additional, parametric frequency of f2-f1 (nonlinear effect, difference frequency). The resulting parametric sound holds the narrow beam/short pulse characteristics of the primary frequency improving resolution. At the same time the low frequency component has a lower attenuation giving rise to enhanced penetration. Additionally reduced side-lobes in the difference frequency beam pattern enhance the S/N ratio.

The SES-2000 transmits 100 and 88-96 kHz as primary frequencies to induce the parametric frequency of 4-12 kHz with a narrow half-power beam-width of ±1.8 degrees. Electronic beam steering guarantees constant and perpendicular incidence angle even if the vessel is heavily rolling or pitching. The ship movement including the heave was recorded with a motion sensor. So far no software was implemented to correct the data for the heave, which causes significant artefacts in later presentations. In combination with a high precision GPS (*DEBEG* 4412 MX) and motion-compensated narrow beam steering an exact georeferencing of each ping was achieved. Frequency classification was not feasible because the prototype sonar only recorded enveloped data at this stage of development.

CTD, water sampling and video analysis

A Seabird 911 CTD additionally equipped with a Beckmann oxygen sensor and 12 x 10 l Niskin rosette water sampler was used for water column investigations during *ALK 259*. A total of 17 CTD stations was conducted around Tommeliten with downcast speed of 0.5 m/s. At most of these casts, water samples were gathered for methane concentration and later shorebased stable carbon isotope analysis.

For CH_4 concentration analysis aboard, a modification of the vacuum degassing method described by LAMMERS and SUESS (1994) was used (REHDER et al., 1999). Within two hours after the casts 1400 ml seawater from Niskin was drawn under the control of a calibrated ENGOLIT Flow-Control 100S DMK flow controller into evacuated 2200 ml glass bottles, which were closed with valve caps to avoid any air contamination caused by leakage. After one minute of heavy shaking, dissolved gases are assumed to be equilibrated, leading to almost quantitative transfer into the gas phase (KEIR et al., 2005). Subsequently, the gas phase was recompressed to atmospheric pressure, a 1ml subsample was injected into a gas chromatograph equipped with an FID for methane analysis (±5% accuracy), and the remaining gas was stored for shore-based stable carbon isotope analysis (±1‰ VPDB accuracy). For this, sub-samples of the extracted gas were filled into pre-evacuated 20 ml crim cap glass vials added with 2 ml of supersaturated salt solution, sealed with a butyl rubber septum and stored protected from light and upside-down to suppress biological activity and atmospheric contamination with air. Later isotopic analyses ($\delta^{13}C\text{-}CH_4$) of these sub-samples were conducted at IFM-GEOMAR laboratory (GC-IRMS; Finigan MAT 253, s. SCHMALE, 2006).

The submersible JAGO was deployed once and rested at four seep sites to film gas ebullition without landing the vessel to exclude artefacts caused from the load of the vessel on the sensible fluid-flow-gas system at the seafloor. Cherokee observation at one seep site was performed after the vessel had landed. Later image processing for better bubble visualization (*ImageJ)* and slow-motion video analysis allowed a characterization of seepage. The employed camera systems were not prepared for optical corrections necessary for a micrometer accuracy measurement (LEIFER et al., 2001). However, selected frame grabs showing bubbles rising close to a reference size (e.g. funnel) allow valuable estimates of bubble sizes, ebullition rates, shape oscillations of the bubbles (wobbling), trace oscillations (zig-zag trajectory), and succession distance between individual bubbles. At one of the gas vents JAGO measured the gas flux by capturing gas bubbles into a metal housing with known volume. Later vessel retrieval during heavy sea caused accidental valve opening and prohibited any further analysis of the sampled gas.

Bubble gas exchange modeling

A numerical bubble propagation model described by MCGINNIS et al. (2006) was used to evaluate the bubble-mediated methane input to the water column at various depths. The model was especially developed for methane gas bubble analysis, and includes parameterizations for the mass transfer coefficients *K* and bubble rise velocities v_b, and diffusivities and solubilities of the gases. To account for dependencies of those parameters on water temperature, salinity and dissolved gas concentrations the model is fed with the respective environmental CTD data. Then the model solves the following equation for each gas identity *i* by numerical integration using the Euler method.

$$\frac{dM_i}{dz} = -K_{Li}\left(H_i P_i - C_i\right)\frac{4\pi r^2}{v_b},$$

were *M* denotes the mass of specific gas *i*, *z* the water depth, K_L the liquid-side mass transfer coefficient, *H* Henry's constant [mol/(m^3 bar)], *P* the pressure [bar] at depth *z*, and *C* the aqueous-phase concentration of gas *i* [mol/m^3]. For parameterizations and further model descriptions we refer to the literature (model: MCGINNIS et al., 2006; gas solubility: RETTICH et al., 1981; bubble rise velocity: CLIFT et al., 1978; diffusivity: HAYDUK and LAUDIE, 1974; seep bubble adaptations LEIFER and PATRO, 2002).

Model runs were performed using a vertical step size of 1 cm based on the CTD data of station CTD-16 (temperature, oxygen, salinity and dissolved methane concentration) and run for seven bubbles with initial CH_4 fraction of 100 %, and initial sizes between 3 mm to 12 mm diameter released at 72 m depth. Considered output parameters are bubble size, depth-specific methane dissolution rate, and gas composition at specific depths.

Study area

Tommeliten – geology and seepage

Tommeliten is located in the Central North Sea at 56° 30' N and 3° *E* and belongs to the Greater Ekofisk area overlying the three salt diapir structures Alpha, Gamma and Delta. The Delta structure has domed and pierced the enclosing sediments and lacks a proper seal. Abundant seismic evidence exists for seepage from the seabed at a water depth of 70 m associated with this Delta structure, where corresponding faulting and fracturing enhance vertical migration of fluids and/or gas (SCHUMACHER and ABRAMS, 1994). Shallow seismic pinger profiles indicated that acoustic turbidity (gas blanking) was present in the surficial sediments over an area of approximately 120.000 m² (HOVLAND and SOMMERVILLE, 1985).

Table 1: Compilation of relevant data concerning this study (subdivided into findings from early 80ies, METROL, and COMET cruises)

Reference (R/V cruise)	Data & Method	Findings	Results
Hovland 1985	Video/ROV	Seep density	sd=120/6500m²
Hovland 1988	Acoustics	Area of venting, number of vents	A_{vent}=6500m² ; n_A=120
	Gas Sampling	Area of shallow gas	A_{sg}=120.000m²
	General description*	CH_4 Flux	f_A=24 m³/day@70m
		Bubble release frequency	rf=0.1667Hz
		Bubble diameter, gentle seeping	d=10mm
		Isotopic signature	δ13C-CH_4=-45.6‰ PDB
		Gas bubble composition	c=99 %CH_4
Hovland 1993		CH_4 Flux one seep hole	f_i=5.6e6g/yr
		CH_4 Flux over A=6500	f_A=47 g CH_4/(m²yr)
Judd 2004	Recalculation of flux	CH_4 Flux over A=6500	f_A=6400 gCH_4/(m²yr)
Judd 2007		CH_4 Flux of Tommeliten	f_A=41.6 t/yr, 24m³/day at am
Niemann 2005	ROV Sprint 102*, Cherokee	Microbiol. AOM, CH_4 profiles	
(*HEI 169/180*)	Coring	Diffusive methane flux to hydr.	f_d=0 mol/(m²s)
	Hydroacoustics	Area of venting	A=3500m²
	Microbiology*	1 dome structure	
Wegener 2008	Pore water geochemistry*	Gas seep characterization	
(*ALK 267, Hei 169/180*)	Seafloor description	2 Flare Clusters	
		Gentle seeping	
Schneider v.D., submitted	Multibeam mapping	Flat bathymetry	
this study	Flare Imaging*	5 flare clusters	s. Fig. 2
		Area of venting	A=140.000 m²
		Total number of seeps	n_A ~ 550
		Total bubble-mediated CH_4 flux	f_{Tomm} ~0.6-3.8 10^6 mol/year
		CH4 Flux over A=6500	f_A=1480-9377 g CH_4/(m²yr)
ALK 290	GasQuant*	Seep density	sd_{GQ}=52/2075m²
		Bulk activity time factor	t=0.7 (1 = 100%)
ALK 290	Submersible JAGO	CH4 Flux one seep hole	f_i=12.5 [ml/min.]
		Seafloor description	gentle seeping'
ALK 259	CTD*	Vertical water column profile	T, S, DO, CH_4, $\delta^{13}CH_4$
HEI 180	Subbottom profiling	3D structures, shallow gas	s. Fig. 8
		Bubble diameter [min; max]	d=[4; 6] mm
*main focus; important result for this study			

Detailed survey over this area in 1983 (HOVLAND and JUDD, 1988) revealed free gas ebullition locally entering the 72 m overlying water column. Remote acoustic and in situ visual observations on echosounder and video records, respectively, witness local gas ebullition within the gas-charged area. Most of them were concentrated in a 6500 m² area. At this so-called 'main seepage' location, 22 seep holes were detected visually, and a total of 120 seep holes releasing 10 mm diameter bubbles every 6 seconds (HOVLAND and SOMMERVILLE, 1985) was estimated. From these data, a flux of 24 m³ per day at ambient pressure was derived (JUDD and HOVLAND, 2007). However we cannot confirm this frequently cited number from a simple re-calculation due to the expected in situ volume release of 120 seep holes releasing one 10 mm bubble every 6 seconds resulting in 0.9 m³ a day (120 seep sites x 86400 seconds per day x 1/6 seconds x bubble volume). In JUDD (2004) a re-calculated number is presented, but no indication is given how the calculation was performed. Moreover, those extrapolations were a first guess based on a few visual findings, no systematic and covering vent mapping was conducted, and the ability of sonar performance to show evidence of free gas in the water column was restricted.

NIEMANN et al. (2005) reported flares even reaching the transducer depth, but asses the respective gas ebullition area to only 3500 m². The authors report an additional seep site at 56° 29.56 N 2° 59.25 E. Flare occurrences were confirmed in WEGENER (2008) and more detailed flare imaging conducted by SCHNEIDER VON DEIMLING et al. (submitted) indicate even larger areas of venting around the previously reported hot spots.

Multibeam surveys show a flat bathymetry, and lander-based acoustic monitoring data constrain the density distribution and periodicity of the vent sites (SCHNEIDER VON DEIMLING et al., submitted). 52 vent holes were documented in an area of 2075m², and an average temporal activity of 70 % was observed during the total survey time of 36 hours (SCHNEIDER VON DEIMLING et al., submitted).

Video survey revealed that funnel-shaped craters, approximately 10 cm deep and with a 20 cm diameter had formed around each seep hole, typically ~1cm wide, in the sandy seafloor from all video data (Table 1). The spacing between individual vents increases exponentially with increasing distance away from the centre of activity (HOVLAND and SOMMERVILLE, 1985). Seep holes were found exclusively over sandy seafloor and geochemical analysis of those bubbles revealed 99 % methane, the rest being ethane, propane, and butane; the $\delta^{13}C$ value is -45.6 ‰ VPDB, and the gas is likely to be of thermogenic origin (Hovland and Sommerville, 1985). Next to the bubble sites, maximum water column methane concentrations were measured up to 500 nM, and background concentration off the seep sites showing ~5 nM (NIEMANN et al., 2005).

Single subbottom echosounder profiles presented in HOVLAND and SOMMERVILLE (1985) and NIEMANN et al. (2005) indicate dome-like structures in the seep area with a distinct sequence of layers narrowing towards the apex of the dome, where the gas plumes are situated. Based on these 2D-findings and three vibro-corer stations, NIEMANN et al. (2005) propose the following conceptual model: an impermeable horizon of stiff marls acts as natural gas barrier for methane rising from a deep gas reservoir, lifting the upper layers and forming the dome. Preferentially at the apex of the dome, the underlying marl may crack, giving way for methane to migrate in the overlain clay-silt horizon. This layer was locally found to hold methane gas bubbles between 0.1-10 mm diameter and oversaturated methane pore water concentrations.

Hydrographic seasonal cycle

A significant temperature-induced seasonality is present in the central and northern offshore areas of the North Sea, causing a distinct thermocline during spring and summer. As a result, vertical transport across this interface is temporarily suppressed.

POHLMANN (1996) concentrates on the determination of the eddy viscosity *Av*, which is highly related to vertical mixing and thus describes the tempo-spatial behavior of stratification and vertical mixing in the North Sea throughout the year. Seasonal heating and cooling at the sea surface as well as mixing induced by winds and bottom-friction control this annual cycle (Figure 1).

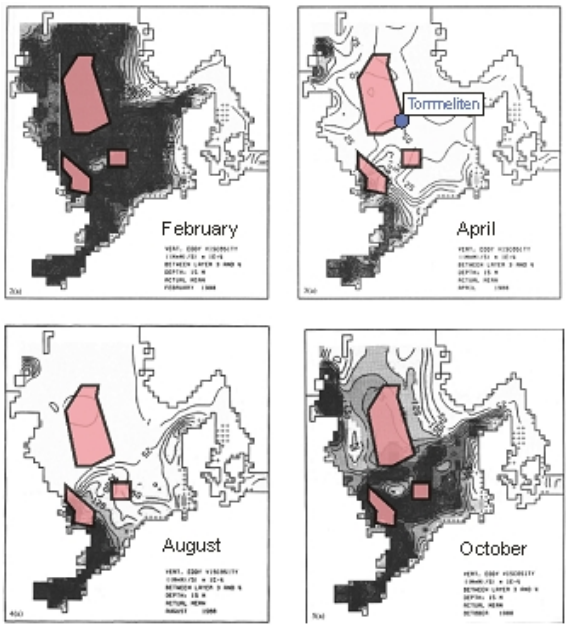

Figure 1: Seasonal change of stratification, expressed as monthly-averaged vertical eddy viscosity A_v between 15 and 20 meters grid cell/water depth (POHLMANN, 1996). Darker color-coding indicates larger A_v and vertical mixing. Gas seepage areas are shown by purple polygons and were compiled from various sources (Norwegian EEZ: JUDD and HOVLAND, 2007; English EEZ: JUDD et al., 1997, JUDD, 2001; Dutch EEZ: SCHROOT et al., 2005).

For the offshore Central and Northern North Sea, a generic sequence annually recurs: in April, the warming has already started, which in connection with decreasing storm activity explains the strong decrease of *Av*. A thermocline evolves over large areas (Figure 1, white areas). The depth and the gradient of the thermocline increase towards the summer, gradually suppressing turbulent vertical exchange between the deep and the surface water. The advent of subsurface cooling in October causes an increase of eddy viscosity. Intensification of storm activity further contributes to this trend. In February, the water column is virtually homogeneous and maximum vertical mixing is established.

Results

Figure 2 compiles areas and spots that have been reported active gas venting localities from previous (HOVLAND and JUDD, 1988: blue; NIEMANN et al., 2005: red) and recent (SCHNEIDER VON DEIMLING et al., submitted) studies, whereas the latter indicates the largest areas of active gas venting and will be discussed in the following in the context of video, acoustic water column/subbottom imaging and geochemical data.

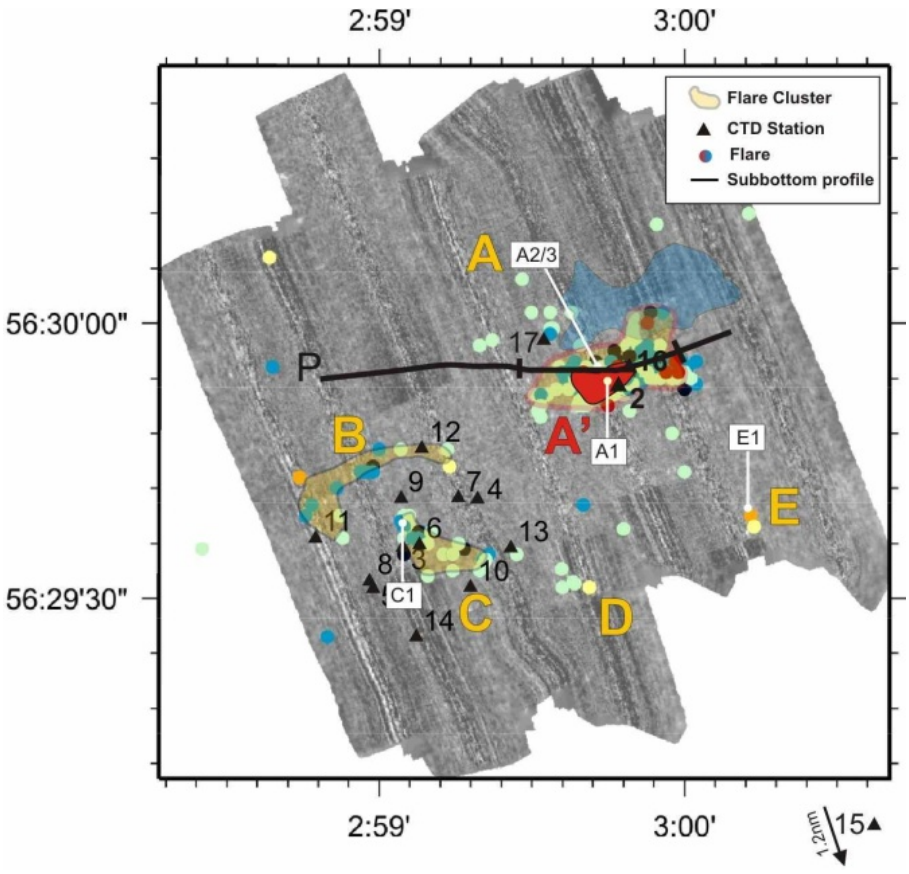

Figure 2: Map showing multibeam backscatter data as grey-shaded background image with height-colored dots for each flare finding from SCHNEIDER VON DEIMLING et al. (submitted). Formerly reported gas-charged upper sediment area (HOVLAND and SOMMERVILLE, 1985) and free gas bubble ebullitions (NIEMANN et al., 2005) additionally plot as blue and red area (A'). Yellow polygons and upper case letters A-E mark boundaries of new flare clusters derived from this study. Individual flares referred to in the text (Figure 4) are referenced here with A1-A3, C1, and E1. CTD casts are coded as black triangles. A selected subbottom track P crossing A plots as black line.

Video observations

In the centre of area *A* (Figure 2), two dives confirmed previous findings of bacterial mats (~30 cm diameter), bioherms and gas bubble ebullitions (Figure 3). We found maximum abundance of gas venting in the center of area *A'* in accordance to previous mapping reported by NIEMANN et al. (2005). All gas bubble vents are characterized by 'gentle' gas ebullition in the form of single bubble streams, i.e. either one bubble after the other detaches from the sediment/water interface in equidistant/periodic succession (Figure 3a-c), or small bursts of a few bubbles develop immediately after the release from the hole and propagate as a group (Figure 3d).

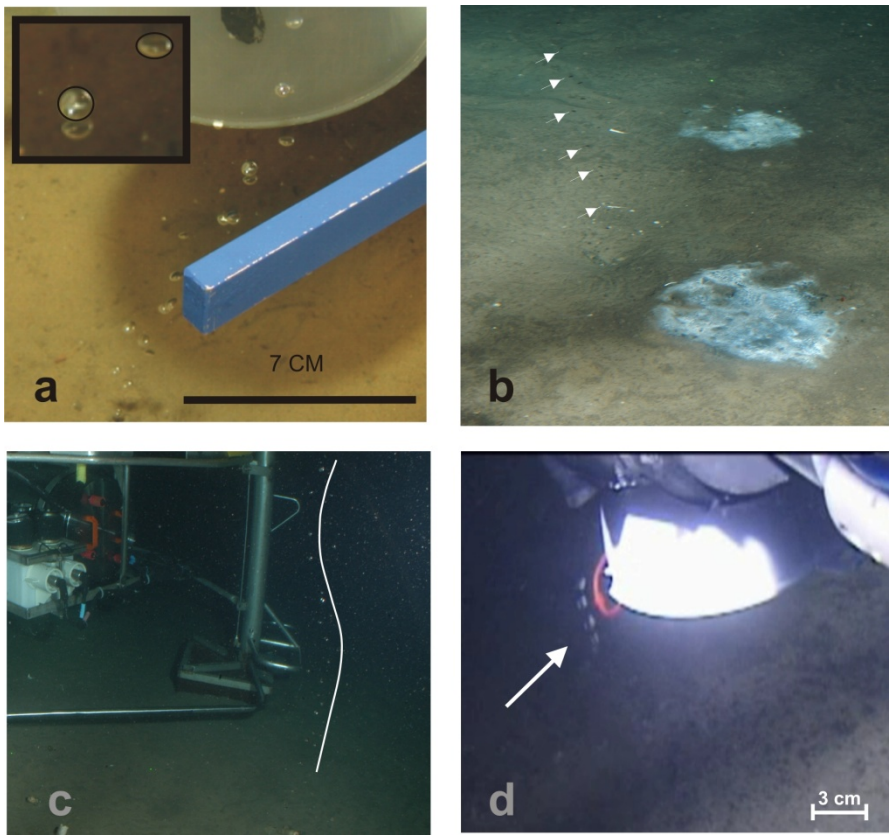

Figure 3: ***a*** *Bubble capturing during station work using ROV Cherokee (ALK267) showing shape oscillations (inlet), [Image source: DFG/BMBF project MUMM, RV ALKOR 267, chief scientist Antje Boetius]* ***b*** *bubble chain indicated by white arrows filmed with JAGO (ALK 290) next to bacterial mats* ***c*** *bubble chain with trace oscillations (wavy white line) in the vicinity of the deployed GasQuant Lander (ALK 290)* ***d*** *bubble flux measurement showing a small bubble burst of four bubbles close to a 12 cm funnel hold by the manipulator arm of JAGO.*

Gas ebullitions at four sites were particularly inspected by JAGO, showing only little frequency variation in the range between 6-10 Hz, with an average value of 7.2 bubbles per second. In contrast, analysis of the Cherokee video reveals much higher ebullition frequency

of 17 bubbles per second that might be caused from the vessels load. The found ebullition rates thus clearly exceed the previously reported 6 seconds interval (HOVLAND and JUDD, 1988) by magnitudes. Optical bubble size measurements from close up photographs reveal spherical to spheroidal bubble shape with aspect ratios between 1 and 1.4 (Figure 3a, inlet), with an average of 1.2 Bubble shape oscillations (Figure 3a, inlet) were accompanied by trace oscillations (3c) with a centimeter amplitude and decimeter wavelength range. The observed oscillation modes resemble experimental observations gathered in connatural lab experiments for rising 4 mm diameter bubbles (LEIFER et al., 2000; their Figure 3d).

An equivalent spherical mean bubble diameter of d_{cher} ($r = (r_a^{2} * r_b^{2})^{(1/3)}$; SAM et al., 1996) from all Cherokee measurements reveal diameters d_{cher}=4.5 mm (σ=0.3) and a less accurate d_{JAGO}=6mm. Bubble size and shape as well as ebullition character (rise velocity, bubble successions, oscillations) at all vents were visually observed to be uniform.

In the easterly part of area *A'*, where hydroacoustic in situ monitoring revealed the number of seeps per area (SCHNEIDER VON DEIMLING et al., submitted), the submersible JAGO captured gas bubbles (f=7.0 Hz) taking 24 minutes to fill a 300 ml pressure housing (Figure 3d), giving an average flux of 12.5 ml/min. This value is 2.4 times larger than the previously reported seep hole flux estimate from HOVLAND and JUDD (1988) (= 10 mm diameter bubble every 6 seconds = 5.2 ml/min). The observed activity time during the sampling period matches the 70 % estimate from the GasQuant results (SCHNEIDER VON DEIMLING et al., submitted). The time to fill a definite volume by a uniform gas seep was used to estimate an average bubble diameter of d_{av}= 4.4 mm and matches the optical results given from the Cherokee data before.

Flare Imaging

The application of the previously described protocol for flare recognition revealed a total of more than 50 flares and defines 5 active venting localities *A-E* (Figure 2). Areas *A-C* are considered flare clusters (arbitrarily defined by more than 4 flares within 100 m) and cover an area of 76.100 m², 37.000 m² and 26.800 m², respectively. *A* clearly resembles the shape of the area termed 'gas charged upper sediments' in HOVLAND and SOMMERVILLE (1985), which plots with an offset of 230 m to the northeast. We thus suspect a positioning in-accuracy of the previous work from the time before the availability of GPS-based positioning.

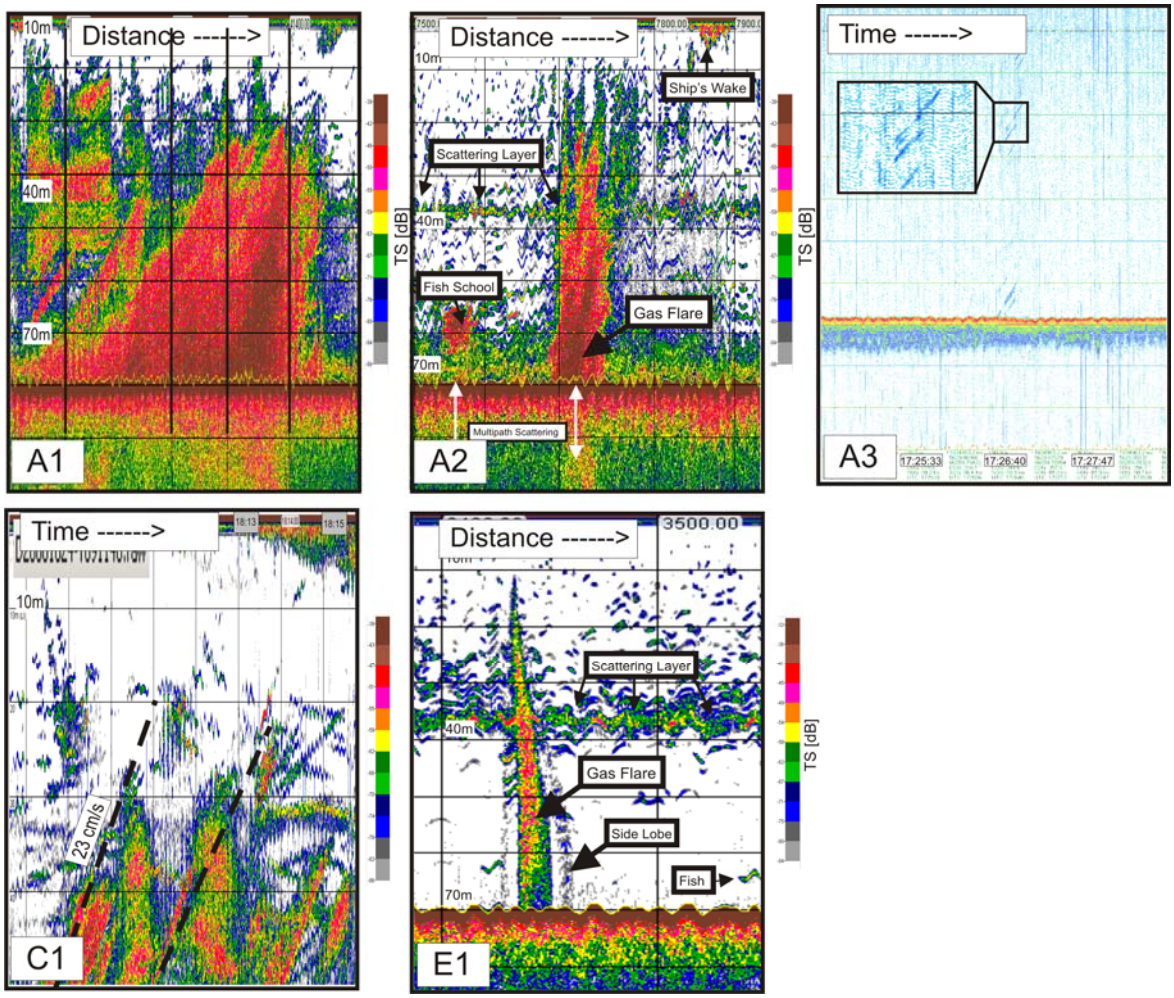

Figure 4: Flare examples from cluster locations A,C and E. Individual flares A1, A2, C1 and E1 were recorded on ALKOR using EK60 38 kHz and A3 during HEI 180 using the INNOMAR SES-2000 prototype system. Horizontal grid line spacing is 10 m in all plots. Vertical gridlines in A3 and C1 present time and 100m distance intervals elsewhere.

The total extent of the venting areas *A*, *B*, and *C* is ~140.000 m² (Table 1: A_{vent}) in accordance to the previously reported shallow gas area of 120.000 m² (Table 1, A_{sg}=120.000 m²), but 21 times larger than the 6500 m² previously defined venting area defined in HOVLAND and JUDD (1988) and even 40 times larger than the 3500m² area of active gas ebullition recently reported by NIEMANN et al. (2005). The previous underestimates are probably caused from minor focus on flare imaging during these studies and smaller sensitivity and coverage of the used sonar. Although pronounced flares arise at *D* and *E* (e.g. Figure 4, E1), they were not assigned an (flare cluster) area in this study, but considered as point sources due their limited lateral extent.

The center of *A* shows the highest abundance of flares (Figure 2, *A'*). Often the acoustic footprint covers several seep holes, that are locally less than 2 m apart from each other (SCHNEIDER VON DEIMLING et al., 2008), and cause very broad flares (Figure 4, A1). With

increasing distance from the major seepage area solitary flares were observed (Figure 4, A2) supporting the observed decreasing seep density with increasing distance from the center (HOVLAND and SOMMERVILLE, 1985). The falloff in seepage intensity from *A*' towards the outer areas is also evident by inspection of the scattering volume over a transect line crossing *A'* (Figure 5, inlet), showing a gaussian-shaped peak around the center of *A'* (Figure 5).

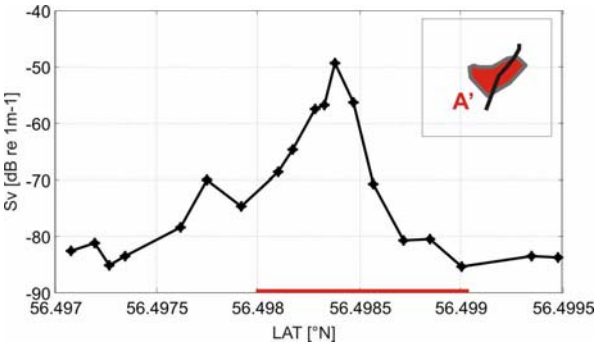

Figure 5: Volume scattering strength profile over the most intense seepage area A' (integration window 50 m width, 15 m height, close to the seafloor).

Flares within *B-E* generally plot weaker; they typically appear as solitary events like flare E1 (Figure 4), however they still reach up to 10 m below the sea surface. Towards the edge of the flare clusters, their widths and Sv-values decrease. Coincidently, solitarily rising bubbles or bubble groups appear as line plot bubble pattern, indicating single bubble streams in the acoustic cone (Figure 4, A3).

The maximum rising height of all detected flares was picked and binned into 10 classes (Figure 6) revealing, that over 80 % of the flares rise higher than 38 m and thus, into the upper mixed layer. Even a larger percentage of bubbles is expected to reach to this level, because the likelihood of bubble detection within the highly reduced insonified volume at short ranges gets smaller.

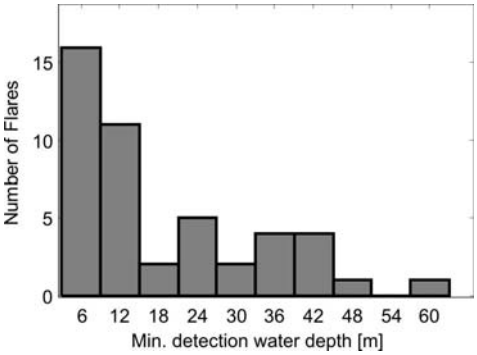

Figure 6: Histogram presentation of the flare heights of 46 flares detected during ALK 290. Flare detections within the upper well mixed layer plot in the 6 m-36 m bin interval.

Subbottom

A single west-east section crossing seep cluster *A* (see Figure 2, P for location) is presented in Figure 7. Reading the subbottom image from W to E, a distinct up-dipping reflector (DR) emerges at 115 ms and gradually rises towards the east until it merges into a high backscattering (HB visible by red clouds underneath the strong seafloor reflector) area directly beneath the seafloor, that is most likely caused from shallow gas. The length of this pinch out zone, where DR virtually disappears in the high scattering HB environment, is approximately 500 meter wide and thus matches the 470 m crossing length of P with area *A* (Figure 2, P). Within this zone, the highest backscatter plots around *A'*.

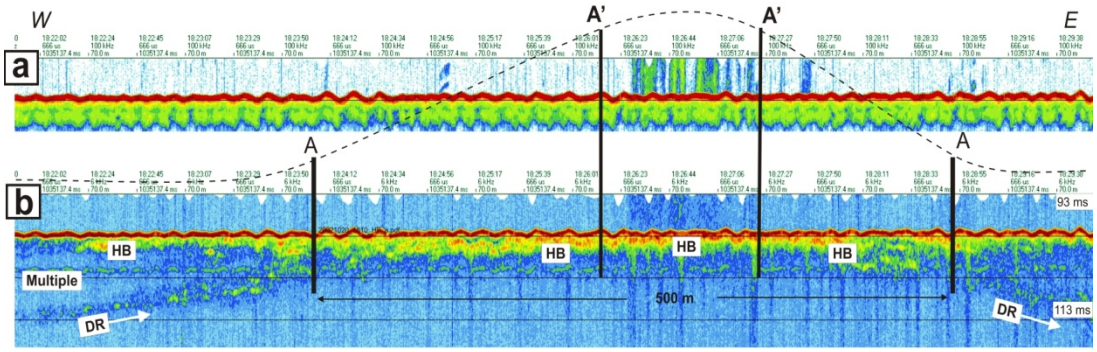

Figure 7: Combined sonar image of (a) primary/high and (b) parametric/low frequency data from the Innomar system crossing the main seepage area A from W to E (profile 20021020_1810). [Image source: DFG/BMBF project MUMM, RV ALKOR 267, chief scientist Antje Boetius], adapted.

The narrow DR layer was digitally picked along more than 10 profile lines covering the area shown in Figure 2 to gather longitude, latitude and depth b.s.f. values of DR. A continuous curvature spline gridding (WESSEL and BERCOVICI, 1998) was applied to this xyz dataset and is visualized in (Figure 8) to image areas with a shallow DR correlated to the seepage (NIEMANN et al., 2005).

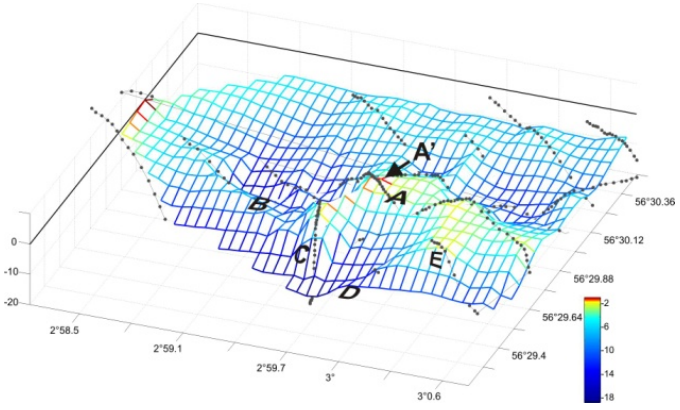

Figure 8: Doted lines represent picked DR coordinates along different survey lines as a base for the 3D interpolation grid of DR-depth b.s.f. Seep clusters area are labeled A-E. At the western boundary the palaeo-dome emerges (see text).Color code in mbsf.

A clear correlation between very shallow depth of DR (<1 ms below seafloor), high backscattering directly beneath the seafloor and maximum flare abundance was found to perfectly match with the assigned area of highest seepage intensity *A'* (Figure 8).

Due to a lack of subbottom data coverage, the southwestern part of the survey area appears blank in the grid and the depth of DR underneath *B* and *D* remains unknown. In the very northwestern part the gridded surface rises up high again. This is not caused by unstable gridding at the boundary but based on ambiguous DR picking.

A closer inspection of the acoustic image beneath this DR elevation in Figure 9 indicates not shallow gas but hard substrate to cause high backscatter intensity here. This might represent a sealed palaeo-seep, as has been suggested in HOVLAND (2002).

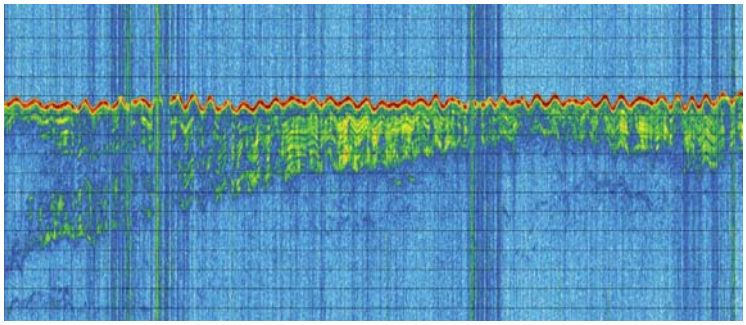

Figure 9: Subbottom line recorded in the northwesterly survey area showing layered reflectors. [Image source: DFG/BMBF project MUMM, RV ALKOR 267, chief scientist Antje Boetius]

Apart from the main seepage areas, subbottom data occasionally indicate isolated minor and ambiguous indications for shallow gas pockets of much weaker acoustic strength compared to HB in area *A'* and are attributed only little potential in terms of gas storage and seepage (Figure 10).

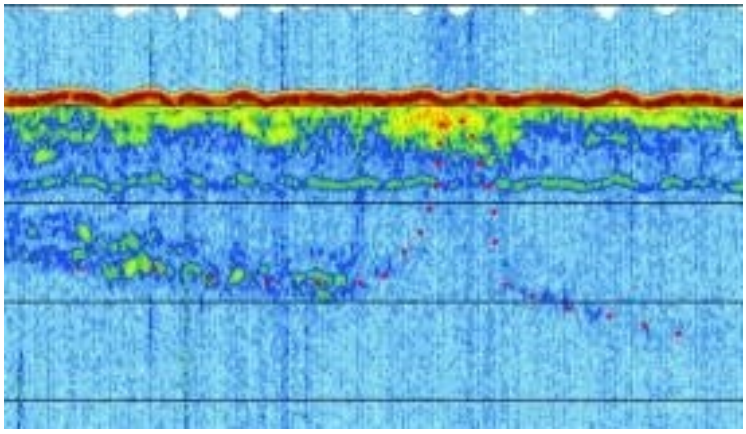

Figure 10: Local and shallow gas finding found between flare cluster A and B. [Image source: DFG/BMBF project MUMM, RV ALKOR 267, chief scientist Antje Boetius]

CTD and water sampling

Water column properties

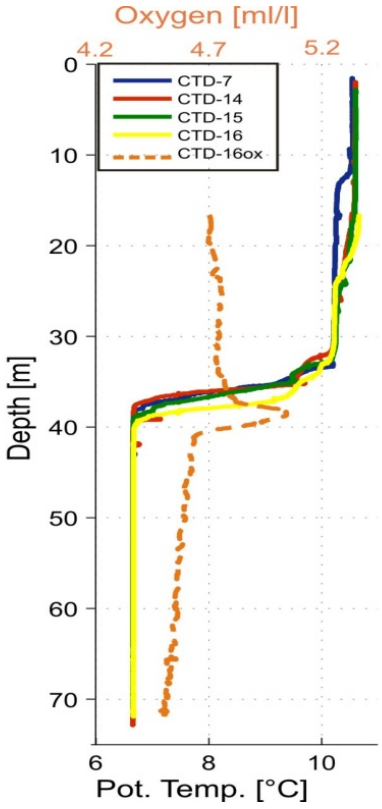

Figure 11: Vertical profile of potential temperature (CTD 7, 14, 15, 16) and dissolved oxygen (CTD16).

The hydrographic setting around Tommeliten in June 2005 is illustrated in Figure 11. CTD-7, 14 and 16 were conducted within, and CTD-15 1.2 nm south-southeast from the seepage area (Figure 2). The temperature profiles show a distinct thermocline with a temperature change of more than 4°C over ~6 m of water depth, but only a minor salinity change of 0.02 psu. Thus, the potential temperature is considered the controlling parameter of the observed strong density stratification in the water column. After inspection of all CTD data a consistent stratification scheme was found throughout the survey. A warm upper layer with a temperature of ~10.5°C reaches down to 32 m water depth. It can be subdivided into smaller layersthat arelikely to be caused by episodic wind and mixing events. Between 32-40 m water depth, a strong temperature gradient of > 0.5°C/m marks the position of the thermocline (layer II). Density variations below 40 m water depth are comparably low due to minor differences in temperature and salinity down to the seafloor.

The oxygen sensor data from *ALK 259* showed significant drift over time and the values in Figure 11 are not calibrated. However, the relative changes are valuable for this study. The introduced three layer model found in the temperature/density profile is also apparent in the oxygen distribution: Figure 11 reveals minor oxygen variation in layer *I*, which is expected to be close to equilibrium with the atmosphere. Towards the thermocline, a pronounced oxygen increase can be observed peaking at the layer *II/III* interface. Downwards, the declining oxygen peak extends a few meters into the uppermost part of the deep water layer *III*. From here, the oxygen concentration decreases towards the seafloor, though the entire water body of the North Sea is well oxygenated.

Methane concentration in the water column

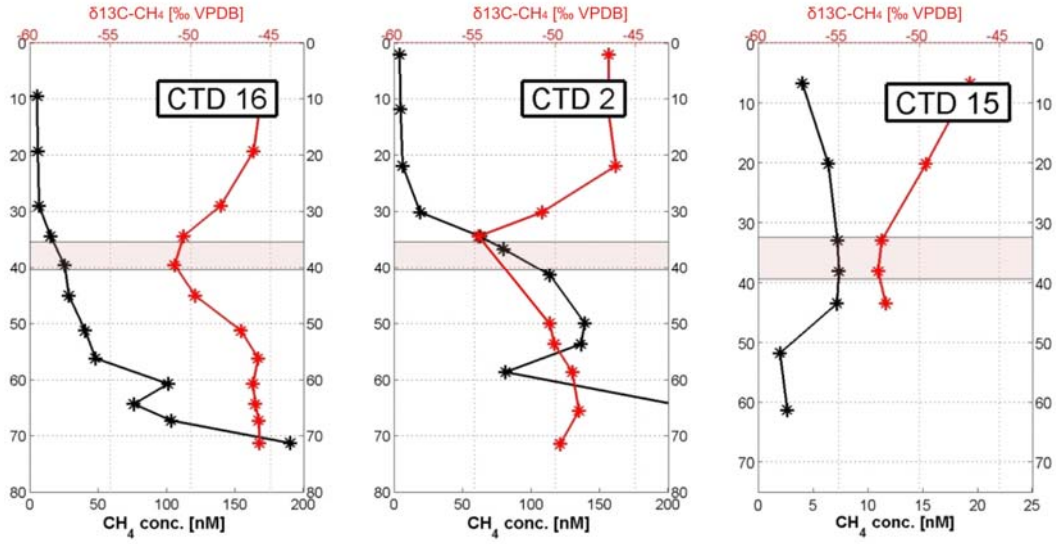

Figure 12: Vertical methane concentration (black) and $\delta^{13}C_{CH4}$ (red) data derived from CTD water sampling.

The methane profiles above seep cluster *A* and *B* show strong increase in concentration towards the seafloor with maximum concentrations frequently above 200 nmol/l, more than a factor of 40 above the local background. No perceptible change of the methane gradient is visible during the passage through the thermocline (Figure 12, red hued) as would have been expected if the upward transport was mainly driven by diapycnal mixing/eddy diffuse transport across the thermocline. From our observations, it thus appears that bubble dissolution is the main driver of the observed pattern, with bubble transport facilitating the path of the gas towards the upper mixed layer and atmosphere.

The mean monthly value of June, 2005, of 1.845 ppm at *Ocean Station M* (http://www.esrl.noaa.gov/gmd/ccgg/iadv/) at 66.00° N, 2.00° *E* was used to calculate the expected surface water methane equilibrium after WIESENBURG and GUINASSO (1979) to 2.73 nM. Accordingly, the measured mixed-layer methane concentrations between 5 and 15 nM indicate an oversaturation of ~180-550 %. Even 1.2 nM apart from the seep area, CTD-15 reveals an oversaturation the surface water of 125 %.

Generally, Tommeliten is strongly affected by the tides, and advection into various directions causes lateral dispersion and mixing of any dissolved constituent such as methane over time (see model results in REHDER et al., 1998; HAINBUCHER et al., 1987). Single profiles given in Figure 12 only represent a snapshot of the very local and time-variant methane distribution patterns, which are strongly affected by current flow regime and proximity of sampled water mass to rising gas bubbles, acting as vertical methane line source. Therefore, a large concentration range is expected to occur due to different levels of mixing. This is particularly apparent in Figure 13 showing a compilation of all *Alk 259* CTD methane cast data within the

study area during our survey (Figure 2). Overall, similar concentrations and gradients were shown as highlighted in Figure 12. However, the concentration variance is larger and this is attributed to a larger number of samples and corresponding broader range of tidal phases and mixing levels.

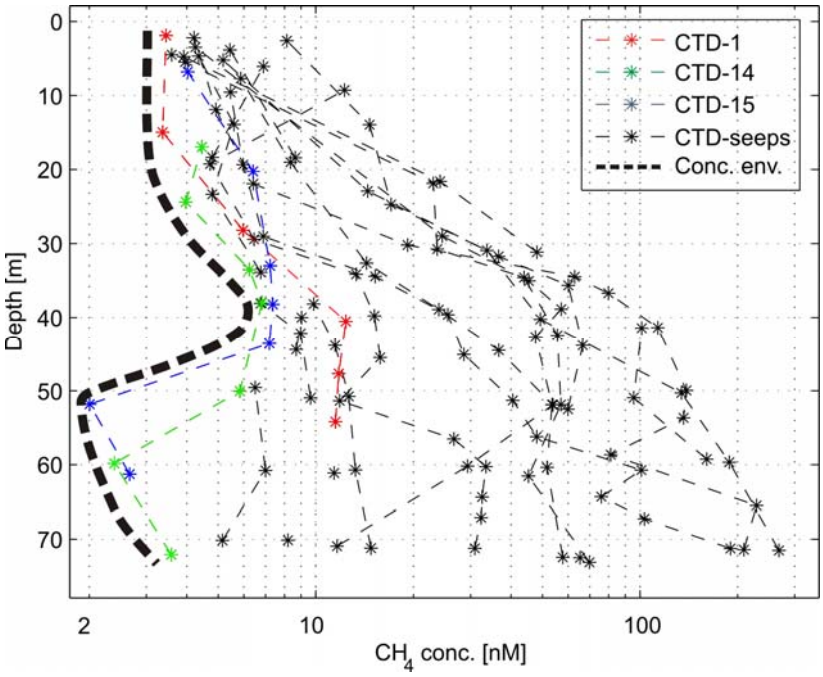

Figure 13: Methane concentration over depth gathered from all CTD casts within the seep area (legend: 'CTD-seeps') and background casts (CTD-1, CTD-14 and CTD-15 in color). The envelope of the local minimum methane concentration at each depth is drawn by a dashed black line (on the left side).

Lowest CH_4 concentrations of 2-3 nM appear between 50-60 m from off-seepage CTD casts. In contrast to previously reported background concentrations of 5 nM (NIEMANN et al., 2005), our values rather resemble the Atlantic inflow background concentrations of 2.5-3.5 nM (REHDER et al., 1998). Values from CTDs conducted within the seepage areas show minimum concentrations between 5-10 nM, which is considered the local background.

Even though the highest methane concentrations were measured close to the seafloor (see discussion), the largest minimum (Figure 13, envelope line) plots at 39 m water depth and corresponds well to the lower limit of the thermocline and the oxygen maximum. At this depth, all samples including those remote from seepage, show 6 nM or more are thus 2-3 times higher than the background of the surrounding water.

$\delta^{13}C$ isotopes of methane

The bottom-near $\delta^{13}C$-CH_4 values of CTD-16 range around -46 ‰ VPDB and thus comply well with the reported -45.6 ‰ VPDB $\delta^{13}C$-CH_4 values measured from captured gas bubbles (HOVLAND and SOMMERVILLE, 1985). Up to a water depth of 55 m the isotopic signal remains unchanged. Then, the methane becomes isotopically lighter towards the thermocline,

reaching values of -51 ‰ VPDB. Towards the sea surface the isotopic signature then approaches the atmospheric value of -47.3 ‰ VPDB (monthly mean June 2005, *Mace Head Station*, 53.33° N, 9.90° W, 25 meter above sea-level, (http://www.esrl.noaa.gov/gmd/ccgg/iadv). The local minimum of $\delta^{13}C\text{-}CH_4$ exactly plots on the lower base of the thermocline at the same depth, where the maximum of the methane background values and the local oxygen maximum occur. This was found both for the seep-influenced (e.g. CTD 16) and for the remote (e.g. CTD 15) stations.

Bubble modeling

Dissolution rate

Modeling reveals the dissolution rate of gas bubbles to be highest immediately after bubble release and then shows a steady decline during the rise towards the sea surface. E.g. a 3 mm diameter bubble initially (at 72 m depth) transfers 0.142 µmol/s into the water column. After a rise of only 20 m, less than 5 % of the initial value contributes to the transfer flux from the bubble into the water column (Figure 14). A larger bubble of 12 mm not only initially transfers more methane (1.881 µmol/s) due to the larger bubble surface, but also preserves more methane for later dissolution in shallower depth, giving rise to a different shape of the dissolution curvature. Under the prevailing conditions, the dissolution rate of an initial 12 mm bubble preserves 40 % of its initial dissolution rate 40 m above the seabed.

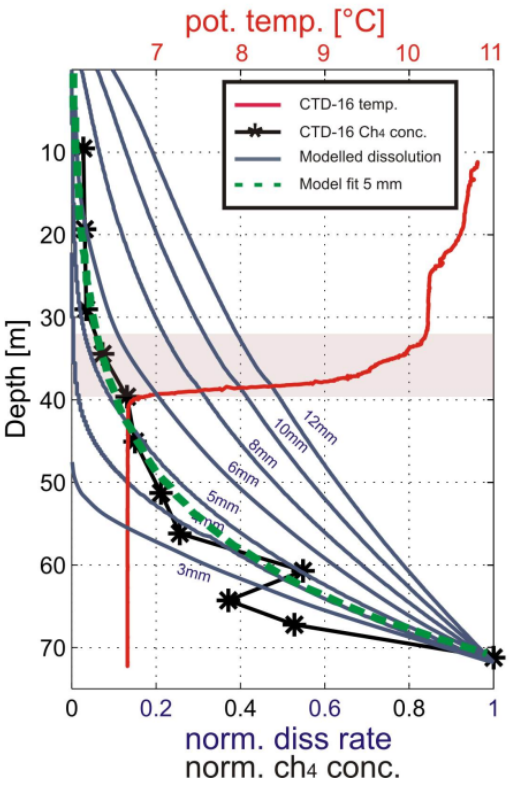

Figure 14: Plot showing temperature (red), CH_4 concentration (black), modeled bubble dissolution rate changes (blue) of seven initial bubble diameters (3 mm to 12 mm diameter), and a least squares fit (R^2=0.98) of a modeled 5 mm bubble (green) giving $f(z)=ae^{(bz)}$ with a=0.00638 and b=0.0716 (z= water depth). Methane concentration and modeled dissolution rate are normalized to their maximum values at the seafloor (CH_4_max=190 nM; $diss\_max_{3mm}$=-0.142µmol/s, $diss\_max_{12mm}$=-1.881 µmol/s at 72 m water depth)

We fitted the normalized dissolution rate for a typical 'Tommeliten' bubble being released with 5 mm initial diameter (Figure 14). As a result, a simple exponential function $f(z)=0.006e^{(0.071.*z)}$ is present to describe the generic vertical line source strength (1=max, 0=min) over depth z caused from typically 5 mm large bubbles released at the seabed of Tommeliten. This approximation of the depth dependent strength of the vertical methane line-source might be useful for future advection-diffusion modeling approaches to describe further pathways of bubble-mediated methane.

Bubble size and methane deposition

The results from the modeling demonstrate steady shrinkage and dissolution at specific depth of bubbles with 4 mm initial diameter or smaller (Figure 15). Larger bubbles first shrink but begin to grow close to the sea surface due to the non-linear pressure dependence of the gas expansion. For bubbles of an initial diameter larger than 10 mm, the model even predicts a net growth compared to the initial size of release. It has to be emphasized that the amount of gas molecules in such a surface bubble volume is still much lower due to the reduced pressure.

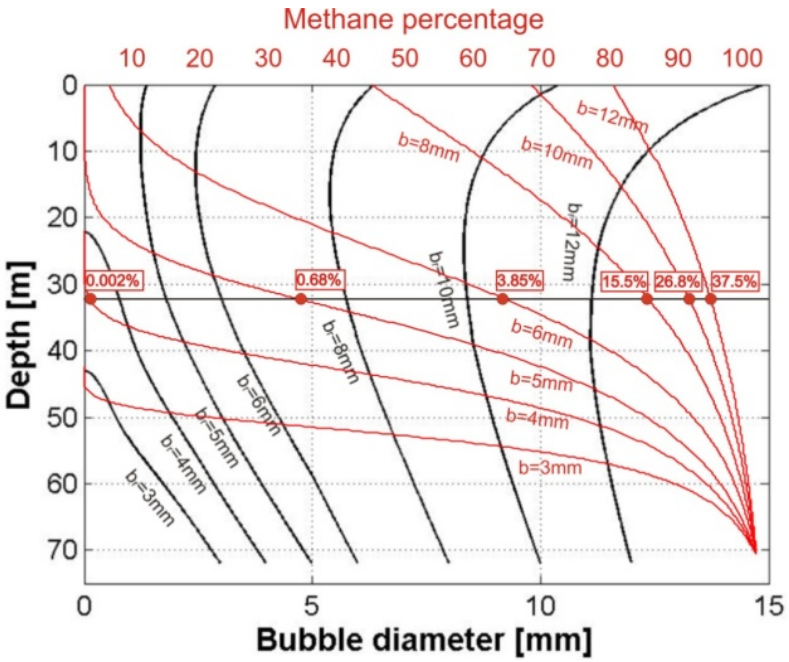

Figure 15: This multi-plot points (1) the change of initial bubble size during its rise towards the sea surface (black line) (2) the relative methane mol- percentage compared to other gases within a bubble at respective depth (red lines) (3) the remaining methane mol-percentage of a bubble compared to its initial mole amount of methane, directly after its release from the seabed (indicated by red dots and rectangles on the 32 m water depth); calculated for the release of pure methane bubbles rising from 72 m water depth. "b" denotes the initial bubble diameter for the corresponding model run.

The bubble growth towards the surface is not solely a pressure effect; moreover gas stripping processes during the rise lead to significant gas exchange, where methane leaves and mainly dissolved nitrogen and oxygen enters the bubble. Depending on the initial size, the bubble can reach the surface with nitrogen as the main component. The crucial effect of initial bubble size on direct bubble-mediated atmospheric methane impact at Tommeliten can be studied in Figure 15. Following the oceanographic data (Figure 11), 32 m water depth can be seen as a threshold level with regard to direct bubble-mediated gas transport into the well mixed upper layer and atmosphere. E.g. the remaining moles methane percentage of initial 4 mm, 5 mm, 6 mm, 8 mm and 10 mm bubbles after rise to the critical depth of 32 m was modeled to the range between 0.002 %, 0.68 % 3.85 %, 15.5 %, 26.8 %, and 37.5 % (Figure 15, red dots on the 32 m depth level).

Discussion

Seep bubble size

The results from the modeling of rising methane bubbles from 72 m water depth reveal a crucial effect of the initial bubble size on the further dissolution behavior at different depths and thus on the disposal zones of methane in the water column of Tommeliten. Moreover our total gas flux estimate in Tommeliten requires a good estimate of average bubble sizes released at the seafloor. Therefore, a range of bubble sizes is discussed, that are most likely to occur at Tommeliten.

Presumably, the observed 10 mm bubble release every 6 seconds (HOVLAND and JUDD, 1988) was not sampled at a representative site. Moreover, if all seeps spots would release 10 mm large bubble at 72 m depth, they would achieve the sea surface with a diameter of ~11 mm. It is likely that such large bubbles would have been detected visually during the long exploration and research history of Tommeliten.

Our video-guided bubble size measurements in the centre of the vent area revealed $d_{Cherokee}$=4.5±0.5 and d_{JAGO}=6±1 mm bubble diameters. This size range complies with the following discussion. The majority of the flares rise as high as 10 m below the sea surface (Figure 6). As indicated by the modeling (Figure 15), this requires an initial bubble diameter of more than 4 mm. The results suggest that bubbles with diameters ≤ 3.5 mm quantitatively dissolve before reaching the thermocline. This would cause a distinct bubble deposition layer (LEIFER and JUDD, 2002) and a steep gradient of the methane concentration between upper layer and the deep water. In contrast the vertical methane profiles point out increased methane concentrations across the thermocline.

Very few quantitative seep bubble size measurements exist. For the minor seepage sites in the Gulf of Mexico and the Shane Seep in the Santa Barbara Basin LEIFER and JUDD (2002) and LEIFER and BOLES (2005a) report a 5.4 mm and 7.0 mm peak diameter, respectively, in a per se gaussian-shaped bubble size distribution. A qualitative estimate of the same authors about continuous minor seeps in the UK 15/25 block (North Sea) show a narrow size distribution with a peak diameter of around 5 mm diameter. Our bubble size estimate reveals a range between 4 and 6 mm and thus fits very well with the reference literature values.

Flux estimate

Main seepage area A

Subbottom video and flare imaging data reveal a maximum seepage activity at *A'*, and decreasing seepage activity towards the outside of *A*. Such a decline is supported by the following findings: (1) Visual observations indicate a distinct decrease of seep hole abundance with increasing distance from the centre (HOVLAND and SOMMERVILLE, 1985); (2) flare density and scattering volume intensity reveal a concentric falloff from the center to the outside of *A* (Figure 2, 5); (3) the gas indicative dome structure (Figure 7) and its global maximum (corresponds to minimum depth b.s.f.) visible in the 3D gridded surface presentation (Figure 8) exactly fits to the major seepage area *A'*. Overall, the centre of *A* is attributed maximum seeping intensity. To meet this spatial dependency, *A* was subdivided into 50x50 m grid cells and classified in terms of flare abundance in each cell. Maximum flare density was assigned unity and no flare detection zero in a cell. A simple integration over the area *A* by use of this weighting grid and the measured reference seep density n_{GQ}=0.025 seeps per m² results in an estimate of n_A=550 seep holes in area *A*.

All investigations at Tommeliten assert the gas ebullitions to be of uniform character over space and time, i.e. similar release bubble sizes and small variance in ebullition rates. Emission rates between 4 and 8 bubbles per second and an estimated bubble diameter between 4 and 6 mm result in fluxes of f_{min}=8ml/min and f_{max}=54 ml/min in accordance to the reference measurement f_{JAGO}=12.5 ml/min within *A'*. Thus the total flux within *A* can be constrained using n_A*f*t (t=0.7, s. Table 1) to an in situ volume flux between 0.6 and 3.8 10^6 moles per year, respectively.

Peripheral zones

Research of Tommeliten gas ebullition has concentrated on flare cluster A, but this study shows even more acoustic and geochemical hot spots (*B*-*E*), where gas flares with similar heights (E1, A2/3) but reduced quantity were observed, and methane concentration above *B* indicate comparable source strength like in area *A.* The southerly succession of the dome in *A* towards *D* and *C* still suggests some linkage between seepage and doming here and further research is required to investigate the new gas vent findings. Acoustic and visual coverage in B-E is poor or even absent and no reference ebullition rate measurement is available. To rather derive a minimum flux estimate for Tommeliten gas seepage, *B* is arbitrary assigned an area-corrected 20 % source strength of f_A, and *C* only 10 % giving rise to fluxes f_B=[0.12; 0.77] and f_C=[0.06; 0.38] 10^6 mol/yr. Due to their small extent *D* and *E* are excluded from area-based calculations. Occasionally, elevated backscatter areas plot outside of the flare clusters (Figure 2). However, the backscatter intensity here is much weaker than inside of area *A* and cannot always unambiguously be attributed shallow gas and consequently is ignored for active area mapping and gas flux estimates.

Other sources of methane

Apart from methane bubble dissolution the water column may hold another prominent methane source, i.e. methanogenesis in the oxygenated upper water column, known to produce distinct subsurface methane maxima (KARL and TILBROOK, 1994; KIENE, 1991).

The measured $\delta^{13}C\text{-}CH_4$ minimum (Figure 12) accompanied with maximum oxygen (Figure 11) and a subsurface background methane maximum concentration around the thermocline (Figure 13, dashed line) strongly suggest such a methane production. The distinct density gradient at the thermocline potentially accumulates particulate organic matter in addition to enhanced access to nutrients. The oxygen maximum clearly indicates enhanced primary production in this depth range, as has been reported typical in this area due to variations of the thermocline during May/June (MOLL, 1998). Zooplankton habitually grazes those layers of phytoplankton and KARL and TILBROOK (1994) hypothesized methanogenic processes in zooplankton guts to cause the methane production and respective isotopic shift. Methanogenesis around the thermocline seems not confined to the Tommeliten area, because the oxygen peak was also observed at CTD-1 44 nm away from the discussed location.

Fate of methane

Bubble dissolution modeling and measured methane concentration at Tommeliten show enhanced bubble-mediated methane deposition at greater depth. Thus the methane is trapped below the upper-well mixed summer layer, were it would readily be degassed to the atmosphere by air-sea exchange processes. Given the water column profile during our survey in June 2005, less than 4% of the bubble-mediated methane immediately reaches the upper mixed layer. The remaining 96% deep/trapped methane is partially transported away from Tommeliten undergoing methane oxidation processes. However, VALENTINE et al. (2001) has shown that methane turnover times in such nano-molar methane concentration settings in seawater are long, in the order of several years. Thus, considerable amounts of methane may travel long distances, as was shown by REHDER et al. (1999). Seepage methane may eventually be transported into shallower hydrographic environments with enhanced vertical mixing and cause additional atmospheric ex-situ methane flux contribution. Whenever the Tommeliten methane plume migrates towards the south, it might partially reach the shallow Dogger Bank, where the lack of stratification allows for partial venting. As a hypothesis the Dogger Bank might serve as an atmospheric window for larger regional provenance of methane seepage. To further constrain this hypothesis modeling of passive tracers using an advection-diffusion model and $f(z)*fT_{omm}$ as a local line source strength is required to pursue the fate of the bubble-mediated methane originated at Tommeliten.

Even the deep/trapped methane that remains in well stratified provenances might be transferred into the atmosphere regarding the seasonality of the North Sea. In autumn surface cooling and enhanced storm activity lead to weakening the thermoclinic stratification from above and strongly increases the vertical mixing (Figure 1).

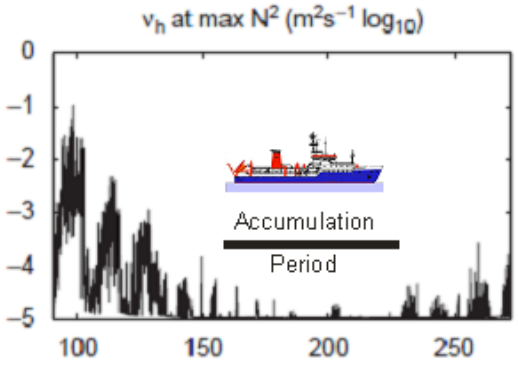

Figure 16: Modeled timeseries of vertical eddy diffusion in the central North Sea at the maximum stability frequency (within the thermocline) for one season modified after HOLT and UMLAUF (2008).

HOLT and UMLAUF (2008) provide modeled time series of seasonal vertical mixing, showing several orders of magnitude variation for an exemplary grid cell in the Central North Sea (Figure 16). Given this seasonality we therefore predict highly enhanced methane flux from the accumulated and trapped spring/summer methane from the deep water into the

atmosphere after the breakdown of the thermocline, that are missed during research cruises in summer.

Conclusion

Various acoustic datasets gathered at Tommeliten were analyzed and reveal a 21fold larger gas venting area than previously reported. A total of 550 individual gas vents is estimated within the main vent field (area *A*). In situ ROV gas flux measurements and a general acoustic seep mapping and characterization allowed to constrain the flux for the entire vent field (*A-E*) between ~0.8-and ~4.8*10^6 mol/year. A distinct evidence for extra methane production in the upper water column was detected, but the source strength remains unclear. Model results reveal an efficiency of less than 4 % from direct bubble-mediated transport during the summer into the upper well mixed layer, where the methane is immediately accessible for air sea exchange. However, considering the seasonal hydrographic variations in the North Sea, our study suggests even quantitative transport of Tommeliten seep methane into the atmosphere during the winter, and venting of the accumulated methane below the thermocline during the breakdown of stratification in fall.

References

Anderson, A. L. and Hampton, L. D., 1980. Acoustics of gas-bearing sediments. I. Background. *J. Acoust. Soc. Am.* 67, 1865-1889.

Artemov, Y. G., Egorov, V. N., Polikarpov, G. G., and Gulin, S. B., 2007. Methane emission to the hydro- and atmosphere by gas bubble streams in the Dnieper paleo-delta, the Black Sea. *Reports of the Natl. Acad. of Sci. of Ukraine* 5, 110-116.

Blake, D. and Rowland, F., 1988. Continuing worldwide increase in tropospheric methane, 1978 to 1987. *Science* 239, 1129–1131.

Boetius, A., Ravenschlag, K., Schubert, C., Rickert, D., Widdel, F. G., A., Amann, R., Jorgensen, B. B., Witte, U., and Pfannkuche, O., 2000. A marine microbial consortium apparently mediating anaerobic oxidation of methane. *Nature* 407, 623-626.

Clift, R., Grace, J. R., and Weber, M. E., 1978. *Bubbles, Drops, Particles*. Academic Press, New York.

Commander, K. W. and Moritz, E., 1989. Off-resonance contributions to acoustical bubble spectra. *J. Acoust. Soc. Am.* 85, 2665-2669.

Greinert, J., Artemov, Y., Egorov, V., De Batist, M., and McGinnis, D., 2006. 1300-m-high rising bubbles from mud volcanoes at 2080m in the Black Sea: Hydroacoustic characteristics and temporal variability. *Earth and Planetary Science Letters* 244, 1-15.

Hainbucher, D., Pohlmann, T., and Backhaus, J., 1987. Transport of conservative passive tracers in the North Sea: first results of a circulation and transport model. *Continental Shelf Research* 7, 1161-1179.

Hayduk, W. and Laudie, H., 1974. Prediction of diffusion coefficients for nonelectrolytes in dilute aqueous solutions. *AIChE Journal* 20, 611-615.

Heeschen, K. U., Collier, R. W., de Angelis, M. A., Suess, E., Rehder, G., Linke, P., and Klinkhammer, G. P., 2005. Methane sources, distributions, and fluxes from cold vent sites at Hydrate Ridge, Cascadia Margin. *Global Biogeochemical Cycles* 19, 1-19.

Hinrichs, K.-U. and Boetius, A., 2002. The anaerobic oxidation of methane: New insights in microbial ecology and biogeochemistry In: Wever, G., Billett, D., Hebbeln, D., Jørgensen, B. B.,

Schlüter, M., and van Weering, T. C. E. Eds., *Ocean Margin Systems*. Springer-Verlag, Heidelberg.

Hinz, K., Kögler, F., Richter, I., and Seibold, E., 1971. Reflexionsseismische Untersuchungen mit einer pneumatischen Schallquelle und einem Sedimentecholot in der westlichen Ostsee. Teil II Untersuchungsergebnisse und geologische Deutung. *Meyniana* 21, 17-24.

Holt, J. and Umlauf, L., 2008. Modelling the tidal mixing fronts and seasonal stratification of the Northwest European Continental shelf. *Continental Shelf Research* 28, 887-903.

Hornafius, J. S., Derek, Q., and Luyendyk, B. P., 1999. The world´s most spectacular marine hydrocarbon seeps (Coal Oil Point, Santa Barbara Channel, California): Quantification of emissions. *Journal of Geophysical Research* 104, 20703-20712.

Hovland, M., 2002. On the self-sealing nature of marine seeps. *Continental Shelf Research* 22, 2387-2394.

Hovland, M. and Judd, A. G., 1988. Seabed pockmarks and seepages. Graham and Trotman, London.

Hovland, M. and Sommerville, J. M., 1985. Characteristics of two natural gas seepages in the North Sea. *Marine and Petroleum Geology* 2, 319-326.

IPCC, 2007. Climate Change. Fourth Assessment Report of the IPCC. Cambridge University Press, Cambridge.

Judd, A., 2001. Pockmarks in the UK sector of the North Sea. *Technical Report TR_002*.

Judd, A., Davies, G., Wilson, J., Holmes, R., Baron, G., and Bryden, I., 1997. Contributions to atmospheric methane by natural seepages on the UK continental shelf. *Marine Geology* 137, 165-189.

Judd, A. G., 2004. Natural seabed gas seeps as sources of atmospheric methane. *Environmental Geology* 46, 988-996.

Judd, A. G. and Hovland, M., 2007. *Seabed Fluid Flow*. Cambridge University Press, New York.

Karl, D. M. and Tilbrook, B. D., 1994. Production and transport of methane in oceanic particulate organic matter. *Nature* 368, 732-734.

Keir, R. S., Greinert, J., Rhein, M., Petrick, G., Sültenfuß, J., and Fürhaupter, K., 2005. Methane and methane carbon isotope ratios in the Northeast Atlantic including the Mid-Atlantic Ridge (50°N). *Deep-Sea Research I* 52, 1043-1070.

Kiene, R. P., 1991. In: Rogers, J. E. and Whitman, W. B. Eds. *Microbial Production and Consumption of Greenhouse Gases: Methane, Nitrogen Oxides, Halomethanes*. American Society for Microbiology, Washington, DC.

Kvenvolden, K. A., Reeburgh, W. S., and Lorenson, T. D., 2002. Naturally occurring methane seepage-Workshop report. *EOS Trans. AGU* 82, 457.

Lammers, S. and Suess, E., 1994. An improved head-space analysis method for methane in seawater. *Mar. Chem.* 47, 115-125.

Leifer, I. and Boles, J., 2005a. Measurement of marine hydrocarbon seep flow through fractured rock and unconsolidated sediment. *Marine and Petroleum Geology* 22, 551-568.

Leifer, I. and Boles, J., 2005b. Turbine tent measurements of marine hydrocarbon seeps on subhourly timescales. *Journal of Geophysical Research* 109, 1-12.

Leifer, I., de Leeuw, G., and Cohen, L. H., 2001. Optical Measurement of Bubbles: System Design and Application. *Journal of Atmospheric and Oceanic Technology* (submitted), 1-14.

Leifer, I. and Judd, A. G., 2002. Oceanic methane layers: The hydrocarbon seep bubble deposition hypothesis. *Terra Nova* 16, 471-485.

Leifer, I. and MacDonald, I., 2003. Dynamics of the gas flux from shallow gas hydrate deposits: interaction between oily hydrate bubbles and the oceanic environment. *Earth and Planetary Science Letters* 210, 411-424.

Leifer, I. and Patro, R. K., 2002. The bubble mechanism for methane transport from the shallow sea bed to the surface: A review and sensitivity study. *Continental Shelf Research* 22, 2409-2428.

Leifer, I., Patro, R. K., and Bowyer, P., 2000. A study on the temperature variation of rise velocity for large clean bubbles. *J. Atmospheric and Oceanic Technology* 17, 1392-1402.

Lyons, A. P., Duncan, M. E., Anderson, A. L., and Hawkins, J. A., 1996. Predictions of the acoustic scattering response of free-methane bubbles in muddy sediments. *Journal of the Acoustical Society of America* 99, 163-172.

MacDonald, I. R., Boland, G. S., Baker, J. S., Brooks, J. M., Kennicutt II, M. C., and Bidigare, R. R., 1989. Gulf of Mexico hydrocarbon seep communities. *Marine Biology* 101, 235-247.

McGinnis, D. F., Greinert, J., Artemov, Y., Beaubien, E., and Wuest, A., 2006. Fate of rising methane bubbles in stratified waters: How much methane reaches the atmosphere? *JGR* 111, 1-15.

Medwin, H., 1977. Acoustical determinations of bubble-size spectra. *Journal of the Acoustical Society of America* 62, 1041-1044.

Merewether, R., Olsson, M. S., and Lonsdale, P., 1985. Acoustically Detected Hydrocarbon Plumes Rising From 2-km Depths in Guaymas Basin, Gulf of California. *Journal of Geophysical Research* 90, 3.075-3.085.

Moll, A., 1998. Regional distribution of primary production in the North Sea simulated by a three-dimensional model. *Journal of Marine Systems* 16, 151–170.

Niemann, H., Elvert, M., Hovland, M., Orcutt, B., Judd, A., Suck, I., Gutt, J., Joye, S., Damm, E., Finster, K., and Boetius, A., 2005. Methane emission and consumption at a North Sea gas seep (Tommeliten area). *Biogeosciences* 2, 335-351.

Ohle, W., 1960. Fernsehen, Photographie und Schallortung der Sedimentoberfläche in Seen. *Arch. Hydrobiol.* 57, 135-160.

Ostrovsky, I., 2003. Methane bubbles in Lake Kinneret: Quantification and temporal and spatial heterogenity. *Limnol. Oceanogr.* 48, 1030-1036.

Pohlmann, T., 1996. Calculating the annual cycle of the vertical eddy viscosity in the North Sea with a three-dimensional baroclinic shelf sea circulation model. *Continental Shelf Research* 16, 147-161.

Rehder, G., Keir, R. S., Suess, E., and Pohlmann, T., 1998. The Multiple Sources and Patterns of Methane in North Sea Waters. *Aquatic Geochemistry* 4, 403-427.

Rehder, G., Keir, R. S., Suess, E., and Rhein, M., 1999. Methane in the northern Atlantic controlled by microbial oxidation and atmospheric history. *Geophysical Research Letters* 26, 587-590.

Rehder, G. and Suess, E., 2001. Methane and pCO2 in the Kuroshio and the South China Sea during maximum summer surface temperatures. *Marine Chemistry* 75, 89-108.

Rettich, T. R., Handa, Y. P., Battino, R., and Wilhelm, E., 1981. Solubility of gases in liquids. 13. High-precision determination of Henry's constants for methane and ethane in liquid water at 275 to 328 K. *The Journal of Physical Chemistry* 85, 3230-3237.

Rigby, M., Prinn, R. G., Fraser, P. J., Simmonds, P. G., Langenfelds, R. L., Huang, J., Cunnold, D. M., Steele, L. P., Krummel, P. B., Weiss, R. F., O'Doherty, S., Salameh, P. K., Wang, H. J., Harth, C.M., Mähle, J., and Porter, L.W., 2008. Renewed growth of atmospheric methane. *Geophys. Res. Lett.* 35.

Sahling, H., Bohrmann, G., Artemov, Y. G., Bahr, A., Brüning, M., Klapp, S. A., Klaucke, I., Kozlova, E., Nikolovska, A., Pape, T., Reitz, A., and Wallmann, K., 2009, in press. Vodyanitskii mud volcano, Sorokin trough, Black Sea: Geological characterization and quantification of gas bubble streams. *Marine and Petroleum Geology*.

Sam, A., Gomez, C. O., and Finch, J. A., 1996. Axial velocity profiles of single bubbles in water / frother solutions. *Int. J. Miner. Process.* 47, 177-196.

Sauter, E. J., Muyakshin, S. I., Charlou, J.-L., Schlüter, M., Boetius, A., Jerosch, K., Damm, E., Foucher, J.-P., and Klages, M., 2006. Methane discharge from a deep-sea submarine mud volcano into the upper water column by gas hydrate-coated methane bubbles. *Earth and Planetary Science Letters* 243, 354-365.

Schmale, O., 2006. Submarine Methane Seepage in the Paleo Dnepr Area and Sorokin Trough and its Influence on the Black Sea Methane Budget, *PhD thesis*, Christian-Albrechts-Universität, Kiel.

Schneider von Deimling, J., Greinert, J., Chapman, N. R., Rabbel, W., and Linke, P., submitted 2008. Acoustic imaging of natural gas bubble ebullition in the North Sea: Sensing the temporal, spatial and activity variability. *Limnol. Oceanogr.*

Schneider von Deimling, J., Greinert, J., and Linke, P., 2008. GasQuant - Hydroacoustic monitoring of a natural gas seep field (Tommeliten, North Sea) *ICGH*, Vancouver.

Schroot, B. M., Klaver, G. T., and Schüttenhelm, R. T. E., 2005. Surface and subsurface expressions of gas seepage to the seabed--examples from the Southern North Sea. *Marine and Petroleum Geology* 22, 499-515.

Schumacher, D. and Abrams, M. A., 1994. Hydrocarbon Migration and its Near-Surface Expression. In: Thrasher, J., Fleet, A. J., Hay, S. J., Hovland, M., and Düppenbecker, S. Eds.*Understanding Geology as the Key to Using Seepage in Exploration: The Spectrum of Seepage Styles*. The American Association of Petroleum Geologists, Oklahoma.

Torres, M. E., McManus, J., Hammond, D. E., de Angelis, M. A., Heeschen, K. U., Colbert, S. L., Tryon, M. D., Brown, K. M., and Suess, E., 2002. Fluid and chemical fluxes in and out of sediments hosting methane hydrate deposits on Hydrate Ridge, OR, I: Hydrological provinces. *Earth and Planetary Science Letters* 201, 525-540.

Valentine, D. L., Blanton, D., Reeburgh, W. S., and Kastner, M., 2001. Water column methane oxidation adjacent to an area of active hydrate dissociation, Eel River Basin. *Geochim. Cosmochim. Acta* 65, 2633-2640.

Wegener, G., 2008. Methane Oxidation and Carbon Assimilation in Marine Sediments, *PhD thesis*, University Bremen.

Wessel, P. and Bercovici, D., 1998. Interpolation with Splines in Tension: A Green's Function Approach. *Mathematical Geology* 30, 77-93.

Whitecar, M. J., 1999. Carbon and hydrogen isotope systemativs of bacterial formation and oxidation of methane. *Chemical Geology* 161, 291-314.

Wiesenburg, D. A. and Guinasso, N. L. j., 1979. Equilibrium solubilities of methane, carbon monoxide, and hydrogen in water and seawater. *J. Chem. and Engin. Data* 24, 356-360.

General conclusion and outlook

In this thesis various hydroacoustic tools and corresponding processing/visualization techniques have been combined for the detection of seep gas bubbles in the water column. A processing procedure for gas bubble detection in multibeam mapping sonar data was introduced showing the advantage of multibeam compared to singlebeam systems, the latter being a standard tool in seep gas bubble research up to the present time. In contrast, multibeam technology offers larger coverage, better resolution and thus exact georeferencing of echo signals and the position of the gas source on the seafloor. Moreover, potential relationships between gas release and geological features such as pockmarks, ridges or mud volcanoes can be examined with mapping sonar systems. The next generation of multibeam mapping systems (water column scanning) is currently entering the market and – based on the results of this study - we attribute this novel technology a major importance especially in the field of gas seepage research in the near future. However, vast increase in the amount of recorded data will require sophisticated data processing, visualization, and design of automated feature detection algorithms; potential solutions are presented in this thesis.

Exemplary, we showed water column multibeam data gathered by a prototype WCI multibeam system (GasQuant). Even single gas bubble streams could be detected in the form of characteristic echo patterns. To visualize those patterns, water current velocity data were incorporated into the data processing. This allowed prediction of the bubble displacement governed by environmental currents and rise velocity. Thus, discrimination of bubble- against ambient echo-signals (e.g. fish-echoes) becomes feasible. This novel approach is promising because (1) velocity data are nowadays often concurrently gathered with ADCP systems during surveying (2) up-to-date numerical models provide reliable velocity data (3) computer power is sufficient to extend data processing in terms of sophisticated algorithmic object detection.

In the acoustic seep research community a straightforward quantification of gas flux using hydroacoustics is often assumed. However, we suggest that much more research is needed in this field. Acoustic inversion of gas seepage requires determination of the ebullition type in terms of bubble size spectra, shape, and surface composition of gas bubbles (hydrate-covered or not), and seep bubble density compared to sonar footprint size. We propose acoustic inversion after parameterization of seepage ebullition type, and stress the need of exact solutions for the acoustic response to a fluid/gaseous seep bubble of respective cross-sectional shape and surface character (similar as was performed in fishery acoustics). Model

results presented in the Appendix of this study suggest that only minor seepage can readily be quantified with active hydroacoustic systems, whereas for violent seepage only a minimum gas flux estimate can be drawn from backscatter analysis. In case of violent seepage, the relation between backscatter and gas flux is extremely complicated and unpredictable without the exact knowledge of bubble size spectra; moreover multiple scattering and acoustic absorption effects can not be neglected any longer. Mapping of the three-dimensional bubble plume shape and analysis of its extent and current-induced deflection might give rise to better estimates about total gas flux than pure backscatter inversion.

Most research work so far has concentrated either on hydroacoustic or geochemical approaches. This study however uses an integrated approach. Combining hydroacoustic, geochemical, and ROV observations allowed for a methane gas seepage source strength estimate for the entire vent field of Tommeliten (North Sea) between ~0.8 and ~4.8*10^6 mol/yr released at the seafloor in the form of gas bubbles. Compared to other gaseous methane seep sites word-wide, this is a significant quantity and Tommeliten should be noted in this context. Moreover, another CH_4 source appears to be present in the mid-water column, but the definition of the source requires further analysis of e.g. $\delta^{13}C$-CH_4 and particle analysis, which could be subject to future research. The fate of the bubble-mediated methane was pursued by geochemical sampling and gas bubble dissolution modeling. Model results disclose an efficiency of less than 4 % from bubble methane transport during the summer into the upper well mixed layer, where it is immediately accessible for air sea exchange. Most of the seepage methane remains in the deep water and is thus decoupled from air-sea exchange as long as the typical summer stratification persists. Thus, a continuous accumulation of methane in the deep water of the Central and Northern North Sea is likely to occur after stratification has established in spring/summer. With regard to the seasonal hydrographic variations in the North Sea, quantitative transport of Tommeliten seep methane into the atmosphere is likely towards the winter after the breakdown of stratification.

This seasonal bias is not only constrained to the study site, but relevant for the entire Central and Northern North Sea as well as for many mid-latitude shallow shelf sea waters showing temporal stratification. Marine research cruises in mid-latitude areas predominantly take place during the calmer summer season. Thus, published surficial methane data from those cruises probably underestimate the yearly budget of seep-mediated methane flux contribution to the atmosphere.

Appendix A

Patent Aktenzeichen 102009033724.5*: Bubble-Detektionsverfahren in der Wassersäule

pva: Patent Verwaltungsagentur Schleswig-Holstein

Verfasser: Jens Schneider von Deimling Kiel, 15.10.2007

Stand der Technik

Sogenannte Fernerkundungssysteme erlauben das Sammeln von Information über Objekte aus der Ferne, d.h. eine direkte (in situ) Untersuchung oder Probenahme ist dazu nicht zwingend erforderlich. In den vergangenen Dekaden erlangte die Fernerkundung große Bedeutung im militärischen Bereich (Aufklärung), sowie in der von Satelliten gestützten Analyse der Erdatmosphäre und der Erdoberfläche. Vorzugsweise kommen hierbei elektromagnetische Verfahren zum Einsatz. Ein prominentes Beispiel sind an Land stationierte Radarsysteme, die zur Überwachung des Flugraumes dienen. Dagegen unterliegt die elektromagnetische Fernerkundung der Hydrosphäre großen Einschränkungen, denn die starke Dämpfung kurzwelliger Strahlung in Wasser lässt nur geringe Eindringtiefen zu. Für langwellige, akustische Strahlung ist Wasser jedoch bis in große Tiefen transparent und infolgedessen haben sich sogenannte hydroakustische Systeme im Frequenzbereich zwischen 3-500 kHz als Fernerkundungs-Geräte zur Untersuchungen der Wassersäule sowie zur Vermessung des Meeresbodens (Echolote) durchgesetzt.

Generell muss zwischen aktiven und passiven Fernerkundungssystemen unterschieden werden. Passive Systeme besitzen lediglich eine Empfangseinheit und sind damit auf externe Signalquellen (z.B. reflektiertes Sonnenlicht) angewiesen. Dagegen bestehen aktive Systeme aus einer Empfangs- und Sendeeinheit, wobei letztere elektromagnetische bzw. akustische Pulse sendet. Anschließend wartet das Empfangsmodul auf mögliche Reflektionen bzw. das Echo. Moderne Systeme tasten während des Lauschvorganges die eingehenden analogen Signale digital ab und speichern diese als komplexe Zeitreihenwerte ab. Je nach verwendeter Wellenlänge, Signalstärke, Signal-Rauschverhältnis und Beschaffenheit eines möglichen Reflektors können in den Daten Reflektoren anhand charakteristischer Merkmale (Amplitude/Phase, Frequenz) detektiert und gegebenenfalls identifiziert werden. Mehrstrahlige Systeme, die einen sogenannten Fächer überdecken, erlauben das gerichtete Senden und Empfangen von elektromagnetischen oder akustischen Wellen in schneller Abfolge. Der Vorteil solcher Anlagen besteht in einem verbessertem Signal Rauschverhältnis, der größeren Überdeckung des Untersuchungsraumes, der exakten Lokalisierung möglicher Reflektoren sowie die Analyse deren räumlich-zeitlicher Entwicklung (Position, Beschaffenheit). Bekannte Beispiele hierfür sind sich bewegende Flugzeuge auf den Radarschirmen der Flugüberwachung.

Im Marinen werden hydroakustische Systeme u.a. eingesetzt, um vom Meeresboden aufsteigende Gasblasen in der Wassersäule zu finden. In Folge des großen Impedanz-Unterschieds an der Wasser-Gas Grenzschicht und möglicher Eigenschwingung von Blasen agieren diese als starke Reflektoren bzw. Oszillatoren und strahlen ein starkes Echo ab. Anschließende Laufzeitmessung der ausgesandten akustischen Signale ermöglicht eine ungefähre Tiefenangabe der jeweiligen Schall- bzw. Echoquelle. Mehrere zeitlich aufeinanderfolgende Lotungen und daraus resultierende Zeitreihen werden als Echogramme zusammengefasst, worin sich Steig- oder Sinkbewegungen der entsprechenden Reflektoren studieren lassen. Aufsteigende Gasblasen zeichnen sich in Echogrammen häufig als typische Muster ab (JUDD et al., 1997; ARTEMOV et al., 2007)) und können mittels visueller Interpretation von z.B. von Fischen erzeugten Fremdechos unterschieden werden. Die hierbei notwendigen hohen Abtastraten resultieren in großen Datenmengen und deren Auswertung ist daher zeitaufwendig und nur von geschultem Fachpersonal durchführbar.

Gemäß dem Stand der Technik konnten Wassersäulendaten bislang meist nur von Einstrahl-Echoloten aufgezeichnet werden. Moderne Signalverarbeitungstechnologie und erhöhte Datenträgerkapazitäten heutiger Mehrstrahl-Systeme ermöglichen neuerdings die Speicherung der Wassersäulendaten eines gesamten Fächers. So entsteht ein akustisches Abbild aller Strahlrichtungen und Tiefen über die gesamte Wassersäule. Mit jeder wiederholten Lotung wird die räumlich-zeitliche Veränderung des akustischen Abbildes erfasst. Allerdings resultieren aus diesen modernen Multibeam Systemen so große Datensätze (bis zu 2 Gigabyte pro Minute) dass eine manuelle Auswertung kaum möglich ist.

Im Folgenden wird daher ein automatisiertes Verfahren beschrieben, mit welchem große Datenmengen auf sich bewegende Objekte hin analysiert werden können.

Beschreibung des Verfahrens

Wird mittels eines Fernerkundungssystems ein *N*-dimensionaler Raum ($N \in [1..\infty]$) in zeitlicher Folge untersucht, so ist es unter gegebenen Umständen möglich einen sich darin bewegenden Körper per Algorithmus zu detektieren und zu identifizieren.

Die Geschwindigkeit $\vec{v}$ eines Körpers/Reflektors im Untersuchungsraum resultiert aus der Vektoraddition dessen Eigengeschwindigkeit $\vec{v}_r$ und der vom Strömungsvektor des umgebenden Mediums auf den Körper übertragene Geschwindigkeit $\vec{v}_m(f)$, wobei *f* eine bekannte Funktion der Übertragungsgüte von Medium auf den Körper darstellt (1).

$$\vec{v} = \vec{v}_m + \vec{v}_r \tag{1}$$

Sind $\vec{v}_m$ und $\vec{v}_r$ bekannt, so kann ein Verschiebungsvektor eines Körpers/Reflektors im Zeitintervall Δt vorausgesagt werden. Umgekehrt kann aus einem Datensatz der Versatz eines wandernden Reflektors während der Zeitspanne t_2-t_1 zwischen zwei Orten s_1 und s_2 abgelesen werden. Der Einfachheit halber betrachten wir das vierdimensionale Problem anhand eines 3-dimensionalen Beispiels (2 Raumrichtungen, 1 Zeitdimension, Fig. 1). Zum Zeitpunkt t_1 befinde sich der Körper bei s_{22}. Im weiteren Verlauf verursacht $\vec{v}$ eine Drift des Körpers von s_{33} bei t_2 nach s_{34} bei t_3. Die gemittelte Momentangeschwindigkeit $\vec{v}_{\overline{mess}}$ mit welcher sich ein Reflektor im Array zwischen t_1 und t_3 bewegt, ergibt sich aus (2)

$$\vec{v}_{\overline{mess}} = \frac{\sqrt{\Delta x^2 + \Delta y^2}}{t_3 - t_1} \tag{2}$$

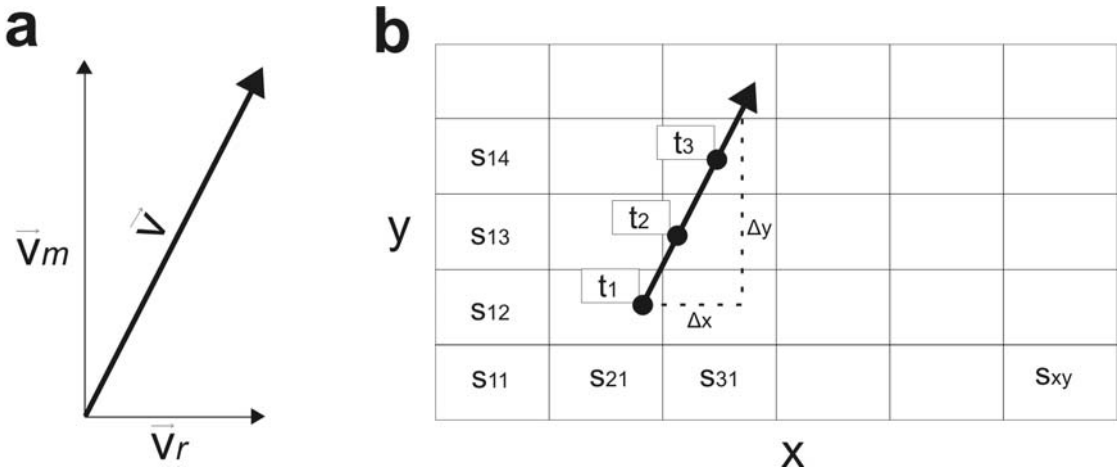

Figure 1: ***a*** *Vektoraddition der Eigengeschwindigkeit* $\vec{v}_r$ *und der von der Strömung induzierten Geschwindigkeit* $\vec{v}_m$ *ergibt die resultierende Geschwindigkeit* $\vec{v}$ *des Körpers.* ***b*** *Beispiel der Bewegung eines Körpers infolge von* $\vec{v}$ *innerhalb eines zweidimensionalen Raums, welcher von der x und y Richtung aufgespannt wird. Die zweidimensionale Ortskoordinate s beschreibt die Position des Körpers, und t den jeweiligen Zeitpunkt seines Auftretens.*

Eine Automatisierung der Bestimmung von $\vec{v}_{\overline{mess}}$ ist mittels moderner Signalverarbeitungstechniken erreichbar, wie schneller Kreuzkorrelation im Frequenzbereich (*FFT*) oder aufwendigere *PIV* (Particle-Imaging Velocimetry) und *PTV* (Partikel-Tracking Velocimetry) Verfahren (LAUTERBORN und VOGEL, 1984; RAFFEL et al., 1998), die bisher nur zur Auswertung optischer Datensätze herangezogen wurden, nicht jedoch zur Untersuchung von mehrstrahligen Sonardaten. Bei diesen Verfahren werden die Zeitreihen benachbarter Zellen sukzessive verschoben (*Lag*, Versatz) und nach jeder Verschiebeoperation kreuzkorreliert. Bei großer Ähnlichkeit von Mustern (z.B. Echoamplitude, Echolänge) in der Zeitreihe ergeben sich hohe Korrelationskoeffizienten (Fig. 2) und dies deutet auf Reflektionen hin, die von dem selben Objekt stammen, jedoch zu unterschiedlichen Zeiten an unterschiedlichen Orten emittiert wurden. Werden im Vorfeld Abschätzungen über die zu erwartenden Strömungswerte $\vec{v}_m$ $[\vec{v}_{m\_\min}, v_{m\_\max}]$ getroffen, so kann ein sogenannter ‚erlaubten Versatz' während eines Zeitintervalls Δt für einen Körper mit charakteristischem $\vec{v}_r$ festgesetzt werden. Zusätzlich wird ein sogenannter ‚Detektion-Schwellenwert' benötigt, um relevante von irrelevanten Korrelationskoeffizienten-Peaks unterscheiden zu können. Befindet sich ein Korrelationspeak nun über dem Detektions-Schwellenwert und innerhalb der Zone des ‚erlaubten-Versatzes', so wird mittels einer logischen UND Verknüpfung eine Objekt Detektion ausgelöst. Ferner können durch eine Koordinatenbestimmung des Peaks in Fig. 2 die exakten Lag Werte bestimmt werden und ein Einsetzen in (2) ergibt einen gemessenen Geschwindigkeitsvektor $\vec{v}_{\overline{mess}}$. Liegt darüberhinaus ein exakter $\vec{v}_m$ Wert (z.B. Doppler Messung) vor, so ergibt sich nach Einsetzen von $\vec{v}_{\overline{mess}}$ für v und Auflösen von (1) der

$\vec{v}_r$ Wert. Folglich werden Rückschlüsse auf den Reflektor möglich, denn häufig stellt dessen $\vec{v}_r$ ein charakteristisches Merkmal dar (z.B. beträgt die Steiggeschwindigkeit von Gasblasen in Wasser ca. 20 cm/s).

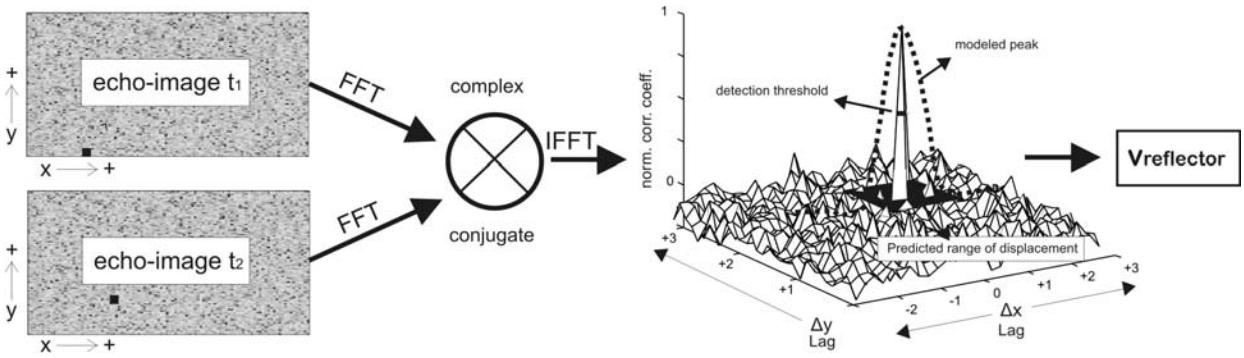

Figure 2: Schematischer Ablauf einer automatischen Objekt-Detektion. Zuerst werden zwei aufeinanderfolgende Echogramme (links) in den Frequenzbereich transformiert (FFT) und multipliziert/kreuzkorreliert (mittig); anschließend werden die Korrelationskoeffizienten resultierend aus verschiedenen Verschiebungsoperationen (x-Lag, y-Lag) ermittelt und in x bzw. y Richtung verbildlicht. Die ‚erlaubte Zone' ist als schwarzes Quadrat gekennzeichnet. Der Detektionsschwellenwert wurde hier auf 0.5 gesetzt.

Die Erfindung besteht darin $\vec{v}_m$ in die Datenauswertung mit einzubeziehen und so sich bewegende Reflektoren in den Daten per Algorithmus sicher zu detektieren, von anderen möglichen Reflektoren abzugrenzen und schließlich anhand deren $\vec{v}_r$ zu bewerten.

Ablauf des Algorithmus

(1) Aufnahme der Reflektions- oder Rückstreudaten in einem *N*-dimensionalem Array. Jedes Element des Arrays beinhaltet eine Zeitreihe, z.B. mit Amplituden- und Phaseninformation.
(2) Erhebung von Strömungsdaten $\vec{v}_m$ des den Körper umgebenden Medium (Modellrechnung, Messung)
(3) Optionale Filterung der Zeitreihen
(4) Bestimmung einer ‚erlaubten Zone' mit einer gewissen Unschärfe
(5) Definition eines Detektions-Schwellenwertes
(6) Korrelationsverfahren zwischen den verschiedenen Elementen des Arrays (z.B Kreuzkorrelation, PIV, PTV)
(7) Aufspüren maximaler Korrelationskoeffizienten und Bestimmung des Versatzes (Lag) Δ*s* innerhalb der Zeitspanne Δ*t*. Daraus resultiert die (momentane) Driftgeschwindigkeit $\vec{v}$ eines Reflektors.
(8) Bestimmung theoretischer $\vec{v}$ Werte ($\vec{v}_t$) für verschiedene $\vec{v}_r$ unter bekanntem $\vec{v}_m$
(9) Statistischer Vergleich zwischen $\vec{v}_t$ und $\vec{v}$ und anschließende Objektbewertung

Nutzung/Anwendung des Verfahrens

- Detektion von auf- oder absteigenden Reflektoren in der Wassersäule
  Fernerkundungsdaten: Multibeam mit *WCI* (Water Column Imaging)
  Strömungsdaten: Dopplermessung oder numerische Modelldaten
- Detektion von Rauchfahnen/Feuer
  Fernerkundungsdaten: Satellitenbildern
  Strömungsdaten: gemessene oder numerisch modellierte Windgeschwindigkeit

Vorteile gegenüber bisheriger Methoden

- Robustheit gegenüber anderer Detektionsalgorithmen (z.B. *STA*/*LTA*) durch vordefinierte Datenmuster bzw. die Definition einer ‚erlaubten Zone'
- Bisher verwendetet Korrelationsverfahren (DWORSKI und JACKSON, 1994) verwenden keine Strömungsdaten

Literatur

Artemov, Y. G., Egorov, V. N., Polikarpov, G. G., and Gulin, S. B., 2007. Methane emission to the hydro- and atmosphere by gas bubble streams in the Dnieper paleo-delta, the Black Sea. *Reports of the Natl. Acad. of Sci. of Ukraine* **5**, 110-116.

Dworski, J. G. and Jackson, D. R., 1994. Spatial and temporal variation of acoustic backscatter in the STRESS experiment. *Continental Shelf Research* **14**, 382-390.

Judd, A., Davies, G., Wilson, J., Holmes, R., Baron, G., and Bryden, I., 1997. Contributions to atmospheric methane by natural seepages on the UK continental shelf. *Marine Geology* **137**, 165-189.

Lauterborn, W. and Vogel, A., 1984. Modern optical techniques in fluid mechanics. *Ann. Rev. Fluid Mech.* **16**, 223-44.

Raffel, M., Willert, C., and Kompenhans, J., 1998. *Particle Image Velocimetry*. Springer, Berlin.

Appendix B

Seep bubble acoustics – the inversion of bubble backscatter into gas flux and principle limitations

Gas bubble acoustics

The scattering behavior of free gas bubbles in the sea has especially been investigated in terms of wind/breaker-entrained or ship-induced small gas bubbles on a micrometer scale. Because bubbles affect under water communication and due to the possibility to acoustically trace a ship's wake, much of the acoustic gas bubble research has been carried out in a military sense. The more interested reader to underwater sound in this context is referred to the incomplete list of English literature (MEDWIN, 1977; CLAY and MEDWIN, 1977; URICK, 1983; LEIGHTON, 1994; MEDWIN and CLAY, 1998; VAGLE and FARMER, 1998).

Gas bubbles in water act as a strong acoustic scatterer. On the one hand this is based on the huge sound speed and density differences between water and gas, respectively. On the other hand scattering of gas bubbles may significantly increase due to resonance effects. ANDERSON (1950) gave the full solution to sound scattering from a fluid sphere in liquid yielding the pressure field by solving the three dimensional wave equation. Scattering from a gas bubble is realized by letting the density ρ and sound speed *c* be those of the respective gas (ρ_1, c_1) at its local pressure/water depth and temperature (FEUILLADE and CLAY, 1999) and relate this to the environmental liquid (ρ_2 , c_2). Changing the gas composition of an acoustic bubble is attributed a minor effect at least in shallow water due to small changes in the mole based density change for different gases in water. Using the full modal solution of bubble scattering requires significant computational effort such as solving spherical *Bessel* and *Neumann* functions, and thus approximations were introduced to describe especially the scattering behavior of small surface water gas bubbles (e.g. the high-pass filter model by JOHNSON, 1977).

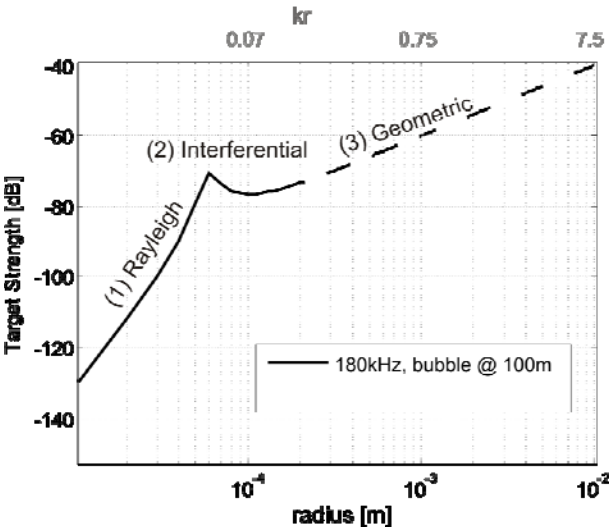

*Figure 1: Target strength (=10*log10(σ_{bs}/A_1)), A_1 is the unit section [m²]) showing resonance peak of a spherical gas bubble of 1mm radius at 100 m water depth; calculated after equ. (3). Note the dashed line, where the criterion kr ≪1 is not fulfilled anymore.*

The scattering of a spherical object can be divided into three different regimes. If the acoustic wavelength λ is much bigger than a spherical bubble of radius *r* (*kr*≪1, *k*=dimensionless wavenumber) then omnidirectional (1) *Rayleigh* scattering (Figure 1) occurs with a pronounced backscattering strength increase proportional to *kr*² until the (2) *interferential* regime is entered at *kr*~1 for rigid spheres and kr<1 for gas bubbles (e.g. *kr*=0.0136 at sea-level). The interferential regime is characterized by a scattering peak (Figure 1) caused from the natural breathing frequency f_{res} of a bubble. This effect is extensively used even for quantitative gas bubble studies (MEDWIN, 1977; VAGLE and FARMER, 1992). MINNAERT (1933) first described an equation of motion for this monopole mode for a spherical bubble. He showed that the frequency f_{res} of the monopole resonance frequency is given by

$$f_{res} = \frac{1}{2\pi r}\sqrt{\frac{3\gamma P_w}{\rho_w}} \tag{1}$$

where γ is the ratio of the specific heats of bubble gas, P_w the ambient pressure, and ρ_w the water density. An even simpler approximate form of equation 1 is given in MEDWIN and CLAY (1998) directly showing the dependence on water depth *z* in equation 2

$$f_{res} \approx \frac{3.25\sqrt{1+0.1z}}{r} \tag{2}$$

In the given *kr*≪ 1 range, an approximate backscattering cross-section σ_{bs} of a single gas bubble can be calculated after Medwin (1970) to

$$\sigma_{bs} = \frac{r^2}{((\frac{f_{res}}{f})^2 - 1)^2 + \delta^2} \tag{3}$$

with the resonance frequency f_{res} calculated after equation (1). If *f*= f_{res}, then the damping constant δ sets the limit for scattering strength and is commonly set to 0.2.

If the sonar transmit frequency f resembles the resonance frequency f_{res} of a gas bubble at given depth *z*, then the bubble backscattering cross-section or backscattering length σ_{bs} as well as the absorption and extinction cross-sections peak and are much higher than compared to that of a rigid object of similar geometry.

If *kr* further increases, then the *geometric* regime is entered (Figure 1), where incident and diffracted waves must be coherently summed to give the true pressure field, which requires the full modal solution after ANDERSON (1950). Following, the monopole approximations does not hold any longer here to calculate the backscatter using equation 3. Nevertheless, this approximate equation was erroneously used in the context of high frequency acoustic seep bubble investigations as will be shown later. In contrast to the steady increase of

approximated σ_{bs} after equation (3) with *kr* in the geometric regime, the Anderson solution even predicts a backscatter drop in the range between *kr*=0.4 and 1 (Figure 2). For higher *kr* much energy is scattered forward and shows significant amplitude variations with distance from the source, while the backscatter amplitude remains relatively unchanged (FEUILLADE and CLAY, 1999; their Fig. 6). The occurring superresonances at high values are very narrow and therefore the overall contribution to the backscatter over a broader range of gas bubble radii is considered small.

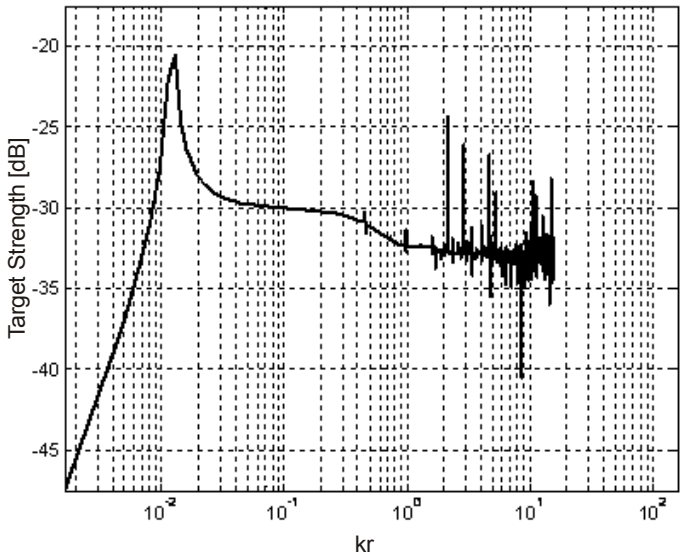

Figure 2: Modal solution of the theoretical backscatter of a spherical gas bubble with density gas/water ratio ρ1/ρ2=0.001/1 and sound velocity ratio c_1/c_2=330/1500. The plot was computed using the Anderson model (Anderson (1950)).

Moreover, if *kr* approaches 5 and larger the scatter behaves increasingly directive with even more sound scattered forward than backward (FEUILLADE and CLAY, 1999; their Fig. 6) and a gas bubble can then be considered an acoustic lense for sound in terms of the scattering field intensity (Figure 3).

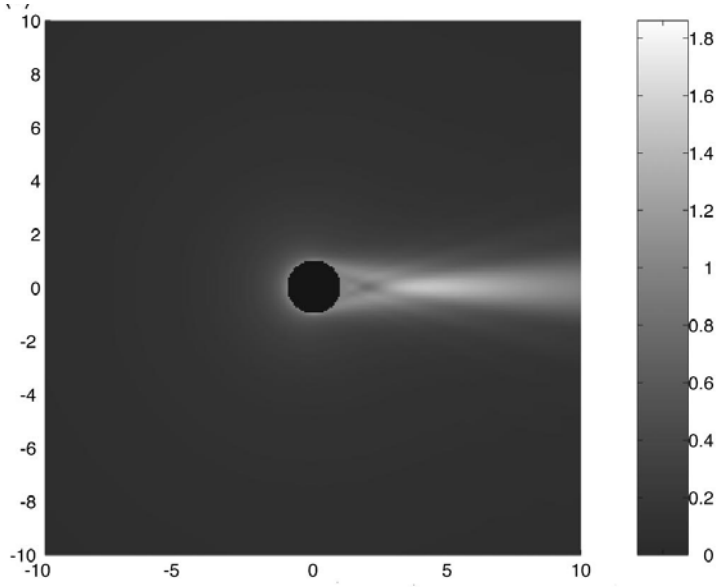

Figure 3: from FEUILLADE and CLAY (1999); scattered field amplitude around a gas filled sphere ($g=\rho_1/\rho_2$, $h=c_1/c_2$, g=0.001, h=0.22 at kr=20). Pressure amplitude is expressed as grayscale plot. The external field is incident from the left. To the right of the bubble a very small shadow emerges,followed by a large high scattering trail indicating strong forward scatter.

Prestudy GasQuant and Modeling of bubble backscatter

During the design of GasQuant care was taken to choose such a frequency, that scattering effects in the non-linear interferential regime can be excluded for the given range of natural gas bubbles size radii and water depth down to 1000 m.

Figure 1 shows, that this is true e.g. for 100 m water depth and – given the expected seep bubble size range between 0.5-10 mm radius and a system frequency of 180 kHz, *kr* values correspondingly range between 0.3 and 7.1. It was believed, that the backscatter scales here with the radius squared of the gas bubbles similar as is the case for a rigid sphere. However, it was shown previously (Figure 2) that the calculation of the exact solution using the Anderson model draws another picture especially in the relevant *kr* range of a potential GasQuant deployment.

GREINERT and NÜTZEL (2004) have conducted an experimental setup based on the assumption, that equation 3 is valid for the typical seep bubble and used frequencies. By their experimental setup with a similar system like GasQuant, they tested the acoustic backscattering response to various gas bubble ebullition rates and stated a correlation of the backscattering with the gas flux independently from the bubble radii distribution within certain ranges. This would be a surprising result, as σ_{bs} scales with r^2 and the bubble volume with r^3.

In the beginning of this thesis we conducted a similar experiment like GREINERT and NÜTZEL (2004) with GasQuant, but found ambiguous results.

To further investigate the experimental results, a numerical model was designed to calculate the theoretical acoustic backscatter S_{bs} for specific bubble populations expressed by means of a normalized probability density function *PDF* about bubble radii. If the distance of individual gas bubbles is larger than the acoustic wavelength λ, which is the case for the use of high frequency sonar, then the backscattering cross-sections σ_{bs} of individual bubbles coherently sum (CLAY and MEDWIN, 1977) and the backscatter S_{bs} per unit volume of *N* bubbles can be expressed using

$$S_{bs} = N\int_0^\infty \sigma_{bs}(r) \times PDF(r)\, dr \tag{4}$$

Correspondingly, the volume for a population of spherical bubbles can be calculated using

$$V = N\frac{4}{3}\pi\int_0^\infty PDF(r) r^3 dr \tag{5}$$

A relation between *V* and S_{bs} is then obtained for different *PDF* and *N* combinations. The seep researcher is mainly interested in gas flux instead of volume. This requires the introduction of gas bubble rising velocities v_b to obtain the quantity

$$F*_b = V \times v_b \tag{6}$$

with a unit of [$m^3 ms^{-1}$].

An analytical solution for seep bubble v_b is missing and we use an approximation calculated by code given by courtesy of Ira Leifer and presented in Figure 4.

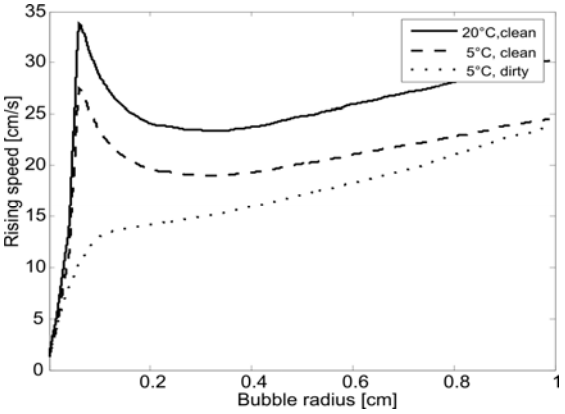

Figure 4: Rising velocities for two clean bubbles showing non-linear behavior, and rising velocity of a dirty bubble. Code for calculation is taken from Ira Leifer's www.bubbleology.com.

Substitution of equation 5 into 6 yields

$$F_b* = N\frac{4}{3}\pi\int_{r_1}^{r_2} v_b(r)\times PDF(r)\times r^3 dr \qquad (7)$$

Given the dimension [m³m s^{-1}] of equation 7, F^* is not a flux. But if we define an *acoustic observation length* L [m], which is most readily the length of an acoustic integration window of time interval τ , then we obtain

$$F = \frac{N\times\frac{4}{3}\pi\int_{r_1}^{r_2} v_b(r)\times PDF\times r^3 dr}{L} \qquad (8)$$

and L can be built by the product of sound speed c [ms^{-1}] and pulse length τ [s] giving rise to correct flux dimension [m³s^{-1}] for F in equation 8.

The integration of equation 4 and 8 was performed by simple summation using a small step size dr to account for narrow resonance peaks and non-linearity of v_b (Figure 4) to obtain the relation S_{bs} vs F.

To test the sensitivity of S_{bs}/F on *PDF*-uncertainty we run the model for artificially and natural seep *PDF* reported in GREINERT and NÜTZEL (2004) and LEIFER and BOLES (2005). Moreover, we shifted one of these *PDF* to simulate the effect of a smaller mean bubble radius μ of the gaussian shaped 'leifer minor' *PDF* (Figure 5) to account for bubble dissolution in the water column (s. Chapter IV).

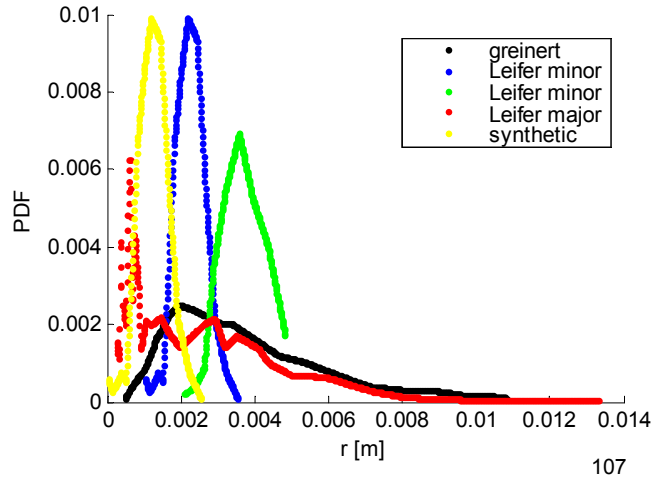

Figure 5: Normalized probability density function measured at artificial (GREINERT and NÜTZEL, 2004) and two minor and one major natural gas bubble seep sites (LEIFER and BOLES, 2005). The synthetic (yellow) PDF presents a left shift of the blue PDF.

To compare our model data with experimental results the input parameters *f*=300 *kHz*, *z*=5 *m,* and the corresponding *PDF* (Figure 5, greinert) were taken from GREINERT and NÜTZEL (2004, their Fig. 9). The model tolerably resembles the data for little gas flux (Figure 6), especially if the data is corrected with a slight negative flux offset that might be necessary to correct flux measurement overestimation. With increasing gas flux the model predicts higher values than actually have been measured. We suggest this effect to be caused from (1) overestimation of S_{bs} due to the use of the approximation equation 3 in the model (2) extinction effects of larger bubble populations.

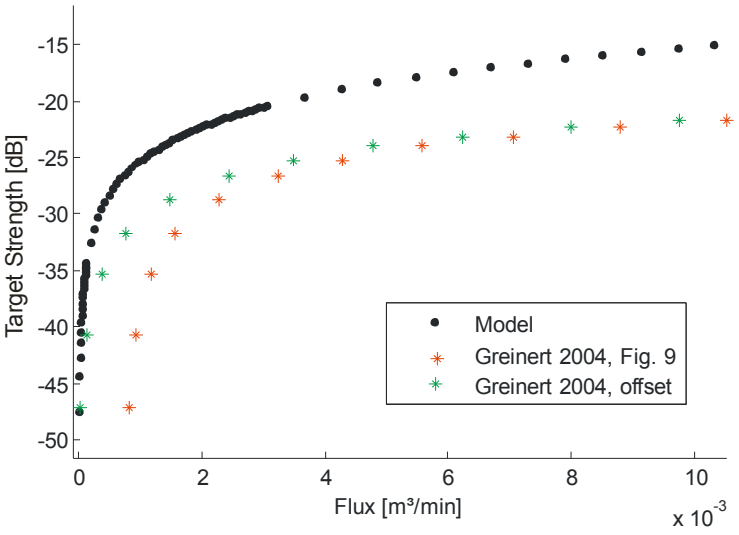

Figure 6: Modeled compared to real data (red dots) taken from GREINERT and NÜTZEL (2004).

Usually, the *PDF* of a given seep site is unknown and thus we model backscatter changes caused from various *PDF* scenarios (Figure 5) for similar gas flux ranges.

Although it was stated, that the S_{bs}/F ratio is independent from the *PDF* (GREINERT and NÜTZEL, 2004), our model results suggest the opposite behavior. Figure 7 reveals, that S_{bs} only linearly correlates with the flux for an unchanged *PDF*. Significant difference in the S_{bs}/F ratio arises if the *PDF* is varied.

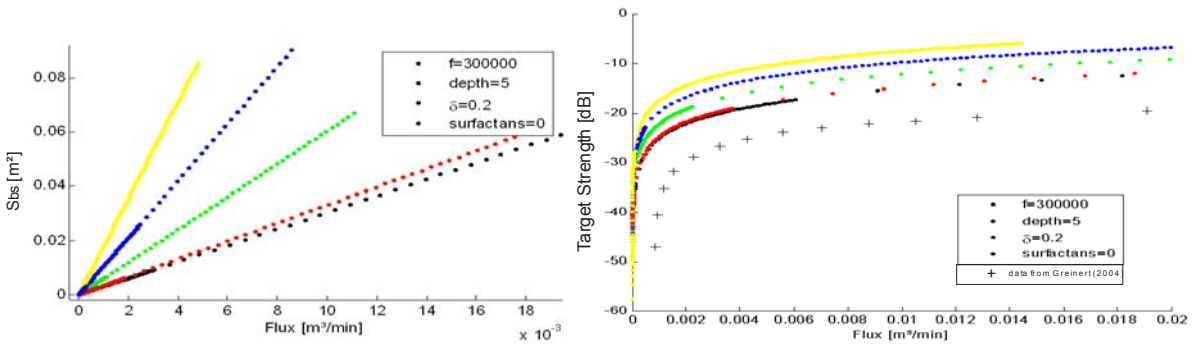

Figure 7: (a) Acoustic backscattering length and its logarithmic (b) Target Strength presentation over flux as response to the specific bubble size spectra from Figure 5 and compared to measrement values (black crosses) from GREINERT and NÜTZEL (2004).

A similar variance of the S_{bs}/F ratio is modeled for the GasQuant experiment discussed in this study using *f*=180 kHz at 70 meters water depth (Figure 8) as model input parameters.

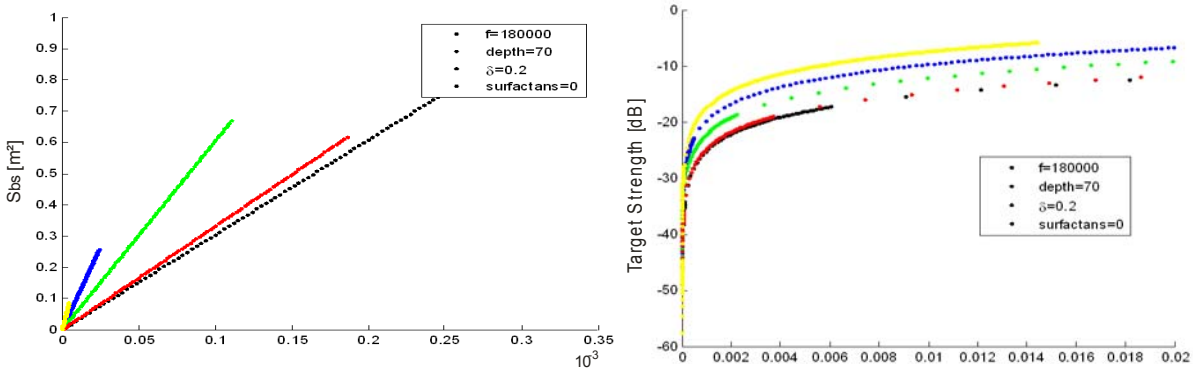

Figure 8: Same as Figure 7 but adapted for GasQuant study site at 70 m depth given f=180 kHz and z=70 m.

Finally, we create a scenario where *f* and *z* were chosen in such a manner to cause the resonant bubble radius be located in the center of the gaussian shaped *PDF*. It becomes obvious, that an inversion of backscattering into gas flux virtually becomes impossible if resonant gas bubbles are present (Figure 9).

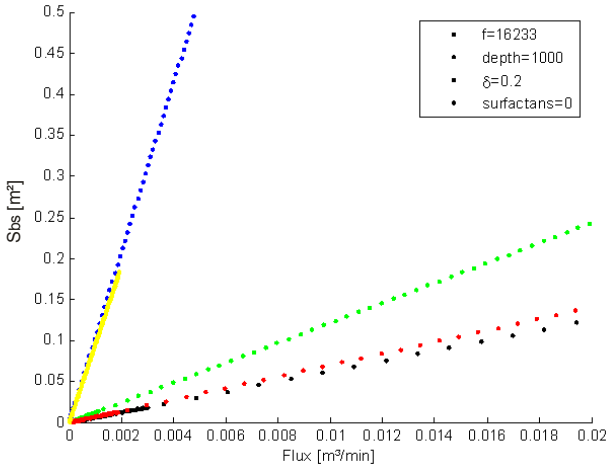

Figure 9: Acoustic backscatter response to the given bubble size spectra in Figure 5. f and z were chosen to cause resonance effects.

We have shown, that the approximate σ_{bs} after equation 3 increases with *kr* in the geometric regime. However, application of the approximate solution is critical and the real backscatter solution for a perfect sphere/bubble calculated after (ANDERSON, 1950) merely indicates backscatter increase with object size (Figure 2). Application of the full solution will produce an even stronger dependency of S_{bs} than presented here (Figure 7-9) on the given *PDF*.

Limitations of using backscattering approximation and implications for acoustic gas seepage inversions

Seep researchers have adapted acoustic scattering techniques from the well examined research field about the acoustics of near surface gas bubbles in the Sea. However, seep bubbles are released at depth with much larger radii and often travel hundreds of meters vertically through the water column and thus undergo a broad dynamic range in terms size and acoustic scattering (Figure 10). The ideal frequency for seep research can merely be given and highly depends on the needs and local settings of the study site. In most seeping areas gas bubbles were not observed at sea-level and following, they have significantly shrunk and finally dissolved during their rise. This implies shifting of their initial bubble size population partially into the interferential and/or Rayleigh regime and has therefore large effects on ship-born flare imaging in terms of quantitative scattering perspectives.

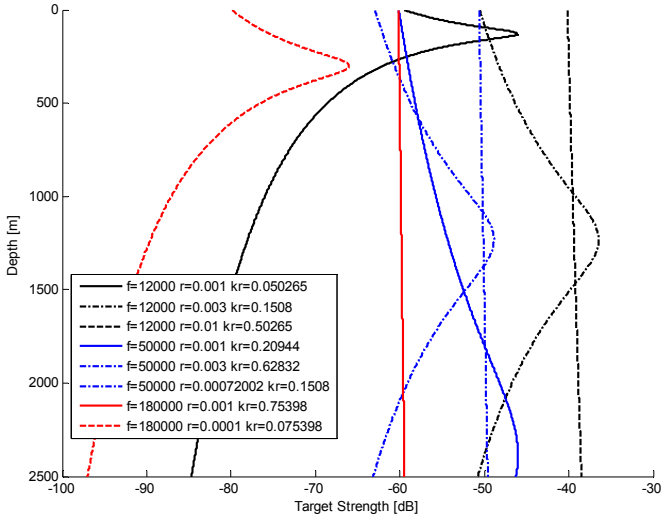

Figure 10: Calculated after equ. 3 to stress the large variation of acoustic response to bubbles insonified by different sonar frequencies at depth range down to 2500 m water depth.

The effect of a hydrate skin may preserve gas bubbles unchanged for larger rising distances (REHDER et al., 2002), but at the same time the coating changes the bubble rise velocity v_b and the elasticity of the sphere, and therefore its acoustic behavior, i.e. an increased resonant radius and decreased backscattering strength are expected (MAKSIMOV and SOSEDKO, 2005).

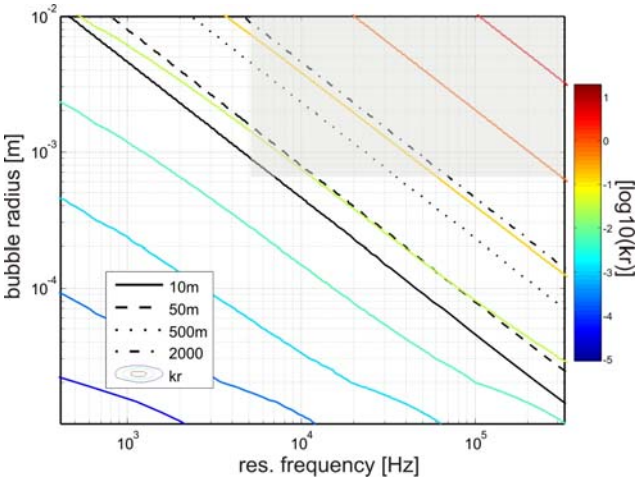

Figure 11: Plot shows resonance frequencies of respective gas bubbles at various depths were seepage was reported. Common seep bubble sizes radii (0.5-10 mm) and typical flare imaging frequency range (3.5-500 kHz) equipment are highlighted with a grey-shade rectangle. Color coded lines indicate the acoustic regime in terms of kr.

Figure 11 presents a reprint of GREINERT and NÜTZEL (2004) showing the range of typically used sonar for seep studies and potential resonance effects at different depths. We additionally plot *kr* in Figure 11 as color coded lines; it becomes obvious that most of the acoustic seep work takes place in the geometric regime, where equation 3 must not be applied. To conduct a sophisticated sensitivity study about acoustic inversion at natural seep sites, we therefore suggest to incorporate the full modal solutions. Furthermore adaption for hydrated bubbles, *f* and *z* dependent δ (DEVIN, 1959) and consideration of already available techniques known from fisheries research (MACLENNAN and SIMMONDS, 1992) are needed. Seep bubbles show significant shape variations with size from spherical, spheroidal to ellipsoidal and thus proper approximations are needed similar like the ones already present in fisheries acoustics (Figure 12) .

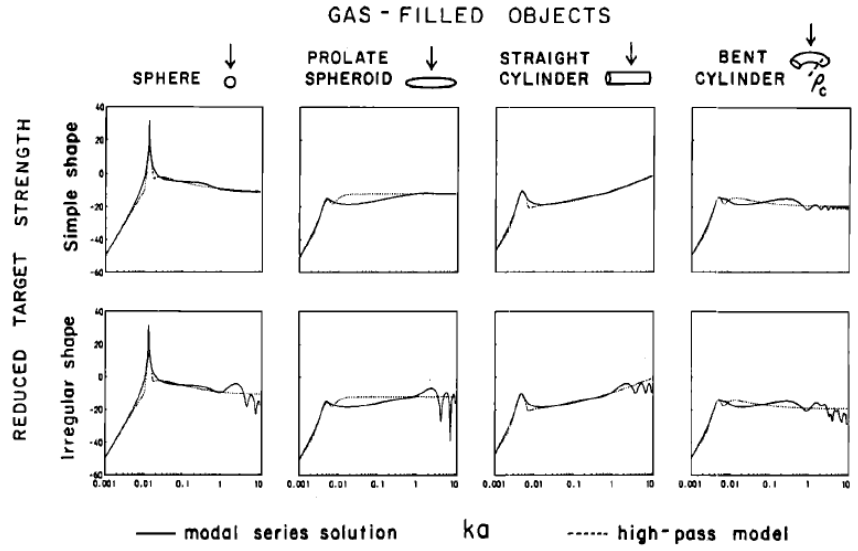

Figure 12: High-pass (dashed) and modals series solutions (solid) for various shapes of gas-filled objects from STANTON (1989) to describe scattering behavior of fish.

For acoustic studies, seepage should be classified in terms of gas bubble size *PDF* and ebullition type to choose the proper acoustic tool for quantification issues. E.g. plume scattering of violent gas seepage is very complicated. It might better be quantified by the acoustic mapping of the plume shape yielding the three dimensional extension and shape-variations caused from the current flow-field, that might be indicative for the total gas flux. In contrast acoustic monitoring and quantification seems feasible for very low flux rates with the appropriate and calibrated equipment. Modeling can then help to estimate the respective error if the bubble population of the site is unknown.

References

Anderson, V. C., 1950. Sound Scattering from a Fluid Sphere. *J. Acoust. Soc. Am.* 22, 426-431.

Clay, C. S. and Medwin, H., 1977. *Acoustical oceanography: Principles and Applications*. John Wiley & Sons, New York.

Devin, C. J., 1959. Survey of Thermal, Radiation, and Viscous Damping of Pulsating Air Bubbles in Water. *J. Acoust. Soc. Am.* 31, 1654-1667.

Feuillade, C., 1995. Scattering from collective modes of air bubbles in water and the physical mechanism of superresonances. *J. Acoust. Soc. Am.* 98, 1178-1190.

Feuillade, C. and Clay, C. S., 1999. Anderson (1950) revisited. *J. Acoust. Soc. Am.* 106, 553-564.

Greinert, J. and Nützel, B., 2004. Hydroacoustic experiments to establish a method for the determination of methane bubble fluxes at cold seeps. *Geo.-Marine Letters* 24, 75-85.

Johnson, K. J., 1977. Sound scattering from a fluid sphere revisited. *J. Acoust. Soc. Am.* 61, 375-377.

Leifer, I. and Boles, J., 2005. Measurement of marine hydrocarbon seep flow through fractured rock and unconsolidated sediment. *Marine and Petroleum Geology* 22, 551-568.

Leighton, T. G., 1994. *The Acoustic Bubble*. Harcourt Brace & Company, London, San Diego, New York.

MacLennan, D. N. and Simmonds, E. J., 1992. *Fisheries acoustics*. Chapman & Hall, London.

Maksimov, A. O. and Sosedko, E. V., 2005. Dynamics of sea bubbles covered by a hydrate skin. *XVI Session of the Russian Acoustical Society*, 459-462.

Medwin, H., 1970. In Situ Acoustic Measurements of Bubble Populations in Coastal Ocean Waters. *Journal of Geophysical Research* 75, 599-611.

Medwin, H., 1977. Acoustical determinations of bubble-size spectra. *Journal of the Acoustical Society of America* 62, 1041-1044.

Medwin, H. and Clay, C. S., 1998. *Fundamentals of Acoustical Oceanography*. Academic Press, Boston.

Minnaert, M., 1933. On musical air bubbles and the sounds of running water. *Philos. Mag.* 10, 235-248.

Rehder, G., Brewer, P. W., Peltzer, E. T., and Friederich, G., 2002. Enhanced lifetime of methane bubble streams within the deep ocean. *Geophysical Research Letters* 29, 10.1029/2001GL013966.

Stanton, T. K., 1989. Simple approximate formulas for backscattering of sound by spherical and elongated objects. *J. Acoust. Soc. Am.* 86, 1499-1510.

Urick, R. J., 1983. *Principles of underwater sound*. Peninsular Publishing.

Vagle, S. and Farmer, D. M., 1992. The Measurement of Bubble-Size Distributions by Acoustical Backscatter. *Journal of Atmospheric and Oceanic Technology* 9, 630-644.

Vagle, S. and Farmer, D. M., 1998. A Comparison of Four methods for Bubble Size and Void Fraction Measurements. *IEEE Journal of Oceanic Engineering* 23, 211-222.

Appendix C

Shallow Microbial Recycling of Deep-Sourced Carbon in Gulf of Cadiz Mud Volcanoes

Marianne Nuzzo[1]; Edward R. C. Hornibrook[1]; Christian Hensen[2]; R. John Parkes[3]; Barry A. Cragg[3]; Joachim Rinna[3]; Jens Schneider von Deimling[2]; Stefan Sommer[2]; Vitor H. Magalh˜aes[4,5]; Anja Reitz[2]; Warner Brückmann[2] and Luis M. Pinheiro[6]

[1]Bristol Biogeochemistry Research Centre, Department of Earth Sciences, University of Bristol, United Kingdom
[2]Leibniz-Institute for Marine Sciences, IFM-GEOMAR, University of Kiel, Germany
[3]School of Earth, Ocean and Planetary Sciences, University of Wales at Cardiff, United Kingdom
[4] INETI, Marine Geology Department, Alfragide, Portugal, University of Chicago, USA
[5]University of Chicago, USA
[6]CESAM and Geosciences Department, Universidade de Aveiro, Aveiro, Portugal

published in *Geomicrobiology Journal* (2008), 25, doi: 10.1080/01490450802258196

Abstract

Based upon the molecular and isotopic composition of hydrocarbons it has been proposed that the source of CH_4 in Gulf of Cadiz mud volcanoes (MV) is a mixture of deep sourced thermogenic CH_4 and shallow biogenic CH_4. We directly investigated this possibility by comparing porewater CH_4 concentrations and their $\delta^{13}C$ values with the potential for Archaeal methanogenesis in Gulf of Cadiz mud volcano (MV) sediments (Captain Arutyunov, Bonjardim, Ginsburg and Porto) using ^{14}C-rate measurements. The CH_4 has a deep sourced thermogenic origin ($\delta^{13}C \sim -49‰$) but becomes ^{13}C-depleted in and beneath the zone of anaerobic oxidation of methane (AOM) where the rates of hydrogenotrophic methanogenesis increase. Thus we infer that a portion of AOM produced CO_2 is being recycled to CH_4 by methanogens yielding further ^{13}C-depleted CH_4, which might be misinterpreted as indicative of a fully shallow biogenic origin for this gas. Production of H_2 is related to compositional changes in sedimentary organic matter, or to upward flux of substrate-enriched fluids. In contrast to other MVs in the Gulf of Cadiz, Ginsburg MV fluids are enriched in SO_4^{2-} and contain very high concentrations of acetate (2478 µM below 150 cmbsf); however, the high levels of acetate did not stimulate methanogenesis but instead were oxidized to CO_2 coupled to sulphate reduction. Both anaerobic oxidation of thermogenic CH_4 linked to shallow methanogenesis and fluid geochemistry control the recycling of deep-sourced carbon at Gulf of Cadiz MVs, impacting near-surface $\delta^{13}C$-CH_4 values.

Appendix D

Seabed methane emissions and the habitat of frenulate tubeworms on the Captain Arutyunov mud volcano (Gulf of Cadiz)

S. Sommer, P. Linke, O. Pfannkuche, T. Schleicher, J. Schneider v. Deimling, A. Reitz, M. Haeckel, S. Flögel, C. Hensen

Leibniz Institute of Marine Sciences, IFM-GEOMAR, Wischhofstrasse 1–3, 24148 Kiel, Germany

published in *Marine Ecology Progress Series* (2009), doi: 10.3354/meps07956

Abstract

Submarine mud volcanism represents an important pathway for methane from deeper reservoirs to the surface, where it enters the benthic carbon cycle. To quantify overall methane release from the Captain Arutyunov mud volcano (CAMV) and to assess the contribution of macrobenthic seep organisms to the regulation of the benthic methane flux, we linked water column methane concentrations, seabed methane emission and pore water geochemistry to the spatial distribution of seep biota. Prominent organisms of the CAMV seep biota were 3 different species of frenulate tubeworms. Seabed methane emission ranged from 0.001 to 0.66 mmol m^{-2} d^{-1}. Dense patches of tubeworms were associated with the lowest seabed methane emission. Elevated methane emission was associated with a sporadic distribution of tubeworms and the occurrence of numerous mud clasts. Despite the presence of a large subsurface methane reservoir, the estimated total methane release from CAMV was low (0.006 × 106 mol yr^{-1}). In addition to direct methane consumption by Siboglinum poseidoni, the tubeworms likely contribute to the retention of methane carbon in the sediment by affecting bacterial communities in the proximity of the tubes. The siboglinids create new meso-scale habitats on the sediment surface, increasing habitat heterogeneity and introducing niches for bacterial communities.